

Electronic Dura mater
Soft, multimodal neural interfaces:
Technology, integration and implementation to surface implants

THÈSE N° 8112 (2018)

PRÉSENTÉE LE 12 JANVIER 2018

À LA FACULTÉ DES SCIENCES ET TECHNIQUES DE L'INGÉNIEUR
CHAIRE FONDATION BERTARELLI DE TECHNOLOGIE NEUROPROSTHÉTIQUE
PROGRAMME DOCTORAL EN BIOTECHNOLOGIE ET GÉNIE BIOLOGIQUE

ÉCOLE POLYTECHNIQUE FÉDÉRALE DE LAUSANNE

POUR L'OBTENTION DU GRADE DE DOCTEUR ÈS SCIENCES

PAR

Arthur Edouard HIRSCH

acceptée sur proposition du jury:

Prof. T. Lasser, président du jury
Prof. S. Lacour, directrice de thèse
Prof. J. Vörös, rapporteur
Prof. M. Decré, rapporteur
Prof. Ph. Renaud, rapporteur



ÉCOLE POLYTECHNIQUE
FÉDÉRALE DE LAUSANNE

Suisse
2018

If you have a difficult task give it to a lazy man,
he will find an easier way to do it.
Bulgarian proverb

To my wife, Emilie ...



Acknowledgements

This thesis would not have been possible without the support, encouragement and help of many people.

First, I would like to thank my thesis director, Prof. Stéphanie P. Lacour, for giving me the opportunity to join the laboratory for soft bioelectronic interfaces (LSBI) and work on exciting projects like the *e-dura*. Throughout these four years, she continuously provided me with helpful guidance, support and most importantly the freedom to explore new ideas. Her enthusiasm and passion for research were always stimulating and inspirational.

I would like to thank the members of the jury, Profs. Theo Lasser, Philippe Renaud, Janös Vörös and Michel Decré, for taking the time to critically review my work.

I also would like to thank the *Fonds National Suisse - Nano Tera project* for providing the funding for this thesis.

Furthermore, I would like to thank Prof. Grégoire Courtine for his help and guidance in the *e-dura* and *ECoG* projects. The energy and devotion he has for his research were really contagious and motivational.

A very special thanks goes out to Ivan Minev who mentored me during my first years at the LSBI. I learned a lot by working at his side and his humor and personality are one of a kind.

My thanks to my collaborators of the *e-dura* project and in particular to Quentin Barraud, Nikolaus Wenger, Marco Capogrosso, Tomislav Milekovic, Léonie Asboth, Fabien Wagner and Jérôme Gandar, Nicolas Vachicouras, Christina Tringides and Florian Fallegger.

Very special thanks goes to Hadrien Michaud and Aaron Gerratt with whom I shared the gallium adventure. They have been great collaborators but also true friends.

I also would like to thank the staff from the center for micronanotechnologies at EPFL (CMi) and the Wyss neuromicrosystem platform at Campus Biotech and in particular Anthony Guil-

Acknowledgements

let for his help and advices.

Working in the LSBI has been a great pleasure in the past four years, and I would like to thank all its past and present members. In particular, Nicolas Vachicouras, Florian Fallegger, Frédéric Michoud, Hadrien Michaud and Aaron Gerratt who review several chapters of this thesis but also Jennifer, Laurent, Giuseppe, Amélie, Sandra, Aaron, Xiaoyang, Ivan, Kate, Cédric, Alessia, Alba, Christina, Kristie and all the others for great scientific and lunchtime conversations.

My greatest thanks goes to my family and particularly to my wife, Emilie, for her unconditional support.

Lausanne, 25 Septembre 2017

Arthur Hirsch

Abstract

Neuroprosthetic devices are engineered to study, support or replace impaired functions of the nervous system. The neural interface is an essential element of neuroprosthetic systems as it allows for transduction of signals and stimuli of desired functions (recording, stimulation, neuromodulation). A persistent challenge for translating neuroprosthetics from the laboratory to the clinic is the lack of long-term biointegration of neural interfaces. This thesis aims at improving biointegration of neural interfaces by reducing the mechanical mismatch between implant and neural tissue.

In this thesis, the design, fabrication and characterization of soft surface neural interfaces is described. These soft neural interfaces, termed *electronic dura mater* or *e-dura*, were designed to mimic the mechanical properties of dura mater. In contrast with conventional neural technologies, e-dura neural interfaces were made of soft and compliant materials. They conform to the circumvolutions of the brain and spinal cord and follow their dynamic deformation without damaging the surrounding neural tissues. These soft multimodal neural interfaces were fabricated on silicone substrates using techniques imported from the microfabrication industry and incorporate compliant electrodes, stretchable electrical interconnects and a micro-catheter for drug delivery.

Evaluation of the e-dura biointegration with spinal tissues demonstrated reduced foreign body reaction, compared to stiff polyimide based implants. Additionally, mechanical tests on an *in-vitro* spinal surrogate provided insights on the complex biomechanical coupling between implants and neural tissue. E-dura interfaces, implanted in rodents, maintained their functionality over extended periods and provided high-resolution neuronal recordings and concurrent delivery of electrical and chemical neuromodulation.

Eventually, the use of gallium thin films was explored to create highly conductive and stretchable interconnects for integration of active electronic components in e-dura neural interfaces.

Key words: neural interfaces, implant, ECoG, spinal cord stimulation, biointegration, e-dura, stretchable electronics, thermal evaporation, micro-cracked gold, gallium, thin film.



Résumé

Les neuroprothèses sont conçues dans l'objectif d'étudier, suppléer, voire même se substituer aux fonctionnalités défaillantes du système nerveux. Élément essentiel de ces dispositifs neuroprothétiques, l'interface neuronale permet une transduction efficace des signaux et autres stimuli électrochimiques vers les fonctionnalités nerveuses ciblées (enregistrement, stimulation, neuromodulation). Un défi majeur pour le transfert de ces neuroprothèses du laboratoire à l'application médicale concrète, est la difficulté de produire des interfaces neuronales capables de se bio-intégrer et de maintenir leur fonctions dans la durée. La présente thèse vise à pallier à ce déficit, en s'attachant à réduire l'incompatibilité mécanique entre interface neuronal et tissu nerveux.

Ce travail de recherche décrit la conception, la fabrication et la caractérisation d'interfaces neuronales souples. Appelées dure-mère électroniques ou e-dura, celles-ci sont conçues pour simuler les propriétés mécaniques de la dure-mère. Contrairement aux technologies neuronales conventionnelles, les interfaces neuronales e-dura sont fabriquées à l'aide de matériaux souples et étirables. Elles se conforment aux circonvolutions du cerveau et de la moelle spinale, dont elles suivent leurs déformations dynamiques sans toutefois endommager les tissus nerveux environnants. Ces interfaces neuronales multimodales et souples sont fabriquées sur des substrats élastomériques en employant des techniques issues de la microfabrication ; elles incorporent des électrodes et des pistes électroniques souples ainsi qu'un micro-cathéter pour l'administration médicamenteuse.

L'implantation prolongée de l'e-dura au contact des tissus nerveux de la moelle épinière a démontré une réaction réduite d'inflammation en comparaison avec celle provoquée par les implants rigides en polyimide. Les tests mécaniques réalisés sur un substitut in-vitro de moelle spinale ont également permis d'apporter de nouvelles perspectives sur le couplage biomécanique complexe entre implants et tissu neural. Implantées dans des rongeurs, les interfaces e-dura ont maintenu leurs fonctionnalités sur la durée et ont permis l'enregistrement de signaux neuronaux de haute-résolution, et la stimulation fonctionnelle de la moelle spinale.

Enfin, l'utilisation de fines couches de gallium a été explorée pour créer des pistes électroniques étirables et hautement conductrices, permettant d'intégrer des composants électroniques actifs au sein d'interfaces neuronales e-dura.

Acknowledgements

Mots-clés : interfaces neuronales, implant, EcoG, stimulation de la moelle spinale, biointégration, e-dura, électronique étirable, évaporation thermique, or micro-fissuré, gallium, couche mince.

Contents

Acknowledgements	i
Abstract (English/Français)	iii
List of figures	xi
List of tables	xv
Introduction	1
1 Technical specifications, components and soft neurotechnologies for e-dura implants	9
1.1 Technical specifications for e-dura neural interfaces	9
1.2 Basic components for e-dura neural interfaces	11
1.2.1 Substrate	11
1.2.2 Biotransducers	12
1.2.3 Stretchable interconnects	13
2 Soft substrate for long term biointegration of e-dura implant	15
2.1 Introduction	15
2.1.1 Motivation	15
2.1.2 Goal and specific aims	16
2.1.3 Case study	17
2.1.4 Mechanical properties and dynamics of natural dura mater in rat	17
2.1.5 Subdural spinal cord implants	20
2.2 Mechanical evaluation in spinal cord surrogate model	22
2.2.1 Spinal cord surrogate model	22
2.2.2 Mechanical tests on spinal cord surrogate	23
2.3 Long term biointegration of subdural spinal implant in rat model	25
2.3.1 Animal groups and surgical implantation	25
2.3.2 Biointegration evaluation	27
2.4 Discussion	30
2.5 Conclusion	32
2.6 Contribution	33

3	Electrical stimulation and biopotential recording e-dura implants using micro-cracked gold technology	35
3.1	Introduction	35
3.1.1	Motivation	35
3.1.2	Goal and specific aims	37
3.2	Technological development	37
3.2.1	Process limitations	37
3.2.2	Proposed solutions	38
3.3	Functional electrical stimulation validation	40
3.3.1	Rodent e-dura FES implant	40
3.3.2	<i>In-vitro</i> validation	40
3.3.3	<i>In-vivo</i> validation	43
3.4	Biopotentials recording validation	45
3.4.1	Micro-ECoG implants	45
3.4.2	<i>In-vivo</i> validation in rodent	46
3.4.3	<i>In-vivo</i> validation in Pig	50
3.5	Discussion	52
3.6	Conclusion	54
3.7	Contribution	54
4	Gallium thin film for high performance interconnects	55
4.1	Introduction	56
4.1.1	Motivation	56
4.1.2	Goal and specific aims	58
4.2	Intrinsically Stretchable Biphasic (Solid–Liquid) Au/Ga thin film	59
4.2.1	Deposition and characterization methods	59
4.2.2	Composition of the film	60
4.2.3	Role of the Au underlayer :	62
4.2.4	Growth of biphasic thin film	63
4.2.5	Surface topography of the film	64
4.2.6	Electromechanical properties	65
4.2.7	Applications	71
4.2.8	Evidence of gallium corrosion	73
4.2.9	Thiol self-assembled mono-layer as corrosion barrier	74
4.3	Engineering the surface of PDMS for smooth tailored liquid metal stretchable thin films	77
4.3.1	Wetting of textured substrates	77
4.3.2	Micro-structured PDMS fabrication	79
4.3.3	Gallium evaporation on super-lyophilic substrate	80
4.3.4	Imbibition condition	81
4.3.5	Growth of liquid gallium film on micro-structured substrate	82
4.3.6	Electromechanical properties	83

4.4	Discussion	84
4.5	Conclusion	86
4.6	Contribution	87
5	Conclusion and outlook	89
5.1	Summary and impact of the work	89
5.2	Future developments and challenges	90
A	Appendix	93
A.1	Soft e-dura materials and fabrication process	93
A.1.1	Interconnects	93
A.1.2	Electrical passivation layer	93
A.1.3	Encapsulation	94
A.1.4	Soft platinum-silicone composite preparation and patterning	94
A.1.5	Microfluidic and connector integration	94
A.1.6	Release	95
A.2	Compression modulus of the hydrogel	97
A.3	Mechanical spinal cord surrogate model fabrication process	97
A.3.1	Dura surrogate	97
A.3.2	Spinal cord tissue surrogate	98
A.3.3	Assembly of surrogate	98
A.4	Micro-Computed Tomography	98
A.4.1	Micro-Computed Tomography of spinal cord surrogate model	98
A.4.2	In-vivo micro-computed tomography of implants	99
A.5	Histology and Morphology of explanted spinal cord	100
A.5.1	Immunohistochemistry protocols	100
A.6	Surgical procedures complement	100
A.6.1	Implantation of electrodes to record muscle activity	100
A.6.2	Spinal cord injury	100
A.6.3	Rehabilitation procedures after spinal cord injury	101
A.6.4	Implantation of e-dura into the cortical subdural space :	101
A.7	Calibration of gallium evaporation and computation of the Ga/Au atomic ratio β	102
A.8	Multilayer assembly	102
A.9	Lift-Off Patterning of Biphasic Gold–Gallium Thin Films	103
	Bibliography	119
	Curriculum Vitae	121

List of Figures

1	The Meninges	2
2	Example of clinical ECoG implants	4
3	Example of clinical spinal cord surface implants	5
4	Illustration of the e-dura spinal cord implant	7
1.1	Platinum-PDMS mesocomposite as neural electrode coating	12
2.1	Functional electrical stimulation of the spinal cord to improve motor control after spinal cord injury	17
2.2	Stress-stretch curves of rat spinal dura mater	18
2.3	Spinal cord curvature in freely behaving rat	20
2.4	Soft and stiff rat spinal cord implant	21
2.5	Assembled spinal cord surrogate inserted with a stiff polyimide implant	22
2.6	Micro-computed tomography of spinal cord surrogate models at relaxed state	23
2.7	Effect of bending deformations on spinal cord surrogate model	24
2.8	Micro-computed tomography of spinal cord surrogate models conforming a radius of curvature of 27 mm	25
2.9	Effect of uni-axial stretch on spinal cord surrogate model	26
2.10	Orthoses and surgical procedures for chronic e-dura implantation	27
2.11	Kinematic evaluation of biointegration	28
2.12	Long term integration of soft e-dura implant	29
2.13	Spinal cord morphology evaluation	29
2.14	Neuro-inflammation evaluation	30
2.15	Wrinkling of a paper sheet subject to biaxial bending	31
2.16	Stiffening of sheet of paper by transversal bending	31
3.1	Stretchable micro-cracked gold thin film	36
3.2	Second generation process flow for soft e-dura implant assembly	39
3.3	Pictures from the assembly of a soft e-dura ECoG	39
3.4	e-dura implant for spinal FES in rat	40
3.5	In-vitro validation of stimulation e-dura implant	41
3.6	Impedance spectroscopy of the soft electrodes under cyclic stretching to 20% strain.	42
3.7	Evolution of electrodes impedance <i>in-vivo</i>	43

List of Figures

3.8 FES for spinal cord rehabilitation	44
3.9 e-dura micro-ECoG implants	45
3.10 Micro-ECoG recordings of light evoked potentials on mouse expressing Channelrhodopsin-2.	46
3.11 Chronic ECoG surgical procedure	48
3.12 Analyse of recorded micro-ECoG signals during unconstrained walking compared to standing rats	49
3.13 Picture of ECoG grids on pig cortex	50
3.14 Comparison between electrocorticograms recorded with clinical grid (a) and e-dura micro-ECoG (b)	51
3.15 Evoked cortical activation maps after snout electrical stimulation	52
4.1 Example of gallium printing techniques	58
4.2 Biphasic Au/Ga thin film	60
4.3 EDS-SEM analysis of the gold-gallium films.	61
4.4 X-Ray diffraction analysis of biphasic gold-gallium thin film.	62
4.5 Thermal evaporation of gallium on bare and gold-coated PDMS substrates	63
4.6 Growth of biphasic gold-gallium thin films on a PDMS membrane.	64
4.7 Wetting angle of gallium AuGa ₂ /Ga biphasic thin film on unstructured PDMS	65
4.8 Preparation of samples for electromechanical characterization	66
4.9 Electromechanical response of biphasic gold-gallium films under large uniaxial deformation	67
4.10 Electromechanical metrics of biphasic thin film	68
4.11 Robustness of biphasic thin film	69
4.12 Maximal current and current concentration in biphasic film	70
4.13 LED integration	72
4.14 Multilayered biphasic thin film assemblies	72
4.15 Evidence of Au/Ga biphasic passive skin breakdown and corrosion in prolonged exposition to phosphate-buffered saline (PBS)	73
4.16 Alkanethiol SAM	74
4.17 Alkanethiol SAM on Au/Ga biphasic film	75
4.18 Thiol SAM as corrosion barrier	76
4.19 Wetting on micro-structured substrate.	78
4.20 Pinning Condition	79
4.21 Micro-structured PDMS substrate created by soft-lithography	79
4.22 Effect of micro-structured substrate on gallium thin film topology	80
4.23 Influence of the micro-texture geometrical parameters on imbibition regime.	81
4.24 Growth of liquid gallium film on micro-structured substrate	82
4.25 Electromechanical response of biphasic gold-gallium films on micro-structured substrates under large uniaxial deformation	83
4.26 Sheet resistance of biphasic film on structured substrate	84
4.27 Gallium thin film as sensors	85

4.28 Evaporated gallium on micro-trenches	85
5.1 Complex morphologies generated by biomimetic 4D printing	91
A.1 Soft neurotechnology for e-dura implants	96
A.2 Evaluation of gelatin stiffness for spinal cord surrogate	97
A.3 Calibration of gallium evaporation and computation of the Ga/Au atomic ratio β .102	
A.4 Micropatterning of biphasic gold-gallium conductors on PDMS substrates with lift-off processing	103



List of Tables

1.1	Experimental measurements of dura mater elastic modulus	9
2.1	Ogden hyperelastic model parameters for rat spinal dura mater tissue	19
2.2	Implant mechanical properties	21

Introduction

Implantable neuroprostheses are engineered systems designed to study, support or replace an impaired function of the nervous system. They rely on neural recording or stimulation capabilities performed by a neural interface that enables the transduction between neural and electronic signals.

Some neuroprosthetic systems have already proven to be life-changing therapy and are now commonly used in clinic. Deep brain stimulators (DBS) are significantly increasing the quality of life of patients with Parkinson's disease by decreasing symptoms and enabling reduction of medication and associated side effects. Cochlear implants restore sufficient degree of hearing to enable the understanding of speech for deaf patients with damages to their sensory hair cells. More than 200,000 people have benefited from cochlear implants and they are now commonly implanted in infants, creating a need for systems able to maintain function over the patient lifetime.

Numerous other strategies have given promising preliminary results without having been translated to the clinic yet. In particular, brain computer interfaces (BMIs) enable to control external machines like robotic arms by decoding brain activity. They have great therapeutic potential for patients suffering from tetraplegia or locked-in syndrome. If these new replacement strategies and restoration treatments hold very strong promises, there are also creating a demand for new devices and a series of challenges to overcome in order to achieve integration of different functions within a functional system for chronic use.

A persistent challenge for translating neuroprosthetics from laboratories to clinic is the difficulty to provide a neural interfaces that combine high spatial and temporal resolution, and long-term biointegration and stability. Neural interfaces designed for the surface of the nervous system offer a trade-off between invasiveness and spatiotemporal resolution and are particularly promising for neuroprosthetic applications.

In this chapter I will give a brief introduction on the central nervous system and the clinical use of neural implants designed for its surface. Challenges and opportunities associated with the development of chronic multi-modal surface neural interfaces will then be discussed. After defining the concept of electronic dura mater (e-dura), I will give the objectives and outline of the thesis.

The Meninges and surface of the central nervous system

The central nervous system (CNS) is often described as the most complex organ of the human body. It coordinates thought processes, emotion, cognitive, motor and vegetative functions. The CNS is composed of the brain, enclosed in the cranial cavity, and the spinal cord housed in the spinal canal, ranging from the base of the skull to the tail bone. The brain integrates, processes and coordinates sensory cues from different organs and initiates commands that are then sent to the rest of the body. The spinal cord transmits the nerve signals bidirectionally to the trunk and limbs through 31 pairs of spinal nerves. The spinal cord also hosts neural circuits that coordinate many reflexes and central pattern generators.

The CNS is a vital and fragile organ and is therefore well protected from external aggression by several barriers :

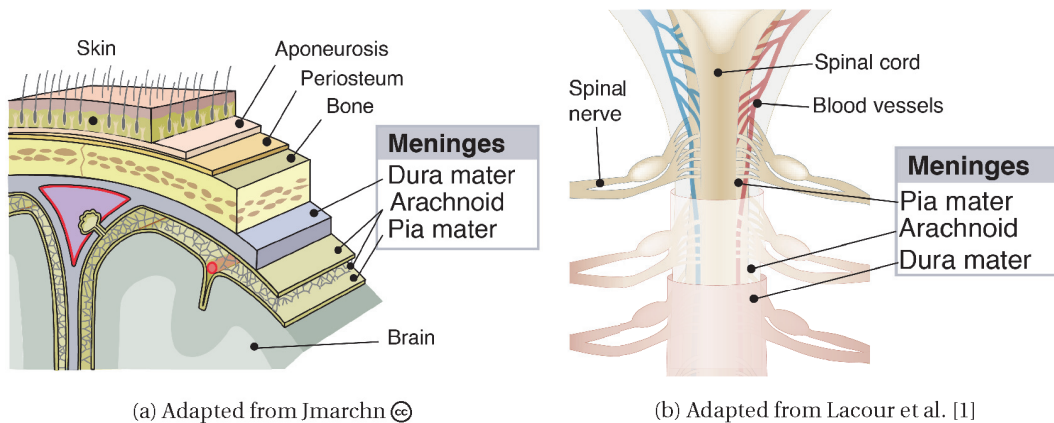


Figure 1 – The Meninges

a - Schematic representation of the meninges at the brain level. **b** - Schematic representation of the meninges at the spinal cord level.

The skull and vertebrae : The first barrier consists of the bones that surrounds the CNS. The skull and vertebrae provide a protection against shock and structural support for the brain and spinal cord respectively.

The meninges : The brain and spinal cord are enveloped by three membranes that offer a second battery of protections against mechanical aggression, viral attacks and chemicals.

- **Dura mater :** The most external membrane is the dura mater. It is the thicker and tougher of the three meningeal membranes and is composed mainly of collagen fibers.
- **Arachnoid mater :** The second membrane, is the arachnoid mater. The arachnoid mater has a web like structure and is normally fused to the dura mater. This thin and fragile membrane is vascularised and acts as a sealant to retain the cerebrospinal fluid in the subarachnoid space.

-
- **Pia mater :** The inner-most layer is the pia mater. It is a very thin membrane (less than 100 μm in human) and the softest of the three meningeal membranes. The pia matter tightly follows the circumvolutions of the brain and the surface of the spinal cord .

Cerebrospinal fluid (CSF) : CSF is the liquid that occupies the subarachnoid space between the arachnoid and pia mater. The CSF maintains the CNS in neutral buoyancy and acts as a liquid shock absorber. The CSF also plays an important role in brain homeostasis and its lymphatic system.

Blood Brain barrier : The extracellular fluid in the central nervous system is separated from the circulating blood by a selectively permeable membrane. This barrier is formed by tight junctions of endothelial cells that prevent the diffusion of large or hydrophilic molecules and potential infectious attacks to the CSF while allowing diffusion of hydrophobic small molecules and glucose.

Surface implants for the CNS

Among the different approaches used by neurologists and neurosurgeons to establish diagnosis and treat patients suffering from neurological disorders, some require to access the surface of the CNS and disrupt part of the aforementioned protective barriers. In this section we give examples of implants used in hospitals, designed to access the surface of the CNS and discuss the opportunities and challenges offered by surface implants to develop next-generation treatments.

Clinical use of brain surface implants

Electrocorticography (ECoG) : ECoG electrode arrays are used in hospitals to record biopotentials or to deliver electrical stimuli to the surface of the brain. Their principal clinical applications are the detection of epileptogenic zones and cortical stimulation mapping in order to plan surgical procedures. ECoGs are used either intraoperatively or implanted for a short period (< 30 days) for extraoperative experiments. Following a craniotomy, the electrode array is either placed over the dura mater (epidural ECoG) or below the dura (subdural ECoG) as shown in figure 2a. In contrast to conventional electroencephalography (EEG), this invasive procedure provides a higher spatial, temporal resolution and signal to noise ratio [2].

Emerging applications for brain surface implants

Brain machine interfaces (BMIs) : BMIs are exploring the potential of reading and decoding brain activity in order to control external machines like robotic arms and computers. BMIs have been successfully implemented in non-human primates and paralysed patients allowing them to perform daily life activities like grasping tasks with a robotic arm assistance [3, 4].

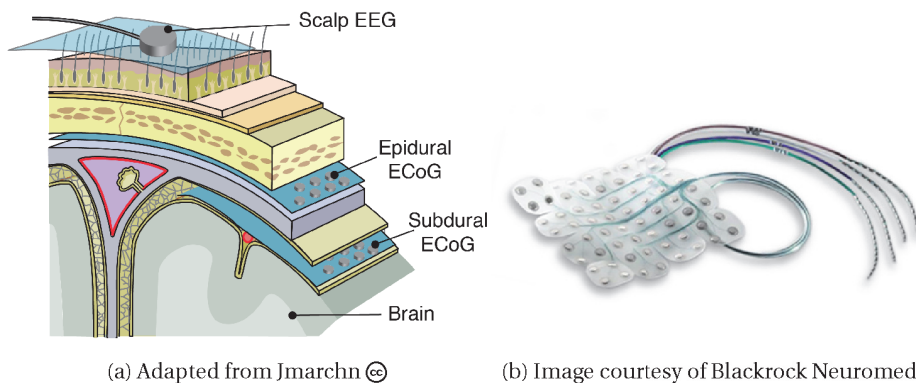


Figure 2 – Example of clinical ECoG implants

Most successful demonstration, of BMI have been using brain penetrating electrodes to record local field potential or single neuron activity within the brain tissue. These devices are extremely invasive but provide the highest spatial and temporal selectivity and enable advance BMI applications [5]. However, the long-term stability of this type of electrode is a major issue [6, 7] and micro-movements between the brain and interface trigger high variability of the signals which can be problematic [8]. ECoG has emerged as a promising alternative to intraparenchymal electrodes for BMI. Indeed it provides balance between invasiveness and spatiotemporal resolution [9–12].

Responsive neurostimulation (RNS): RNS is a promising new approach to treat certain types of epileptic seizures. Their principle relies on the detection of the onset of a seizure by recording and decoding electrocorticographic signals recorded with chronically implanted ECoGs and delivering stimulation to abort propagation of the seizure [13, 14]. For example, the Neuropace RNS[®] system has recently received FDA approval and is currently under clinical trials [15].

Clinical uses of spinal cord surface implants

Spinal cord stimulation (SCS) for chronic pain : SCS is commonly used in clinic to treat patients suffering from severe neuropathic pain [16]. When classical therapies remain unsuccessful, an electrode array can be implanted in the epidural space. Localized delivery of electrical stimuli to the spinal cord helps to alleviate the perceived pain sensation and reduce effective analgesic drug intake and associated side effects. The electric pulses are provided by an implantable pulse generator (IPG) connected to a surface electrodes array as shown in figure 3b. Each year, around 14,000 patients around the world receive a spinal cord stimulator.

Intrathecal drug delivery for chronic pain: An alternative approach to treat severe chronic pain consists of using an intrathecal drug delivery system [17]. Opioids such as morphine

are very efficient for relieving pain but are also associated with strong adverse side effects. While systemic delivery is often given in a first approach, intrathecal delivery bypasses the blood-brain barrier by infusing the drug directly in the CSF and thus reducing drug dose and associated side effects.

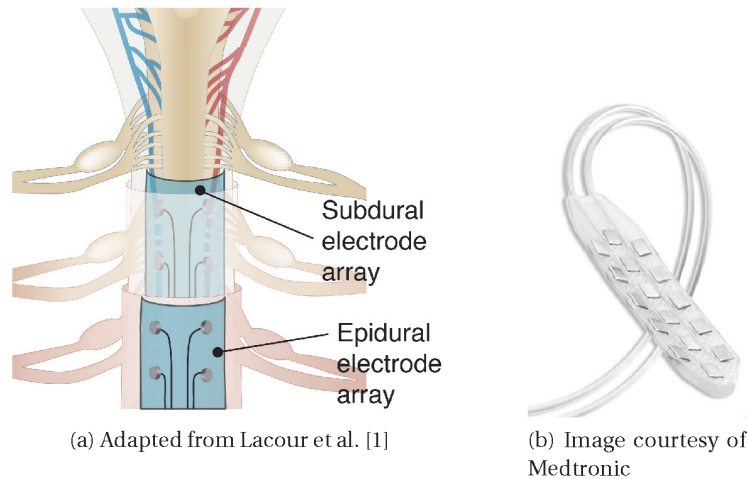


Figure 3 – Example of clinical spinal cord surface implants

Emerging application for spinal cord surface implant

Improving motor control after spinal cord injury : Recently functional spinal cord electrical stimulation (FES) has gathered significant interest for improving motor control and rehabilitation after spinal cord injury. After a traumatic event on the spinal cord, the neural connections between supraspinal centers and lumbar spinal circuits can be damaged resulting in partial or total lower limb paralysis. Even though lumbar circuits below the injury remain functional, these lack the excitation and modulation stimuli coming from the brainstem to allow control for activities such as standing and walking. A promising neuroprosthetics approach consists of replacing the missing brain inputs by a combination of chemical and electrical stimuli delivered by an implant directly to the segment of the spinal cord below the injury [18] . Eventually the spinal neural prosthesis would work in conjunction with a brain interface able to decode the motor intention and trigger the delivery of stimuli on the spinal cord interface, effectively bypassing the injury. Recent studies have shown that lumbar spinal circuits can be reactivated by electrical stimulation in patients suffering from paraplegia [19, 20], however significant developments remain to be completed before achieving a functional chronic brain/spine neuroprosthetic device.

Challenges for surface implant

While these emerging applications hold very strong promises, they are also creating a demand for reliable chronic neural interfaces. Yet, several technical challenges lie ahead of the

development of these next generation treatments:

Conforming to the CNS geometry and dynamics

For stable and reliable bidirectional transduction of signals, surface implants should conform as much as possible to the geometry and dynamics of the CNS. The brain has a complex convoluted geometry with many folds forming grooves (*sulci*) and ridges (*giri*). A substantial portion of its surface is thus difficult to access with conventional clinical surface implants, preventing recording or stimulation of many regions of interests.

Moreover, the brain and spinal cord are not static organs. They experience dynamic deformations during normal activities. Postural movements can result in large strain ($\sim 15\%$) in the spinal cord [21]. The brain is highly vascularised and displays significant micromotions ($\sim 30\text{ }\mu\text{m}$ in rodent [22], $\sim 500\text{ }\mu\text{m}$ in human [23]) due to vascular pulsatility and respiration [24]. Relative movements between dynamic tissues and rigid electrodes trigger variability in the recorded neural signals [8] and can impede the surrounding tissue.

Biointegration

One of the main remaining challenges before being able to achieve a functional chronic system is the difficulty to provide stable neural platforms for extended periods of time. In contrast to bone tissue that can develop an intimate contact with bone implants through the osseointegration process [25], neural tissue in direct contact with rigid implant degrades with time, forming scar tissue encapsulation [26] and limiting the functionality of these devices on the long-term basis [27].

The natural foreign body inflammatory response is one of the main causes for device failure. Inflammatory cells reactions create hostile chemical environment that can lead to oxidation and corrosion of the implanted device [28, 29]. First inflammatory reaction is due to the mechanical trauma resulting from implant insertion and disappears after the first weeks leading to a chronic inflammatory reaction [30]. This reaction is characterized by the presence of both reactive astrocytes, which form a glial scar, and activated microglia [26].

One of the current hypotheses is that the mechanical mismatch between neural devices and neural tissue plays a significant role in the neuroinflammatory response [31]. Recently, Capadona et al. have shown that mechanically compliant implants can reduce the neuroinflammatory response in comparison to stiffer systems [32]. Thus, the development of soft neural interfaces may improve the long-term stability of implanted neural electrodes.

Electrode density

Emerging neuroprosthetics and BMIs will require high density sub-micrometric electrode arrays to achieve high spatial resolution. The fabrication and electrical routing of these electrode arrays is a persistent technological challenge. One promising approach consists of using techniques imported from the microfabrication industry to deposit and pattern thin metal films with micrometric precision on silicon or polymeric substrates [33, 34]. Yet, routing of interconnects resulting from these planar processes and connection with standard

implanted electronic remains challenging.

Electronic dura mater

In this thesis, I develop the concept of *electronic dura mater* or *e-dura*. The e-dura consists of a soft neural interface that mimics the mechanical properties of the dura mater. In contrast with standard neurotechnologies, the e-dura is made of soft and stretchable materials able to conform to the complex geometry of the CNS and follow its dynamical deformation without impeding the surrounding tissue and limiting long term foreign body reaction. The e-dura can serve as a multimodal neural platform designed for the surface of the CNS and can integrate neurostimulation, recording and drug delivery capabilities depending on the application needs. Figure 4 shows an illustration of an e-dura implant for the spinal cord with drug delivery and electrical stimulation capabilities.

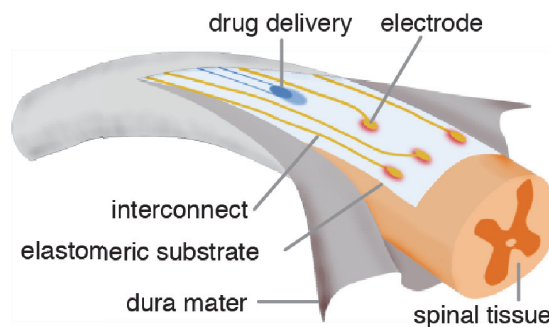


Figure 4 – Illustration of the e-dura spinal cord implant

Objectives of the thesis

This work aims to improve existing soft neural interface technologies by :

- developing deposition and patterning techniques for producing stretchable metallic electrodes and interconnects enabling fabrication of an e-dura implant on a soft elastomeric substrate.
- characterizing the obtained conductors and electrodes.
- implementing these conductors to fabricate implants that approach the mechanical properties of dura mater.
- evaluating the stability and performance of these implants in *in-vitro* environments.
- evaluating the biocompatibility and functionality of these implants in *in-vivo* environments.

Outline of the thesis

In the first chapter of the thesis, I will present the specifications and different components of e-dura implants and I will give an overview of the state of the art of soft neurotechnologies. In the second chapter, I will evaluate the biointegration of soft implants designed to approach the mechanical properties of dura mater. The third chapter will cover the functional demonstration of e-dura implants using micro-cracked stretchable gold metalization. In the fourth chapter I will explore the use of gallium liquid metal to create highly conductive and stretchable interconnects enabling integration of active components in an e-dura platform.

1 Technical specifications, components and soft neurotechnologies for e-dura implants

In this chapter, I will describe the technical specifications, components and available technologies for the design of e-dura soft neural interfaces.

1.1 Technical specifications for e-dura neural interfaces

Mechanical Specifications

E-dura implants should be designed to approach the mechanical properties of dura mater. Dura mater is a soft biological tissue composed mainly of collagen and elastin fibers organized in successive parallel planes called laminae. In humans, the dura mater consists of ~ 80 laminae for a total thickness of $\sim 270\mu\text{m}$ [35,36].

Biomechanically, the dura mater behaves as an anisotropic viscoelastic material and is influenced by the orientation of its constituent fibers. Collagen fibers in dura mater are primarily orientated along the craniocaudal direction resulting in a greater tensile strength and stiffness in the longitudinal direction [37,38].

Tissue	Species	Mechanical modulus	Test mode	Ref.
Lumbar dura mater	Human	E=65 MPa to 103 MPa	Longitudinal 1D-tension	Runza et al. [38]
Lumbar dura mater	Human	E=4 MPa to 8 MPa	Circumferencial 1D-tension	Runza et al. [38]
Spinal dura mater	Cat in vivo	E=2 MPa	Longitudinal 1D-tension	Chang et al. [39]
Thoraco-lumbar dura mater	Dog	E=0.4 MPa to 46 MPa	Longitudinal 1D-tension	Tunturi et al. [40]
Spinal dura mater	Rat	G=1.2 MPa	Longitudinal 1D-tension	Maikos et al. [41]

Young's Modulus (E), Shear Modulus (G)

Table 1.1 – Experimental measurements of dura mater elastic modulus

For slow deformation rates and limited elongation ($<10\%$) the dura mater is approximated as an isotropic material and the Young's Elastic modulus can be computed. The table above gathers experimental measurements of dura mater mechanical properties found in the literature.

Chapter 1. Technical specifications, components and soft neurotechnologies for e-dura implants

Measured Young's elastic moduli ranged from 0.4 to 103 MPa.

E-dura implants must sustain the same range of deformations as their surrounding tissues. Spinal cord and meninges deform to follow postural movements. In particular, flexion of the spinal cord can result in localized stress and strain in the spinal cord and meninges. Harrison et al. [42] compiled different publications and reported that largest strain occurred with flexion movements with local strain larger than 15%.

In this work, I will use implement elastic materials like silicone elastomers to design dura-like implants able to sustain repeated deformation including uni-axial tension up to 20% applied strain.

Functional specifications

Depending on the targeted application, the e-dura platform integrates the capability to record biopotentials, deliver electrical or light stimuli and deliver drug locally through a micro-catheter (chemtrode). These functions are performed by biotransducers that are described in section 1.2.2.

Biocompatibility and expected lifetime

Translation of e-dura implants to clinical use will require e-dura devices and its constituents to meet biocompatibility standards and regulatory requirements for the intended clinical use. Guidelines for biocompatibility assessment are provided by the Organization for Standardization (ISO 10993) and FDA (blue book memorandum § G95-1). For prolonged contact (> 30 days) with tissue or bone, required biocompatibility tests include cytotoxicity, sensitization, genotoxicity, chronic toxicity and carcinogenicity among others.

Moreover, e-dura neural platforms are particularly promising for neuroprosthetics applications. In these cases the neural platform would need to be used chronically to restore a lost sensory or motor function in the patient and thus is expected to be implanted permanently and maintain function over several decades. Eventually the implant should be easily retrieved or replaced in case of failure or complication.

Surgical specifications

The e-dura implant should be able to withstand the conditioning and handling required for its surgical implantation. Before surgery the device needs to be sterilized to remove any potent biological agents. Ethylene oxide gas treatment is the most suitable technique considering the materials used. Eventually the devices need to be handled by the surgeon. The implant may experience significant mechanical stresses during implantation procedure. For example, insertion of a spinal e-dura implant in the subdural space requires the implant to be folded

and inserted through small openings and pulled along the spinal segment, as detailed in section 2.3.1. The strain experienced by the device during such a procedure is difficult to quantify and might vary with surgeon skill and practice.

1.2 Basic components for e-dura neural interfaces

E-dura implants are composed of the following elements :

- The **substrate** provides the mechanical integrity to the implant and sets the overall geometry and compliance of the device.
- The **biotransducers** perform the intended functions. It includes **electrodes** for biopotentials recording and electrical stimulation but also **optrodes** for optical stimulation and **chemotrodes** for drug delivery.
- The **interconnects** interface the biotransducers to their controlling units such as implantable stimulation and recording electronics.

1.2.1 Substrate

Silicone elastomers are commonly used for medical applications including for long-term implantable devices (breast implants, hydrocephalic shunts) and have emerged as a promising substrate for the fabrication of soft neural interfaces like e-dura implants.

Polydimethylsiloxane (PDMS) is a type of silicone polymer with the formula $[\text{O}-\text{Si}(\text{CH}_3)_2]_n$. These elastomers are rather soft with a Young's modulus in the range of 500 kPa to 2 MPa depending on their formulations and can sustain large strains (>100%).

In addition to their biocompatibility and chemical stability, these silicone elastomers are particularly convenient for the fabrication of micro assembled devices. Thanks to their low liquid surface tension (~ 20.4 mN/m), they can be fabricated into thin films which can be further covalently bonded to one another after oxygen plasma activation [43]. Finally, PDMS is optically transparent from 240 to 1100 nm making it also perfectly suitable for combination with optoelectronic devices.

In this work, I primarily use Sylgard 184 (Dow Corning) for practical reasons. This commercially available PDMS is particularly popular in the academic environment and easily available in clean room. Despite the fact that this PDMS is not a medical grade silicone, the developed processes and results presented in this thesis should be easily translated and reproduced on medical grade silicone.

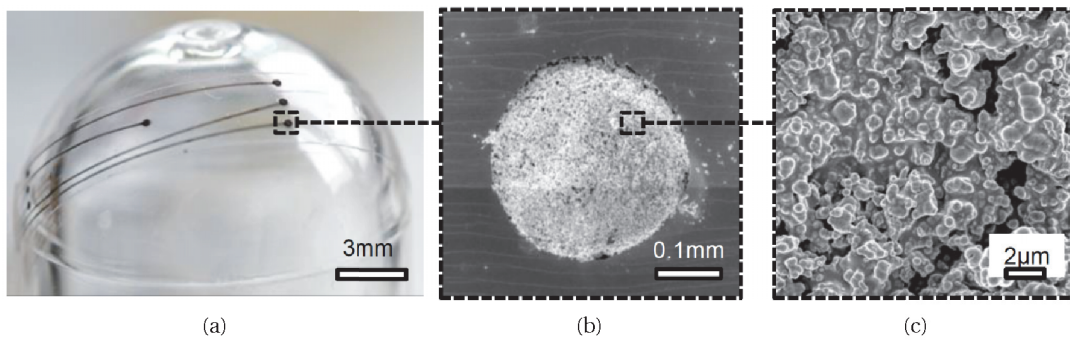
1.2.2 Biotransducers

Electrodes

Electrodes enable the recording of biopotentials by transducing ionic currents into electronic signals and to stimulate neural tissue by establishing ionic currents between two or more electrodes. The transduction from electron flow in the metallic electrode to ion flow in the tissue can result either from capacitive reactions involving charging and discharging of the electrode-electrolyte double layer or from faradaic reactions involving charge transfer and redox reactions [44].

Surface electrodes record signals called local field potentials (LFP) that represent the summed ionic currents within a small volume of neural tissue at the vicinity of the electrode. ECoG grids used in hospitals for identifying epileptogenic foci typically feature millimetric size electrodes with large inter-electrode spacing (~ 1 cm) and lack the spatial and temporal resolution required for BMI applications compared to intracortical micro-electrodes. Micro-ECoGs with closely packed (~ 1 mm) sub-millimetric size electrodes are able to record neural activity at the scale of cortical columns and are particularly promising for neural prosthetic applications [10, 45, 46]. Recording electrodes are usually characterized by their impedance at 1 kHz. Typically ECoG electrodes exhibit impedances in the range of $\sim 100 \Omega$ while micro-ECoG have impedances ranging from 1 k Ω to 1 M Ω , depending on the size and material of the electrode [10].

Stimulation electrodes usually use biphasic current pulses to initiate depolarization of surrounding excitable cells. Charge balanced waveforms and restricting the applied potentials within the water window limits degradation of the electrode caused by irreversible faradaic reactions. In particular, large potentials can lead to water electrolysis and formation of reactive gases (O_2, H_2) that can damage both electrode and surrounding tissue.



Adapted from Mineev et al. [47]

Figure 1.1 – Platinum-PDMS mesocomposite as neural electrode coating

a - Electrode array on PDMS substrate with platinum-PDMS mesocomposite electrodes. **b** - Low magnification scanning electron micrograph (SEM) of the composite coating pasted on a 300 μ m electrode. **c** - High magnification SEM of the porous micro-structure of the mesocomposite.

1.2. Basic components for e-dura neural interfaces

Noble metals like platinum (Pt) or platinum-iridium alloy (Pt-Ir) are preferred for electrodes as they allow charge injection by both capacitive and reversible faradic reactions [48]. These metals are, however, rigid ($E = 168 \text{ GPa}$) and can therefore not be directly used in their bulk form for e-dura devices. Emerging soft and flexible materials for electrodes include carbon nanotubes [49, 50], silicone-metal composites and electrically conduction polymers such as PEDOT:PSS [51–54].

In this work, I use a platinum-PDMS meso-composite as electrodes for e-dura implants (see figure 1.1). The process developed by Minev et al. [47] enables fabrication of electrodes that combine mechanical compliance, robust mechanical integration with the PDMS substrate while maintaining the electrochemical properties of platinum. The composite material is obtained by mixing silicone elastomer with micrometric platinum powder ($\sim 1 \mu\text{m}$) in a ratio allowing for percolation of metallic particles.

Optrodes

Neurons can be genetically modified to express light-sensitive ion channels (opsins) on their membrane using techniques referred as optogenetics [55, 56]. Shining light at a wavelength specific to the expressed opsin triggers opening of the light sensitive ion channels. Optogenetics has several advantages over electrical stimulation, such as cell-type specificity, sub-millisecond temporal resolution and absence of electrical artifacts [57]. Typically, optogenetics application requires light power ranging from a couple to tens of mW/mm^2 [58].

Optodes enable local light delivery to neural tissue. Integration of local light delivery capability in a implant can be achieved either by integration of light emitting diodes (LEDs) or optical wave guides connected to an external source [59]. Integration of optrodes in soft and stretchable substrate like silicone is a real challenge as LEDs need significant currents ($>1 \text{ mA}$) which require stretchable and highly conductive electrical interconnects.

Chemotrode

In the context of this thesis, a chemotrode enables to modulate activity of the CNS by locally delivering locally drug through a micro-catheter integrated within the e-dura platform. For example a chemotrode can deliver agonists to specific neural receptors located in well defined spinal cord regions in order to mimic the modulating influences of brainstem inputs [60]. Micro-channels can easily be fabricated and integrated within the silicone substrate using micro-moulding techniques [61].

1.2.3 Stretchable interconnects

E-dura implants require stretchable electrical interconnects to carry electronic signals and power to electrodes and distributed active components (e.g. LEDs). Realizing electronic conductors on a soft and stretchable substrate like silicone is a challenging problem that has attracted the attention of the scientific community throughout the past decade. Indeed, stretchable conductors find applications in many domains including bioelectronics [62],

Chapter 1. Technical specifications, components and soft neurotechnologies for e-dura implants

wearable electronics [63] and soft robotics [64].

Conventional electronic conductors such as metals or conductive oxides tend to fracture at low strains (<5%). Consequently processes like the ones used in the industry to create electrical circuits on silicon or epoxy composite (FR-4) can not be directly translated to soft substrates.

The first class of stretchable conductors uses conventional **solid conductors** where the stretchability is engineered by geometric designs at the nano-, micro- and macrosopic scales :

- Patterning metal thin films on meander shaped susbstrates [65–67] or pre-stretched substrates [68,69] allows the electrical conductor to accommodate large deformations by deflecting out of plane. However, integration of these constructs on soft substrates is complex, and the engineered elasticity is usually limited to predefined directions.
- Engineering micro-cracks [70] or nano-mesh [71] in thin metals films are an efficient strain relief approaches enabling reversible, multiaxial-stretchability to tens of percent. These conductors display electrical conductivity much lower than continuous metal films of similar thickness.
- Blending conductive polymers, particles or nano wires [72–76] with an elastomeric matrix enables to form conductive and stretchable composites that rely on the percolation and relative motion of the fillers. These approaches enable tailored, multiaxial elastic conductors but associated patterning and contacting techniques can be challenging.

The second class of stretchable conductors uses **conductive liquids** enclosed in soft elastomer to create highly deformable assemblies:

- Liquid metals can flow and rearrange and are consequently intrinsically stretchable electrical conductors. Gallium and gallium based alloys [77] are room temperature liquid metals and provide a non toxic alternative to mercury. However patterning and manipulation of these metals can be challenging due to their uncommon rheology [78].
- Ionic liquids are very resistive conductors and require complex encapsulation. However they can be useful for very specific applications [79–81].

In this work, I selected gold micro-cracked thin film [82] to realize soft interconnects for functional recording and stimulation e-dura devices as detailed in chapter 3. The interconnects are formed in vacuum by thermal evaporation of gold on silicone substrate. The resulting gold film (25 to 80 μm) is particularly suited for the design of e-dura implant as it gathers sufficient electromechanical properties (10 to 100 Ω/\square), good biological compatibility and requires a rather simple process.

Additionally, I explore the use of gallium liquid metal to create highly conductive and stretchable interconnects enabling integration of active components in an e-dura platform as detailed in chapter 4.

2 Soft substrate for long term biointegration of e-dura implant

One of the main hypotheses to explain the difficulty to provide stable neural platforms over extended periods of time, is the considerable mechanical mismatch between implants and neural tissues. In this chapter, I evaluate the hypothesis that surface implants designed to mimic the static and dynamical mechanical properties of targeted tissues display better long-term biointegration. This hypothesis is tested through the case study of a spinal cord implant designed for rat animal model. First I evaluate the mechanical and dynamical behavior of a soft silicone e-dura implant compared to standard stiff plastic technology, in an *in-vitro* surrogate model of the spinal cord. Then the long term biointegration of both implants is comparatively investigated on Lewis rats.

This chapter is adapted from the following publication:

[83] MINEV*, Ivan R., MUSIENKO*, Pavel, HIRSCH, Arthur, et al. Electronic dura mater for long-term multimodal neural interfaces. *Science*, 2015, vol. 347, n° 6218, p. 159-163.

2.1 Introduction

2.1.1 Motivation

Context

Mechanical mismatch between implants and neural tissue is one of the main hypotheses to explain the lack of long-term biointegration of neural platforms [32]. Neural tissues are one of the most delicate tissues in the body. They are extremely soft, featuring Young's moduli in the kPa range [84]. In contrast, most clinical implants are made of materials like metals or silicon that have Young's moduli in the GPa range. As a result they exhibit very small levels of compliance and are unable to conform to the complex geometries of the CNS and follow micromovements.

To address this problem flexible bioelectronic interfaces are being developed using polymers like polyimide, parylene or SU-8 as substrate and metal layer deposition techniques imported

Chapter 2. Soft substrate for long term biointegration of e-dura implant

from the microfabrication industry. If these polymers also exhibit Young's moduli in the GPa range, flexibility and conformability can be achieved by using ultra thin film (1 to 25 μm).

Polydimethylsiloxane (PDMS) silicone rubber has emerged as a promising alternative substrate for soft neural interfaces. This biocompatible material is much softer than conventional polymers used in neuroprosthetics. Typically, PDMS silicone have Young's Modulus in MPa range and can withstand large deformations (>100%).

2.1.2 Goal and specific aims

Goal

The overall goal of this chapter is to test the hypothesis that surface implants designed to mimic the static and dynamical mechanical properties of targeted tissues display better long-term biointegration. This hypothesis is tested on the specific case study of a surface electrode array designed to conform to the rat spinal cord. Two different implants were selected and comparatively studied. A flexible but rather stiff implant fabricated from polyimide polymer corresponding to standard practices for flexible neural implants, and a softer implant made from silicone elastomer supposed to match the mechanical properties of natural dura mater.

Specific aims

The specific aims of the chapter are listed below:

- Evaluate the mechanical dynamical properties of natural rat dura mater.
- Build a mechanical surrogate of the rat spinal cord.
- Comparatively evaluate the mechanical and dynamical behavior of a soft and a stiff implant in an in-vitro surrogate model of the spinal cord.
- Comparatively investigate the long term biointegration of soft and stiff implants in an *in-vivo* rat model.

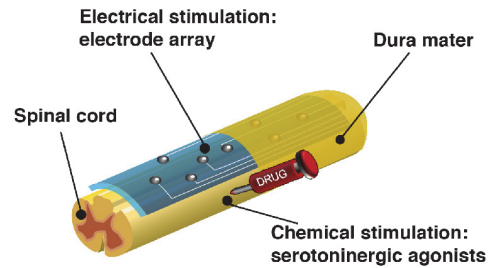
2.1.3 Case study

Collaboration with Courtine Group

The group of Grégoire Courtine is one of the groups working worldwide on the development of innovative interventions to restore motor functions after spinal cord injury and other central nervous system disorders. Their approach combines the use of robotic interfaces [85], functional electrical stimulation (FES) and chemical modulation of the spinal cord [86]. Figure 2.1a shows an example of a rat with spinal cord injury and severe paralysis regaining voluntary motor control of the lower limbs with the combination of electrical and chemical stimulation and robotic harness assistance. Working primarily in rodent and primate models, their work explores innovative strategies that can be translated for motor control in humans, such as realtime control of stimulation patterns based on the live kinematics [87] and fine spatiotemporal neuromodulation [88].



(a) Adapted from Vanden Brand et al. [89]



(b)

Figure 2.1 – Functional electrical stimulation of the spinal cord to improve motor control after spinal cord injury

a - Combination of electrical and chemical stimulation and robotic harness assistance enables to restore voluntary lower body movement in rats with spinal cord injury and severe paralysis. **b** - Schematic representation of spinal cord implant. The implant is located in the subdural space. A combination of serotonergic agonists and electrical stimulation of lumbar segments is used to wake up a dormant spinal column.

Subdural e-dura electrode array for the rat

In collaboration with the laboratory of Grégoire Courtine we developed a soft e-dura implant designed to be inserted below the dura mater as shown in figure 2.1b. The subdural location of the implant allowed for an intimate contact with the target tissue providing a better functional specificity and the opportunity to combine direct intrathecal drug delivery through a micro-channel integrated in the implant. We used this project as a case study for this chapter.

2.1.4 Mechanical properties and dynamics of natural dura mater in rat

In this section, the mechanical properties of natural rat dura mater are discussed. First, results of uni-axial tension tests on rat spinal dura mater tissue are reported, then the range of motions

of the spinal cord is evaluated in freely moving rats.

Rat dura mater stiffness measurement

Dura mater is a highly collagenous soft tissue and behaves as a visco-elastic material due to the presence of both collagen and elastin fibers. There is limited data in the literature reporting measurements of the mechanical properties of the rat dura mater. Maikos et al. [41] conducted uniaxial tension tests on spinal dura mater tissue of adult Long-Evans hooded rats. We performed similar tests on dura mater samples from the lumbar region of the spinal cord in adult Lewis rats, results are presented below.

Method: A section of rat dura mater was explanted from a 2-month old Lewis rat and cut to a strip with dimensions of 3.4 mm x 1 mm. Immediately post explantation, each end of the strip was secured to a glass cover slip using a fast acting cyanoacrylate adhesive. The cover slips were inserted into the clamps of a tensile testing platform (Model 42, MTS Criterion). Extension at a strain rate of $0.5 \text{ \%} \cdot \text{s}^{-1}$ was continuously applied until the dura mater sample failed. The thickness of the dura mater sample was determined from optical micrographs ($80\text{-}100 \mu\text{m}$). During the process of mounting and stretching, the dura mater sample was kept hydrated with saline dispensed from a micropipette.

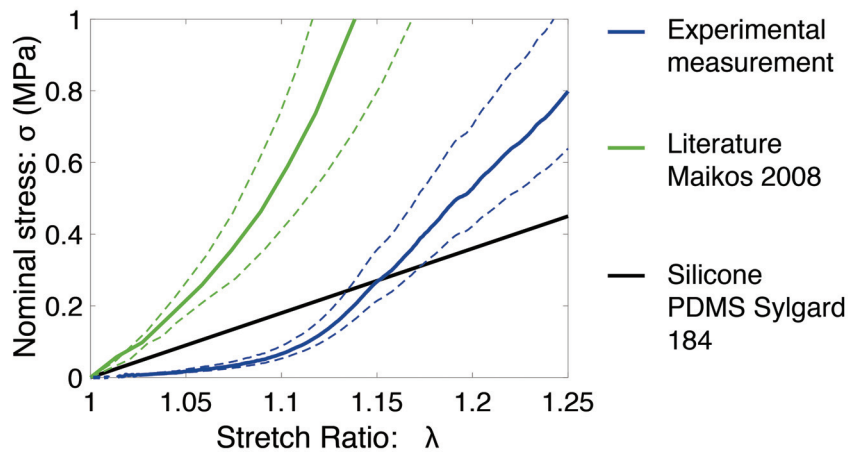


Figure 2.2 – Stress-stretch curves of rat spinal dura mater

Representative stress-strain curves from rat spinal dura mater (\pm standard deviation). The results from the current study are depicted in blue while the reference curve from Maikos 2008 [41] is depicted in green. As comparison the Stress-stretch curve of Sylgard 184 PDMS silicone is given in black. Adapted from [83].

Results: Obtained stress-stretch curves can be seen in figure 2.2. As comparison the stress-stretch curve of Sylgard 184 PDMS silicone is also presented. Dura mater samples showed

a non-linear stiffening as expected from collagenous soft tissues. The stress-stretch curve obtained experimentally shows a slightly softer behavior than Maikos results.

For slow deformation rates, Maikos et al. modeled the dura mater as a hyperelastic continuum solid. The behavior of the dura was described using a first order Ogden form of the hyperelastic strain energy potential function given by the following equation:

$$W = \frac{2G}{\alpha^2} (\lambda_1^\alpha + \lambda_2^\alpha + \lambda_3^\alpha - 3) \quad (2.1)$$

where G and α are material dependent parameters and λ_i are the stretch ratios in the different axes. In the case of uniaxial tension and assuming incompressibility, the nominal stress can be expressed as function of the stretch ratio using the following equation:

$$\sigma = \frac{2G}{\alpha} (\lambda_1^{\alpha-1} - \lambda_1^{-0.5\alpha-1}) \quad (2.2)$$

The identified parameters of the Ogden model are given in the table below:

Parameters	Maikos 2008 [41]	This study
$G(\text{MPa})$	1.20 ± 0.79	0.368
α	16.2 ± 9.74	15.71
R^2 for Ogden fit	0.98	0.98

Table 2.1 – Ogden hyperelastic model parameters for rat spinal dura mater tissue

Rat spinal cord range of motions

Rats are naturally exploratory animals. They like to climb on objects, crawl in tunnels and hide in their nest. During these movements the spinal cord of the rat is subjected to complex bending movements. These mechanical solicitations can be particularly challenging both for spinal implants and the surrounding tissues. The goal of this section is to evaluate the range of motion of the rat spinal cord in freely behaving conditions by measuring the maximal bending radius of curvature along the spinal cord. The measured radii of curvature will then define the bending limits applied to the spinal cord implant surrogate model presented in section 2.2.

Method : To measure the range of physiologically relevant vertebral column curvatures, we recorded spontaneous movement of a healthy rat during exploration of a novel environment. Reflective markers were attached overlying body landmarks to measure motion of the vertebral column. The position of the markers was recorded with 12 infrared cameras (200 Hz) and processed with Nexus software (Vicon) in order to obtain the 3D coordinates of the markers. The spinal cord was modeled as an interconnected chain of rigid segments, and joint angles were generated accordingly. Overlay of the camera image and reconstructed spinal segments

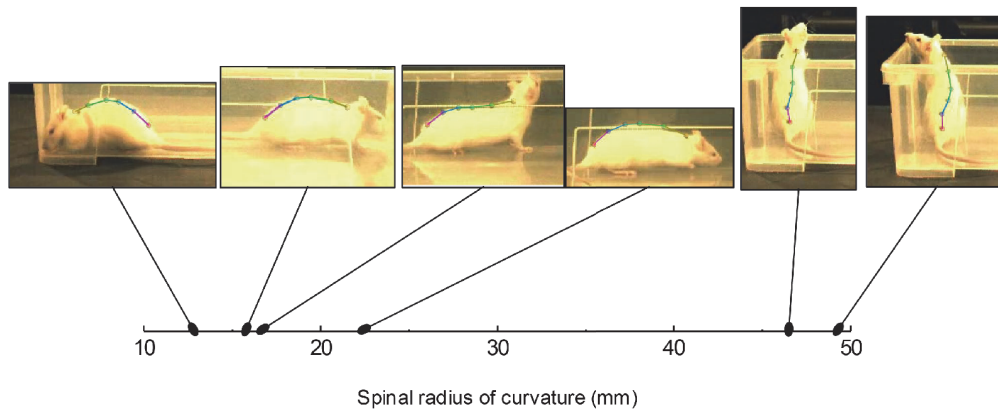


Figure 2.3 – Spinal cord curvature in freely behaving rat

Maximal radii of curvature along the spinal cord was evaluated in freely moving rat. Radii are reported along the axis and corresponding positions of the rat are depicted in insets. Adapted from [83].

are shown in figure 2.3 for different positions of the animal. For each position, we fitted a polynomial function through the inter-connected chain of markers using a custom MATLAB code and computed the maximal radius of curvature around the interpolated curve.

Results : The resulting curvatures are reported in figure 2.3. Radii ranging from 12 to 50 mm were measured. Since all the markers were attached on the skin surface, the radii of curvature experienced by the vertebral column, and even more by the spinal cord itself, are expected to be at least 1 to 2 mm smaller.

2.1.5 Subdural spinal cord implants

The implants considered in this study were designed for FES of rat spinal cord lumbar segment in the context of motor rehabilitation after spinal cord injury. The implants were inserted in the subdural space (below the dura mater) to allow better motor selectivity and intrathecal drug delivery. They featured 7 electrodes in a 3-1-3 configuration optimally placed to target the dorsal roots projecting to spinal segments that contain flexion and extension circuits. The intraspinal portion of these devices was 3.2 mm wide and 3 cm long. For this study we compared two different neural implant technologies: a soft and stretchable implant made from silicone elastomer, and a flexible but stiff implant made using a polyimide polymer. Details are given below:

Soft implants : Soft e-dura implants were prepared following the process developed by Ivan Minev detailed in appendix A.1. The implants consisted of a fully functional device, including both the micro-fluidic channel for intrathecal drug delivery and seven electrodes integrated in a transparent silicone (Sylgard 184, Dow corning) substrate with a thickness of 120 μm . A picture of the assembled soft implant is given in figure 2.4a.

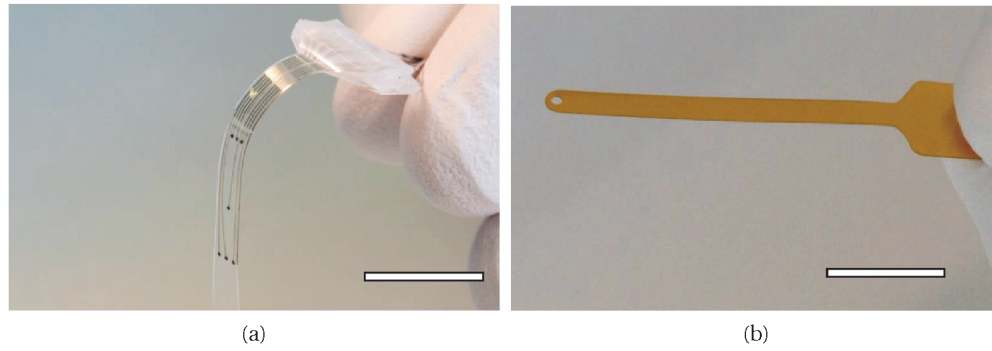


Figure 2.4 – Soft and stiff rat spinal cord implant

a - Soft silicone implant made from 120 μm thick functionalized PDMS stacks. **b** - Flexible implant made from 25 μm polyimide. Scale bars are 1.5 cm Adapted from [83].

Stiff implants: Stiff implants were prepared from 25 μm thick polyimide foil (Kapton™-100HN, DuPont). The contour of the implant was cut out using a laser micromachining tool (LAB 3550, Inno6 Inc.) and had rounded edges to minimize tissue trauma during insertion. Neither electrodes nor interconnects were patterned on the polyimide foil. A picture of the stiff implant is given in figure 2.4b.

The mechanical properties of both implants are presented in the table below and compared to the rat dura mater. The flexural rigidity of the implants were calculated considering the implant as a plate and using the following equation:

$$D = \frac{Eh^3}{12(1-\nu^2)} \quad (2.3)$$

where E is the Young's Modulus, h the thickness of the plate and ν the Poisson's Ratio.

	Dura mater	Soft implant	Stiff implant
Substrate	Collagen/elastin fibers	PDMS	Polyimide
Bulk young modulus (MPa)	≈ 1	2	2×10^3
Thickness (μm)	≈ 100	120	25
Flexural rigidity (Pa·m ³)	$\approx 1 \times 10^{-7}$	4×10^{-7}	5×10^{-6}
Tensile stiffness (N)	≈ 0.3	0.8	2×10^2

Table 2.2 – Implant mechanical properties

2.2 Mechanical evaluation in spinal cord surrogate model

In this section, the previously described implants are evaluated *in-vitro* in a surrogate model of the spinal cord.

2.2.1 Spinal cord surrogate model

We developed a mechanical surrogate model of the rat spinal cord. The model was composed of a surrogate dura made from silicone elastomer, enclosing a surrogate spinal tissue made from gelatin hydrogel. The soft or stiff implant were inserted in between the dura and spinal tissue surrogate before sealing the model. The model was kept in water to allow full expansion of the hydrogel and constant lubrication of the entire implant. A picture of the assembled surrogate model fitted with a stiff implant is shown in figure 2.5.

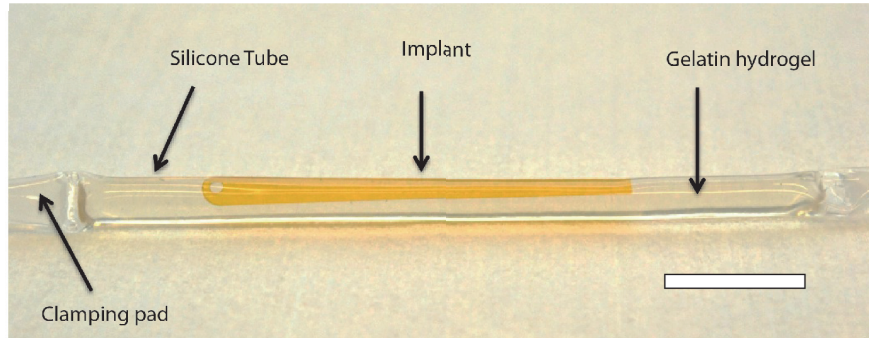


Figure 2.5 – Assembled spinal cord surrogate inserted with a stiff polyimide implant

The surrogate is composed of a silicone tube to mimic the dura mater enclosing a gelatin hydrogel rod mimicking the spinal tissue. The implant is inserted between the silicone tube and the gelatine rod before sealing. Scale bare is 1 cm. Detailed assembly process is given in appendix A.3. Adapted from [83].

Dura surrogate : The dura surrogate consisted of a PDMS silicone (Sylgard 184, Dow Corning) tube with a length of 8.5 cm, a diameter of 3.2 mm and a thickness ranging from 80 to 100 μm . The PDMS substrate (Young modulus of 2 MPa) tube dimensions were chosen to approximate the rat natural spinal dura mater (see section 2.1.4).

Spinal tissue surrogate : The spinal tissue surrogate consisted of a gelatin hydrogel rod (10% gelatin by weight in water, gelatin from bovine skin, Sigma-Aldrich) with a length of 8.5 cm and diameter of 3.2 mm. The gelatin hydrogel was chosen to approximate the spinal tissue. We measured the compressive modulus for 10% gelatin hydrogel by indentation and fitting of a Hertz contact model (details can be found in appendix A.2). We measured a compressive elastic modulus of 9.2 ± 0.66 kPa ($n=5$ test runs) which is comparable to measurements of indentation on rat lumbar spinal cord tissue from the litterature [90] [91].

Fabrication process : Details on the fabrication process of the surrogate model are given in appendix A.3.

2.2.2 Mechanical tests on spinal cord surrogate

Spinal cord surrogate model in relaxed state

Methods : We imaged the spinal cord surrogate models in a relaxed state with either a soft, stiff or no implant. We used micro-computed tomography (μ CT) to obtain a cross-section visualization of the models. The resolution of the scanner was limited to voxels of $37\mu\text{m}$ and did not allow direct visualization of the stiff implant. Details of the method can be found in appendix A.4.1.

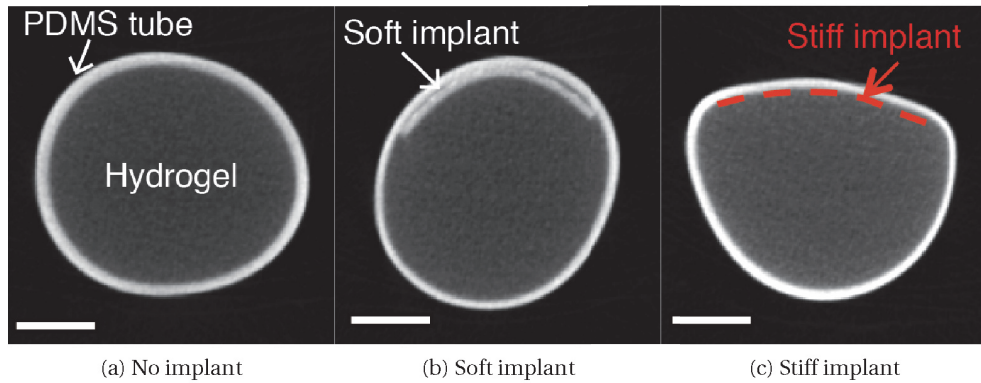


Figure 2.6 – Micro-computed tomography of spinal cord surrogate models at relaxed state

Spinal cord surrogate models at relaxed state with (a) no implant, (b) soft implant and (c) stiff implant. The scanner resolution ($37\mu\text{m}$) does not allow visualization of the stiff implant ($25\mu\text{m}$). The soft implant can conform to the curvature of the hydrogel while the stiff implant impedes the original circular shape of the model. Scale bars are 1 mm. Adapted from [83].

Results : Obtained cross sections can be seen in figure 2.6. The PDMS silicone appeared in light grey whereas the hydrogel made mostly of water appeared in darker grey. Without any implant the model had an expected circular shape. The presence of the soft implant did not impact the shape of the model. The soft implant conformed well to the circumferential curvature of the surrogate. In contrast, the stiff implant impedes the circular shape of the model but presented a slight circumferential curvature.

Bending test on Spinal cord surrogate

Methods : The model was flexed to controlled bending radii, which covered the entire range of physiologically relevant spinal movement determined in-vivo (figure 2.3). Parallel lines with 1mm inter-distance were drawn directly onto the surface of the implants to allow measurements of the deformations. In addition the models were imaged using μ CT scan for a specific radius of curvature of 27 mm.

Chapter 2. Soft substrate for long term biointegration of e-dura implant

Results : The soft implant conformed to the flexion of simulated spinal tissues. The strain along the sagittal crest of the model (broken line) was determined experimentally (discrete symbols) and compared to a geometrical prediction (continuous line). The stiff implant started wrinkling with radii smaller than 30mm. The amplitude of wrinkles, termed A, and the wavelength depended on the bending radius.

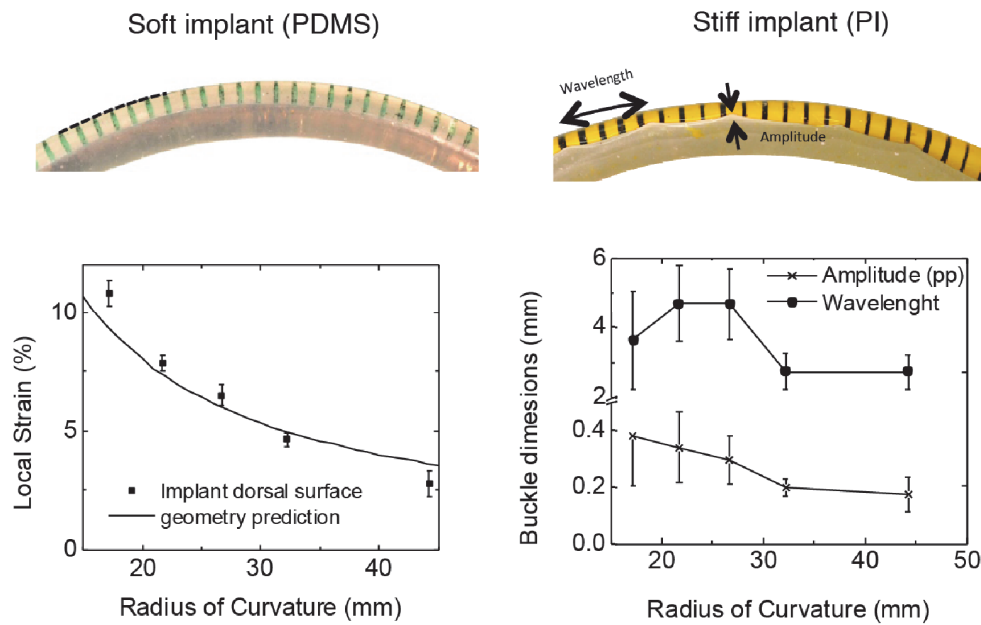


Figure 2.7 – Effect of bending deformations on spinal cord surrogate model

The soft implant (left panel) conformed to the flexion of the spinal cord surrogate model. The local strains along the dashed line were evaluated and compared to theoretical predictions. The stiff (right panel) implant could not conform to the non-developable topology of the bended model. The stiff implant started wrinkling with radii smaller than 50 mm. Amplitude and wavelength of the buckled structures are presented as a function of the radius of curvature in the main axis. Adapted from [83].

Tensile test on spinal cord surrogate

Methods : The spinal cord implant model was placed under uni-axial tensile stretch. Graphite powder particles were mixed with the hydrogel during gel preparation to create markers. Markers in the hydrogel ‘spinal tissue’ were then tracked and used to measure the local strain by image correlation.

Results : The graphs in figure 2.9 quantify locally induced strain in the implant and in the hydrogel core (spinal tissues) as a function of the global applied strain to the model. The soft implant was able to stretch with the model of spinal cord. In contrast, there was a substantial mismatch between the local strain inside the model and the induced deformation of the stiff implant. Consequently, the stiff implant slid between the silicone and the hydrogel during stretch.

2.3. Long term biointegration of subdural spinal implant in rat model

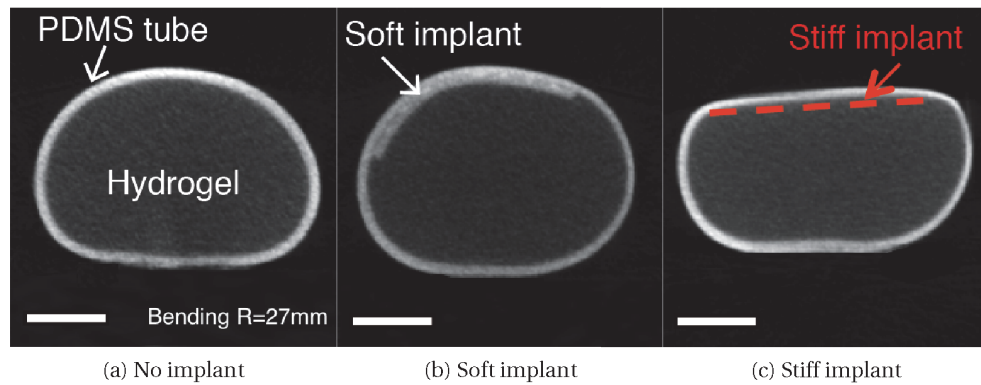


Figure 2.8 – Micro-computed tomography of spinal cord surrogate models conforming a radius of curvature of 27 mm

Spinal cord surrogate models with no implant (a), soft implant(b) and stiff implant(c) conforming to a round object with a radius of curvature of 27 mm. Scale bars are 1 mm. Adapted from [83].

2.3 Long term biointegration of subdural spinal implant in rat model

In this section, the long-term biointegration of the soft and stiff implants in a rat animal model is reported.

2.3.1 Animal groups and surgical implantation

All surgical procedures were performed in accordance with Swiss federal legislation and under the guidelines established at EPFL. Local Swiss Veterinary Offices approved all the procedures. Experiments were performed on Lewis rats (LEW/ORLj) with initial weight of 180-200 g.

Animal groups

We comparatively evaluated the long-term biointegration after 6 weeks of implantation for 3 groups of animals:

- A *soft implant group* (n=4), received a fully functional soft device including a silicone subdural implant, head connector, vertebral orthosis, and subdermal wires.
- A *stiff implant group* (n=4), received a stiff device including a polyimide subdural implant, head connector, vertebral orthosis, and subdermal wires.
- A *sham-operated group* (n=4), received the head connector, vertebral orthosis, and subdermal wires but no subdural implant.

Prior to surgery rats were handled and trained daily in the locomotor tasks for three weeks. These tasks included walking overground along a straight runway, and crossing a horizontal

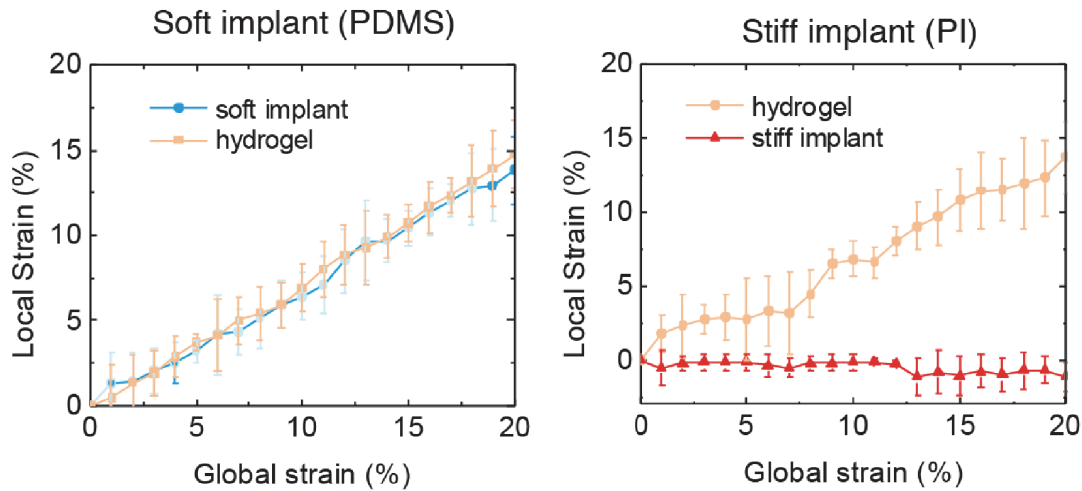


Figure 2.9 – Effect of uni-axial stretch on spinal cord surrogate model

Local strain in implant and hydrogel spinal tissue surrogate model. Mean \pm standard deviation (SD). Adapted from [83].

ladder with irregularly spaced rungs. Prior to the training, rats underwent a mild food deprivation and were rewarded with yogurt at the end of each trial. The body weight was monitored closely; in case of weight loss the food deprivation was adjusted. The animals were terminated 6 weeks post-implantation.

Surgical procedure

Soft and stiff implants were implanted under Isoflurane/Dorbene anesthesia. Under sterile conditions, a dorsal midline skin incision was made and the muscles covering the dorsal vertebral column were removed. A partial laminectomy was performed at vertebrae levels L3-L4 and T12-T13 to create entry and exit points for the implant. To access the intrathecal space, a 3 mm long mediolateral incision was performed in the dura mater at both laminectomy sites. A loop of surgical suture (Ethilon 4.0) was inserted through the rostral (T12-T13) dura mater incision and pushed horizontally along the subdural space until the loop emerged through the caudal (L3-L4) dura mater incision. The extremity of the implant was then folded around the suture loop. The loop was then retracted gently to position the implant over the spinal cord. A small portion of the implant protruded beyond the rostral dura mater incision and could be manipulated with fine forceps to adjust the mediolateral and rostrocaudal positioning of the implant. The protruded extremity of the implant became encapsulated within connective tissues, which secured positioning of the implant in the chronic stages.

The soft-to-wires (and microfluidic) connector were secured to the bone using a vertebral orthosis. The connector was first positioned above the vertebral bone. Four micro-screws (Precision Stainless Steel 303 Machine Screw, Binding Head, Slotted Drive, ANSI B18.6.3, # 000-120, 0.125) were inserted into the bone of rostral and caudal vertebrae. Surgical suture

2.3. Long term biointegration of subdural spinal implant in rat model

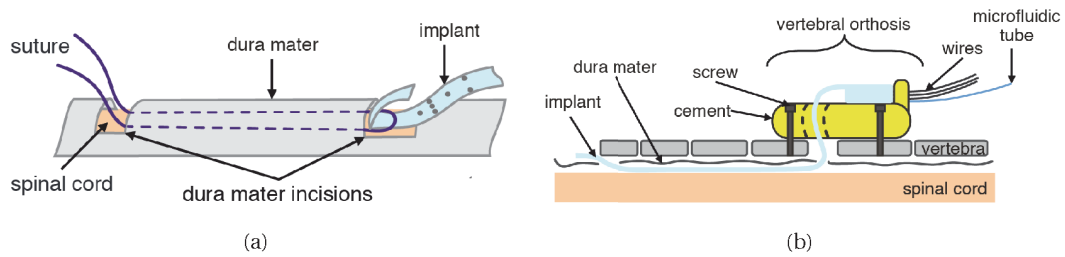


Figure 2.10 – Orthoses and surgical procedures for chronic e-dura implantation

a - Surgical procedure to slide the e-dura below the dura mater covering lumbar segments. **b** - Side view of the engineered vertebral orthosis that secures the e-dura connector, and ensures long-term functionality of embedded electrodes and chemotrode in vivo. Adapted from [83].

(Ethilon 4.0) was used to form a cage around the micro-screws and connector. The walls of the cage were plastered using freshly mixed dental cement (ProBase Cold, Ivoclar Vivadent) extruded through a syringe. After solidification of the dental cement, the electrical wires and microfluidic tube were routed sub-cutaneously to the head of the rat, where the Omnetics electrical connector and the microfluidic access port were secured to the skull using dental cement. The same method was used to create the vertebral orthosis for stiff and sham implants.

2.3.2 Biointegration evaluation

Kinematic evaluation

Methods : We assessed the motor performance of the different groups by recording high resolution body kinematics of the animals during a skilled locomotion across a horizontal ladder. The bilateral hindlimb kinematics were recorded using a Vicon imaging system featuring 12 infrared motion capture cameras (200 Hz; Vicon). Reflective markers were attached bilaterally overlying iliac crest, greater trochanter (hip), lateral condyle (knee), lateral malleolus (ankle), distal end of the fifth metatarsal (limb endpoint) and the toe (tip). Joints and body segments were then reconstructed with Nexus software. Representative kinematics are presented in figure 2.11a. We quantified the percentage of missed steps for each group during the performance of the ladder locomotion task. Results are reported in figure 2.11b.

Results : The sham operated rats did not show deficits when traversing the horizontal ladder over the duration of the study. The behavior of the rat with the soft e-dura implant was statistically similar to the rats with sham implant even at chronic stages. In contrast, the rats with the stiff polyimide implant displayed significant motor deficits that emerged around 1 to 2 weeks after implantation and deteriorated over time. They failed to accurately position their paws onto the rungs of the ladder. Even during basic walking, rats with stiff implants showed pronounced gait impairments, including altered foot control, reduced leg movement, and postural imbalance.

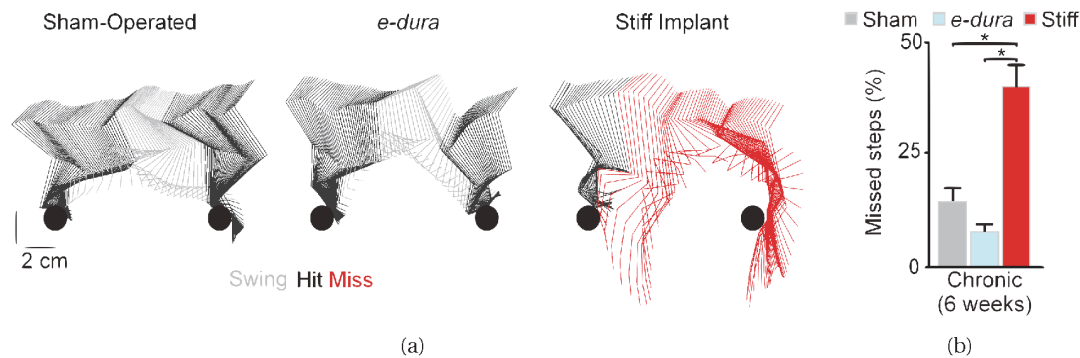


Figure 2.11 – Kinematic evaluation of biointegration

a - Representative hindlimb kinematics during ladder walking 6 weeks after implantation. **b** - Bar plots reporting mean percentage of missed steps averaged per animal onto the rungs of the ladder ($n = 8$ trials per rat, $n = 4$ rats per group). Adapted from [83].

Spinal cord morphology evaluation

Method : At the end of the 6 weeks experimental procedures, rats were perfused with Ringer's solution containing 100 000 IU/L heparin and 0.25% NaNO_2 followed by 4% phosphate buffered paraformaldehyde, pH 7.4 containing 5% sucrose. The spinal cords were dissected (figure 2.12a), post-fixed overnight, and transferred to 30% phosphate buffered sucrose for cryoprotection. After 4 days, the tissue was embedded and the entire lumbosacral tract sectioned in a cryostat at a $40\ \mu\text{m}$ thickness.

To assess spinal cord morphology, a Nissl staining was performed on 25 evenly spaced lumbosacral cross-sections separated by 0.8 mm, for each rat. The slides were assembled into the NeuroLucida image analysis software (MBF Bioscience, USA) to reconstruct lumbosacral segments in 3D. Spinal cord compression was quantified using a circularity index defined as $\frac{4\pi \text{area}}{\text{perimeter}^2}$. Circularity index was measured for all the slices, and averaged for each rat to obtain a mean value that was compared across groups.

Results : After the 6 weeks implantation period, both implants were still located in the targeted subdural space, with minimal connective tissue as shown in figure 2.12. The reconstruction of the spinal segments from the cross sections are depicted in figure 2.13. Both sham and soft implant groups presented similar circularity index while the group with stiff implants had significant deformation of the spinal segments at the vicinity of the implant and subsequently lower circularity index (figure 2.13c).

Neuro-inflammation evaluation

Method : Neuroinflammatory responses at chronic stages were visualized with antibodies against activated astrocytes (GFAP) and microglia/macrophage (Iba1), two standard cellular

2.3. Long term biointegration of subdural spinal implant in rat model

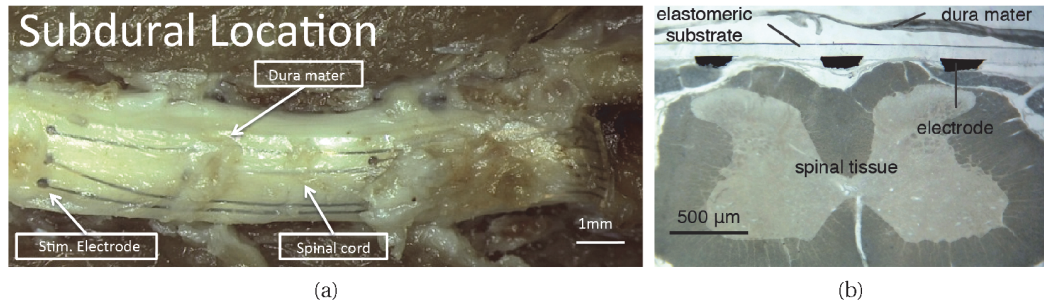


Figure 2.12 – Long term integration of soft e-dura implant

a - Optical image of a soft silicone e-dura implant after 6 weeks subdural implantation in a freely moving rat. The dura mater and spinal cord was exposed during post sacrifice dissection of the animal. **b** - Cross-section of a soft silicone e-dura inserted for 6 weeks in the spinal subdural space. The spinal tissue showed no visual sign of impairment. Adapted from [83].

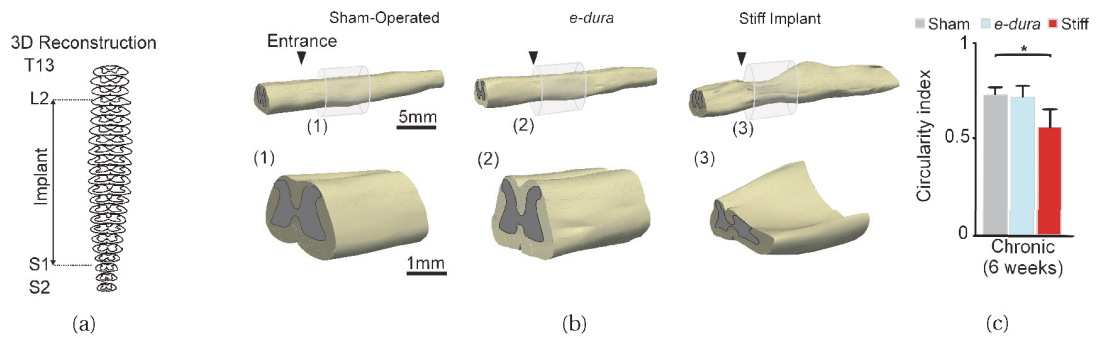


Figure 2.13 – Spinal cord morphology evaluation

a,b - 3D spinal cord reconstructions, including enhanced views, 6 weeks after implantation. The arrowheads indicate the entrance of the implant into the subdural space. **c** - Bar plots reporting mean values of spinal cord circularity index ($\frac{4\pi \text{ area}}{\text{perimeter}^2}$). Adapted from [83].

markers for foreign-body reaction. The detailed protocol is given in appendix A.5.1. Then, immunostaining density was measured offline using 6 representative confocal images of lumbosacral segments per rat. Images were acquired using standard imaging settings that were kept constant across rats. Images were analyzed using custom-written MATLAB scripts according to previously described methods [89]. Confocal output images were divided into square regions of interest (ROI), and densities computed within each ROI as the ratio of traced fibers (amount of pixels) per ROI area. Files were color-filtered and binarized by means of an intensity threshold. Threshold values were set empirically and maintained across sections, animals and groups. All the analyses were performed blindly.

Results: The sham and soft implant groups presented statistically similar inflammatory cell density. In contrast the group with stiff implants had a massive accumulation of both cell

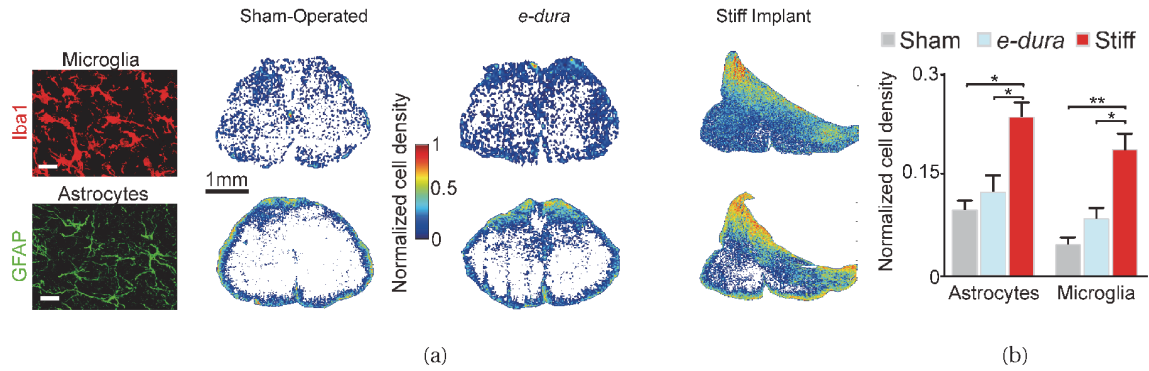


Figure 2.14 – Neuro-inflammation evaluation

a - Photographs and heat maps showing microglia (Iba1) and astrocytes (GFAP, glial fibrillary acidic protein) staining reflecting neuroinflammation. Scale bars: 30mm. **b** - Bar plots showing normalized astrocyte and microglia density. Adapted from [83].

types at the vicinity of the implants.

2.4 Discussion

The experiments presented in the previous sections demonstrated long term biocompatibility of soft implants while the stiff implants failed to accommodate mechanical deformations in the spinal cord surrogate model and created impairments in the implanted rats.

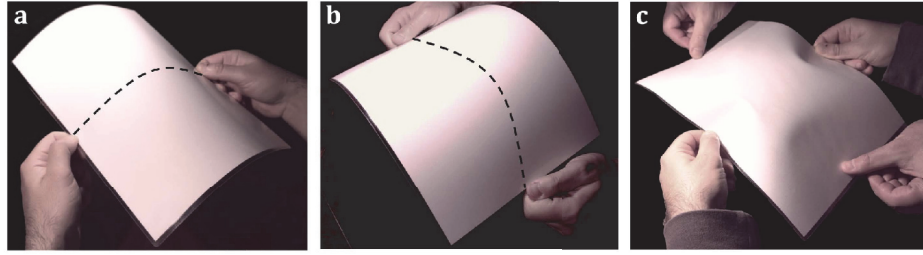
The stiff implant (25µm thick) presented a flexural rigidity one order of magnitude larger than the soft implant. During bending movements the stiff implant created significant more resistance than the soft implant which might have actively contributed to the failure of its biointegration. Reducing the thickness of polyimide implant to a few µm is technically possible. A 2.5µm implant made of polyimide would have a flexural rigidity less important than the studied soft implant while the tensile stiffness will be still two order of magnitude larger than soft implant. However simple consideration of flexural rigidity might not be relevant for implant conforming to complex dynamical shapes like the spinal cord. The influence of two dimensional bending on flexural rigidity of thin sheets is discussed below:

Curvature induced stiffening

Most organs have a complex non-developable surface. They present areas with a compound curvature. The spinal cord for example has a first curvature in the transverse plane and a second curvature in the coronal plane and can be assimilated to the section of a torus. These surfaces can not be geometrically flattened into a plane without creating distortions (stretching or compression). Inversely a flat 2D sheet with a thickness h and a length L can not be wrapped around such objects without being locally stretched or buckled. In-plane stresses

are necessarily developed when a sheet is subject to biaxial bending. These stresses give rise to out of plane deformations (wrinkling, bending, buckling) rather than in plane straining, as bending is energetically $\left(\sim \left(\frac{h}{L}\right)^3\right)$ more favorable than in-plane straining $\left(\sim \frac{h}{L}\right)$ [92–94].

We observed this effect during the bending of the spinal cord surrogate model loaded with the stiff implant (2.2.2) but a simple demonstration can be done with a sheet of paper as shown by Pini et al [95] (figure 2.15). The piece of paper was able to bend in both transversal and longitudinal directions however a biaxial bending created buckling of the structure.

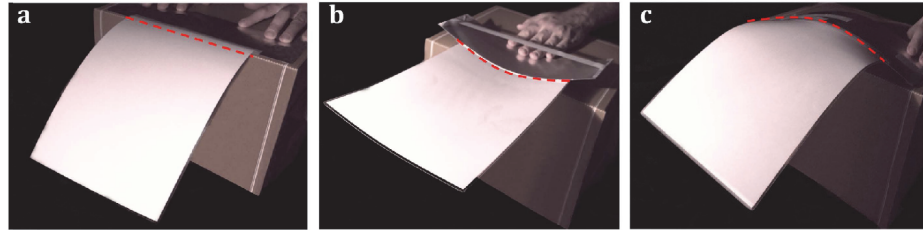


Adapted from Pini et al. [95].

Figure 2.15 – Wrinkling of a paper sheet subject to biaxial bending

Photographs of a A4 paper sheet manually subject to uniaxial bending in the transversal (a) and longitudinal (b) directions; and to biaxial bending (c).

Inversely, Pini et al. showed that *“the stiffness of cantilever sheets significantly increases with transversal curvature”*. For example adding a slight curvature to a piece of paper enabled to reduce the deflection due to the gravity as seen in figure 2.16.



Adapted from Pini et al. [95].

Figure 2.16 – Stiffening of sheet of paper by transversal bending

a -The piece of paper had no transversal curvature and bended under gravity influence (b) positive and (c) negative curvature allowed to reduce deflection due to gravity.

Pini et al. expressed the relative change of stiffness due to static curvature for a plate with a thickness h , a length L and a width b :

$$\frac{\Delta k}{k} = \frac{L^2}{60 \eta^2} \beta^4 (\kappa_y - \nu \kappa_x)^2 \quad (2.4)$$

Chapter 2. Soft substrate for long term biointegration of e-dura implant

where $\beta = \frac{b}{L}$, $\eta = \frac{h}{L}$, ν the poisson ratio and κ_y and κ_x the static curvature of the plate. For a given curvature the change of stiffness scales like $\sim \frac{1}{\eta^2}$. Thus the thinner the film ($\eta \ll 1$), the more pronounced is the curvature stiffening effect.

For our specific study case the following observations can be made :

- The theory discussed applies for both elastomeric soft implant and stiff plastic implant. However a soft material enables to achieve equivalent bending stiffness with comparatively thicker sheet. The relative curvature stiffening is thus less important for a sheet of soft material compared to a sheet of stiff material with equivalent bending stiffness.
- In an *in-vivo* case, the implant is constrained by the surrounding tissue. The surrounding tissue will oppose forces to counterbalance out-of-plane deformations of the implant. These forces will contribute to the energetic cost of the deformation. In plane-straining might then become more energetically favorable than out of the plane deformations. An implant with a smaller tensile stiffness will be more prone to stretch in plane while an implant with higher tensile modulus will be able to oppose more force to the surrounding tissue while deforming out of plane.

An alternative to decrease the tensile stiffness of the substrate while avoiding the use of elastomers consist in patterning extremely thin films into web-like systems [71, 96, 97]. The patterned substrate enables to obtain a certain degree of stretchability by allowing elements to deform out of plane following the same principal as a curly telephone cable. For example, fractal-like meshes develop into out-of-plane structures during mechanical loading, which facilitates reversible and local compliance. Medical devices prepared with such three-dimensional (3D) topologies can conform to the curvilinear surface of the heart [97] and skin. However, this type of interface requires complex, multistep processing and transient packaging. In comparison, the fabrication steps of soft silicone e-dura are remarkably simple. Moreover, the shape and unusual resilience of the soft implant greatly facilitate surgical procedures.

2.5 Conclusion

In this chapter, the comparative mechanical and biocompatibility analysis of standard stiff neural technologies to soft silicone neural implants were presented around a specific case study of spinal cord FES in the rat animal model. First, the mechanical and dynamical properties of rat dura mater was evaluated. We used these results to guide the design of a soft silicone implant able to match the mechanical properties of the natural rat dura mater. Both soft and stiff implant where mechanically evaluated in a surrogate model of the spinal cord. The stiff implant failed to accommodate the complex bidirectional curvature of the spinal cord which resulted in buckling and large out of plane deformations. On the contrary the soft silicone implant was able to stretch and accommodate bidirectional curvature. We then

evaluated the biointegration of both implant in-vivo over a 6 week period. The soft neural implants showed long-term biointegration while the stiff implant failed to integrate and impaired the animal. These results showed that biomechanical coupling between implants and neural tissues is critical to achieve neural biointegration. In conclusion neural implants prepared with elastic materials met the demanding static and dynamic mechanical properties of spinal and triggered limited foreign-body reaction even when implanted in the subdural space. In the following chapter we will use this soft neural technology to realize functional devices for long-term neural recordings and functional stimulation.

2.6 Contribution

Data presented in this chapter are the result of a team effort :

- I contributed to the fabrication of the implants. I led, designed, performed and analyzed experiments related to the spinal cord surrogate. I participated to the design and analysis of animal experiments and assisted the surgeries.
- Ivan Minev designed the soft e-dura implant and developed original fabrication process and led the design, realization and analysis of the various experiments.
- Surgeries, tissue analysis, and animal experimental work were performed by the team of Grégoire Courtine's laboratory including Pavel Musienko, Quentin Barraud, Nikolaus Wenger among others.

3 Electrical stimulation and biopotential recording e-dura implants using micro-cracked gold technology

In the previous chapter we saw that reducing the mechanical mismatch between implants and targeted tissue led to better biointegration of e-dura implants. In particular PDMS silicone elastomer proved to be an excellent substrate to mimic natural dura mater. However implementing electronics on such stretchable elastomeric substrate is a challenging task. In this chapter I report the use of micro-cracked stretchable gold metalization on silicone substrate to realize functional chronic implant for recording and stimulation of the surface of the CNS. After a brief introduction on the technology, I will present my personal contribution to the fabrication process of e-dura implant. Next, *in-vitro* and *in-vivo* functional validation of ECoG and spinal FES e-dura implants for mouse, rat and pig animal models will be reported.

This chapter is adapted from the following publications:

- [83] MINEV*, Ivan R., MUSIENKO*, Pavel, HIRSCH, Arthur, et al. Electronic dura mater for long-term multimodal neural interfaces *Science*, 2015, vol. 347, n° 6218, p. 159-163.
- [98] HIRSCH, Arthur., MINEV, Ivan R., PAVLOVA, Natalia., ASBOTH, Leonie., COURTIME, Grégoire., LACOUR, Stéphanie P. Pdms based μ -ecog. *in proceedings MEA Meeting 2014*, 2014, pp. 237–238.

3.1 Introduction

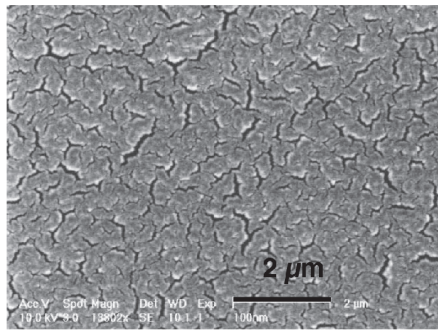
3.1.1 Motivation

Context

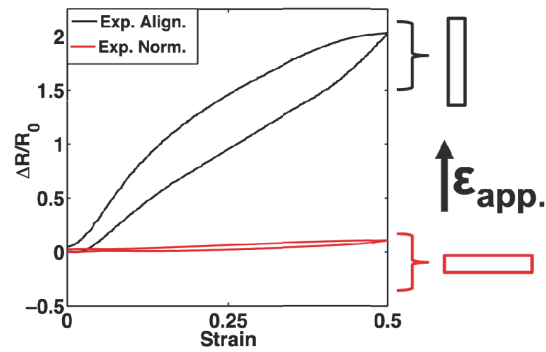
Micro-cracked gold thin film is particularly promising for bio-electronic applications. This process developed by Lacour et al. [82], consist of physical vapor deposition (thermal evaporation) of gold on a PDMS silicone substrate to create a 25 to 60 nm thin film. During the

Chapter 3. Electrical stimulation and biopotential recording e-dura implants using micro-cracked gold technology

deposition micro-cracks ($\sim 1 \mu\text{m}$ in length) spontaneously form within the thin film while maintaining a conductive percolating path, as depicted in figure 3.1a. These micro-cracks act as strain relief by deflecting out-of-plane when the film is strained, thus avoiding the formation of catastrophic macro cracks. The film is characterized by a sheet resistance ranging from 10 to $100 \Omega/\square$ depending on the thickness deposited. The resistance of the film is sensitive to the direction and magnitude of applied strain as characterized by Michaud et al. [99] and depicted in figure 3.1b. The film exhibits a gauge factor ~ 4 when strained in the direction of the electrical current, yet is little affected by strain in the normal direction.



(a) Adapted from Lacour et al. [82].



(b) Adapted from Michaud et al. [99].

Figure 3.1 – Stretchable micro-cracked gold thin film

a - SEM image of 25 nm thin micro-cracked Au film deposited on PDMS substrate. **b** - Relative change in resistance of a strain gauge made of a 5×0.5 mm micro-cracked gold track on PDMS substrate when applying aligned and normal strain. Initial resistance R_0 is 138Ω for the aligned (black) gauge and 131Ω for the normal (red) gauge.

E-dura implants for recording and stimulation can be fabricated on PDMS substrate using micro-cracked gold interconnects. Gold interconnects are patterned using a stencil mask and encapsulated with a layer of silicone leaving electrode sites exposed. Further coating of the electrode with a platinum-elastomer mesocomposite enables to enhance the electrochemical properties of the electrodes as shown by Minev et al. [47]. A representative standard process flow is detailed in appendix A.1.

Problem Statement

While acute proof-of-principle *in-vivo* recordings [100] and stimulations [101] of neural tissues were previously obtained using this technology, the long-term *in-vivo* stability and functionality of such implants remained undocumented. Body dynamics and foreign body reactions create a harsh environment for the implant that might limit its integrity and function over time.

Moreover, the former fabrication process suffered from several pitfalls that limited the fabrication yield and integration density. An application like ECoG requires high density and number

of electrodes. Refinement of the fabrication process was thus necessary to enable translation of the process towards clinical applications.

3.1.2 Goal and specific aims

Goal

The overall goal of this chapter was to evaluate long-term recording and stimulation functionality of soft e-dura implant based on micro-cracked gold metalization.

Specific aims

The specific aim of the project are listed below :

- Provide refinement in the fabrication process, to allow better fabrication yield and electrode density.
- Validate *in-vitro*, long-term mechanical and functional stability of the implants.
- Validate *in-vivo*, long-term mechanical and functional stability of the implants.

3.2 Technological development

In this section, our contribution to the fabrication process of e-dura implant is detailed.

3.2.1 Process limitations

The process established by Minev et al. (appendix A.1) was originally developed to produce soft e-dura implant for proof-of-concept studies only requiring implant with limited surface and number of electrodes (< 8). This process involved a limited number of steps and proved to be effective to build series of 10 to 20 soft implants. However it still relied on several manual steps limiting the yield of production, the critical achievable dimensions and the ability to scale to larger area. These aspects needed to be addressed in order to produce soft implants with extended number of electrodes and integration density and reliability. This new development will contribute to the translation of soft e-dura technologies towards clinical human applications.

Several pitfalls in the former process were identified :

Encapsulation layer : This step relied on the fabrication of a complex stack of 3 PDMS layers and release monolayers followed by the selective transfer of two of these PDMS layers. This step was particularly time consuming and had a low yield (< 50%).

Chapter 3. Electrical stimulation and biopotential recording e-dura implants using micro-cracked gold technology

Patterning of electrode sites : The electrode sites were formed by manual mechanical punching holes through the encapsulation layer prior to its bonding on the carrier layer. Manual punching is time consuming and requires a certain skill of the manipulator while the possible shape and size of the electrodes are limited by the puncturing tool.

Final wiring of the device : Wires used to be manually positioned above the terminal pad of the gold film interconnects. A conductive polymer deposited by hand beforehand on the pads enabled the electrical contact. The assembly was then finally secured by flooding a silicone adhesive to form a package. These steps required a particularly skilled operator and limited the integration density on the wire/pad connector.

3.2.2 Proposed solutions

The proposed solutions are detailed below :

Encapsulation layer : We used sheets of PDMS silicone stacked between two polymers films (PET ~ 50µm, polyimide 25µm) for the fabrication of the encapsulation layer. They were obtained by lamination of polyimide on commercially available silicone sheet (elastosil™, Wacker). The polyimide layer was used as a screen during the screen printing process while the PET layer was removed before plasma bonding. Both layers avoided accumulation of dust and were removed before bonding or after screen printing.

Patterning of electrode sites and connectors pads : The manual hole punching was replaced by laser ablation to form electrodes and contacts within the encapsulation layer. A femto second laser (WS Turret-200, Optec) was used to cut through the encapsulation layer stack. The polyimide and PET films avoided the re-deposition of debris on the PDMS layer. The laser enabled processing of A4 sheets which were cut in a parallel to form many encapsulation layers, reducing significantly production time and increasing yield. The encapsulation layer was then plasma bonded to the carrier substrate and electrodes and contact pads were then screen printed through the polyimide layer before removing the latter.

Final wiring of the device : Direct wiring onto the pads was replaced by an intermediate surface-mount connector (SMD). Connection wires were fitted to a 16 contacts SMD connector (800µm pitch, Tiger Beam™, Samtec). Each assembled connector could be individually electrically tested before final mounting on the device. The assembled connector was then mounted on a 3 axis micro-manipulator, aligned to contact pads and press fitted on matching pads on the wafer. The assembly was then finally secured by flooding a silicone adhesive to form a package.

A representative process flow is given below :

Results : The detailed process was used to fabricate soft e-dura ECoGs for recordings in pig. Pictures from different steps of the assembly process can be seen in figure 3.3. The process

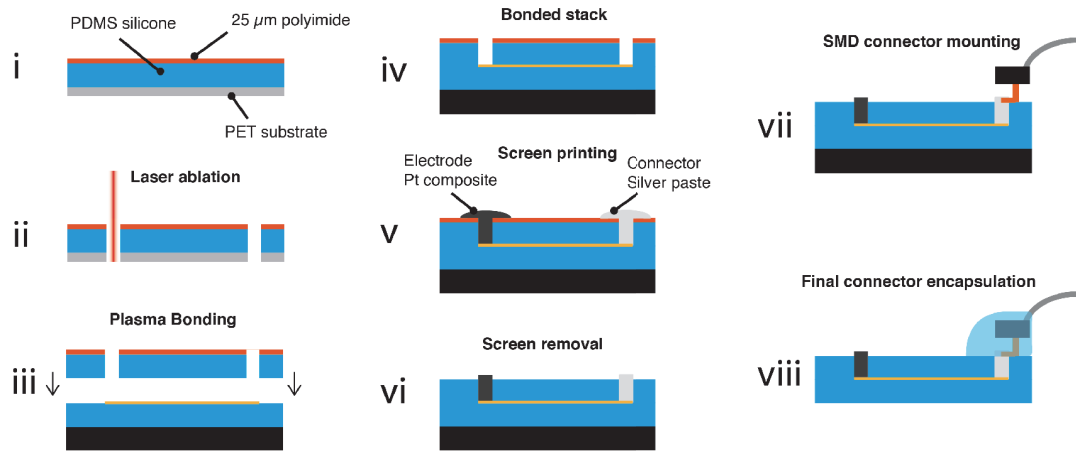


Figure 3.2 – Second generation process flow for soft e-dura implant assembly

i - Encapsulation layer composed of a stack PET thin film, PDMS silicone and polyimide thin film. **ii** - Electrodes sites and connectors pads were formed by laser ablation of the stack. **iii** - **iv** - After removing of PET thin film the encapsulation stack was aligned and plasma bonded to metalized PDMS layer. **v** - Screen printing of electrode sites with Pt composite and connector pad with conductive silver paste. **vi** - Removing the screening polyimide layer enabled to form electrodes and pads. **vii** - Surface mounted connector (SMD) was aligned and put in contact with connector pads. **viii** - Final encapsulation of connector with room temperature vulcanized (RTV) silicone.

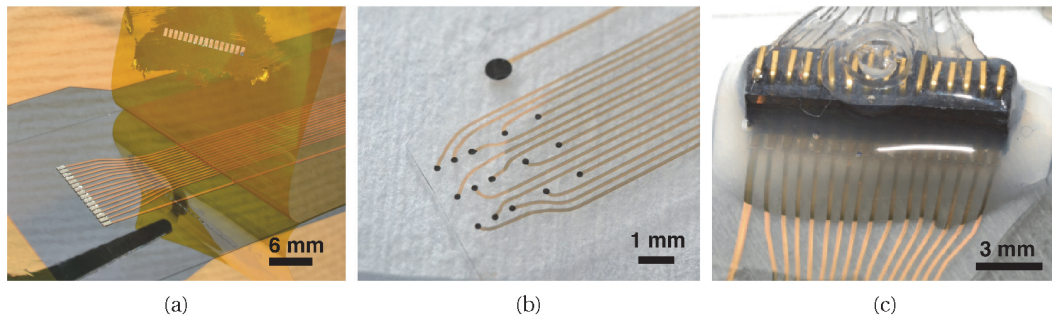


Figure 3.3 – Pictures from the assembly of a soft e-dura ECoG

a - Removing of polyimide screen layer during screen printing of conductive paste on connectors pads. **b** - Screen printed Pt composite electrodes. Laser process enables various shapes and electrode sizes. **c** - Details on surface mounted connector with 16 pads and 800 μm pitch.

improvements enabled to reduce the fabrication time from 8 to 4 days per device batch and increased the fabrication yield from ~ 50% to ~ 80%.

3.3 Functional electrical stimulation validation

In this section, the long term stimulation functionality of e-dura implants is evaluated using functional electrical stimulation (FES) e-dura implant designed to fit the rat spinal cord as described in the previous chapter 2.1.3. First, the stability of the implant to repeated mechanical deformation is evaluated *in-vitro*, then, the long-term implantation and functional use of the implant is reported.

3.3.1 Rodent e-dura FES implant

Functional specifications : The implant was designed to be implanted in the subdural space of the spinal cord in rat and deliver both chemical and electrical stimuli for motor rehabilitation after spinal cord injury. The implant featured 7 stimulation electrodes designed to selectively address dorsal root ganglion and a micro-channel for direct delivery of serotonin agonists ($5HT_{1A/7}$ and $5HT_2$). A picture of the implant and integrated chemotrode is given in figure 3.4.

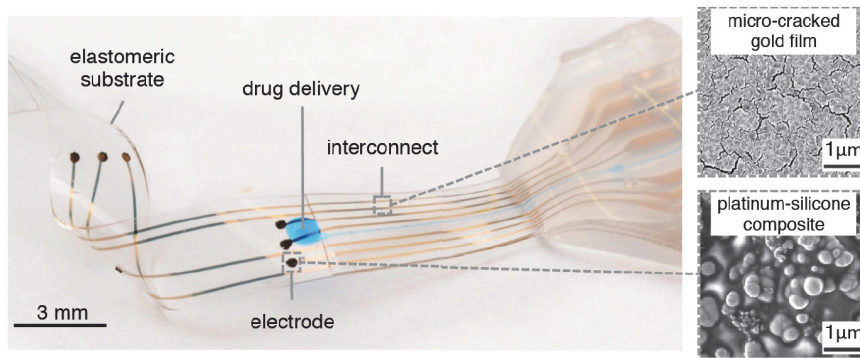


Figure 3.4 – e-dura implant for spinal FES in rat

Optical image of an implant, and scanning electron micrographs of the gold film and the platinum-silicone composite. A blue dye was used to highlight the micro-channel. Adapted from [83].

Design specifications : The subdural part of the implant was 3.2 mm wide and 3 cm long with a thickness of 120 μm . The electrical interconnects consisted of 35 nm thick stretchable micro-cracked gold film. The silicone substrate integrated a 100 μm by 50 μm in cross section micro-channel fabricated by soft-lithography. The electrodes were approximately 300 μm in diameter and covered by Pt-PDMS composite.

3.3.2 *In-vitro* validation

To demonstrate the robustness of the soft implant against deformation experienced by natural dura mater during daily living activities, we evaluated the impact of repeated mechanical deformations on the implant *in-vitro* using a customized experimental set-up combining

3.3. Functional electrical stimulation validation

electrochemical impedance spectroscopy with cyclic mechanical loading.

Experimental set-up

Uni-axial stretcher : The tested implant sample was secured in a customized uni-axial stretcher and immersed in saline solution to conduct electrochemical characterization of the electrodes following different stretching protocols. The stretcher was controlled with a custom Labview program and programmed to hold the implant under test at a specific strain or to execute a preset number of stretch relaxation cycles.

Impedance spectroscopy : Electrochemical impedance spectroscopy measurements were conducted in phosphate buffered saline (PBS, pH 7.4, Gibco) at room temperature using a three-electrode setup and a potentiostat equipped with a frequency response analyzer (Reference 600, Gamry Instruments). A 5 cm long Pt wire served as counter electrode and a Standard Calomel Electrode (SCE) as reference. Impedance spectra were taken at the open circuit potential. The excitation voltage amplitude was 7 mV.

Figure 3.5a shows an implant mounted on the uni-axial stretcher and immersed in saline solution. The attachment rods are connected to the clamps of the stretcher and follow horizontal linear motion. A counter and a reference electrode were submerged in the electrolyte to complete the circuit but are not visible on the picture.

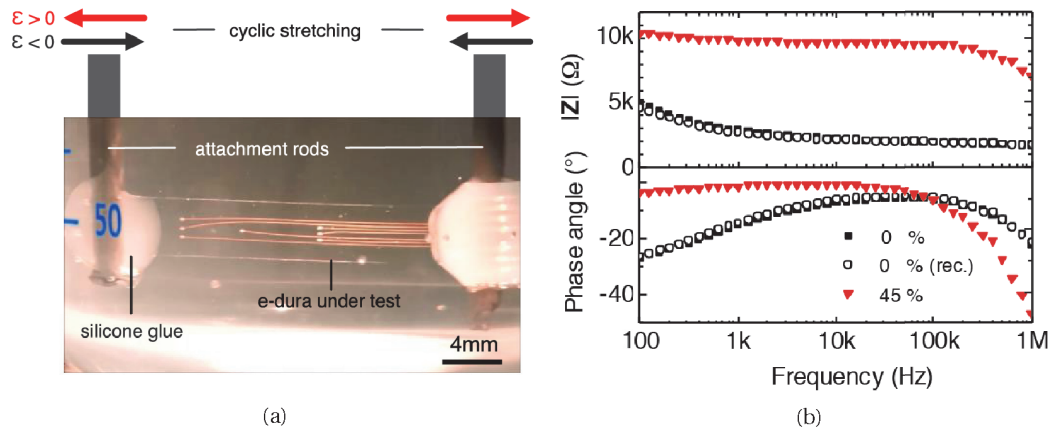


Figure 3.5 – In-vitro validation of stimulation e-dura implant

a - Apparatus for conducting electrochemical characterization of soft implants under tensile strain. The ends of the implant were glued to two probes that are clamped to the jaws of a custom built extensimeter. The implant and (partially) the probes were then submerged in Phosphate Buffered Saline solution (PBS). The extensimeter applied pre-defined static strain to the implant, or performed a cyclic stretch-relax program. A counter and a reference electrode were submerged in the electrolyte to complete the circuit (not shown) **b** - Magnitude and phase of electrode impedance recorded in saline solution (pH 7.4). Spectra were collected before (■), at maximum elongation (▼), and after (○) a uniaxial stretch cycle to 45% strain. Adapted from [83].

Experimental results

Influence of uni-axial deformation on electrode impedance : We measured the electrode impedance at 45% applied strain and at relaxed state before and after applying the mechanical deformation. A representative impedance spectrum is depicted in figure 3.5b. The composite electrodes of the soft implant displayed low impedance ($Z = 5.2 \pm 0.8 \text{ k}\Omega$ at 1 kHz, $n = 28$ electrodes) that remained stable even after stretching to 45%. Impedance modulus in stretched state revealed base line increase to 10 k Ω that can be attributed to the strain gauge behavior of the interconnects.

Evolution of impedance to repeated mechanical deformation : We evaluated the robustness of the implant by subjecting it to one million stretching cycles at 20% while immersed in saline solution. One cycle was performed every second and the experiment span over two weeks. Impedance spectra were measured every 10^n cycles. Results are presented in figure 3.6. The impedance remained relatively stable up to 100k cycles and raised a relative change of 2 in averaged after one 1M cycles.

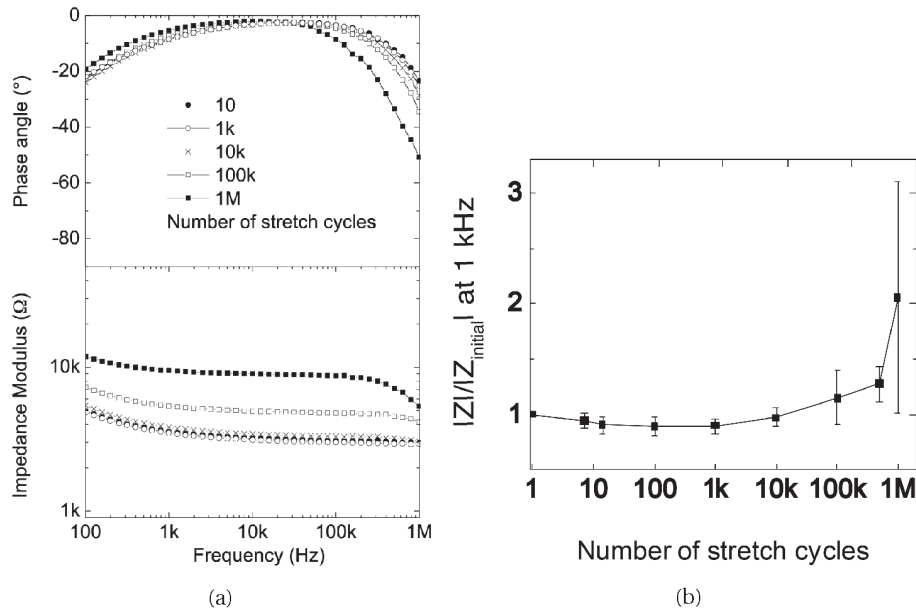


Figure 3.6 – Impedance spectroscopy of the soft electrodes under cyclic stretching to 20% strain.

a - Representative impedance plots recorded from one electrode. The spectra were recorded at 0% applied strain after 10, 1,000, 10,000, 100,000 and 1 million stretch cycles. Each stretch cycle lasted 1s. The implants remained immersed in PBS throughout the evaluations. The remaining 6 electrodes in the tested implants exhibited a similar behavior. **b** - Relative impedance modulus of electrodes ($n = 7$, mean \pm SD) at 1 kHz and at rest and after uniaxial fatigue cycling to 20% strain. Adapted from [83].

3.3.3 *In-vivo* validation

In this section we evaluated the long-term in-vivo stability and functionality of stimulation e-dura implants in rats over a 5 week-period.

Animal groups

- The change of electrode impedance in-vivo was evaluated in the *soft implant animal group* (n=4) used for the biocompatibility study, described in section 2.3.1.
- Functionality of e-dura FES implant was evaluated in a independant group (n=3). Rats were first implanted with an e-dura over lumbosacral segments with additional bipolar electrodes into ankle muscles to record electromyographic (EMG) activity. After 10 days of recovery from surgery, they received a spinal cord injury. E-dura surgical procedure was already reported in section 2.3.1 additional details on EMG, spinal cord injury procedure and rehabilitation are given in appendix A.6.

Evolution of impedance *in-vivo*

Method : The impedance of e-dura electrodes implanted over lumbosacral segments was recorded using a bipolar electrode configuration (working and counter electrode only). The counter electrode was a ‘Cooner’ wire with a deinsulated tip implanted in the osseous body of vertebra L1. As with in vitro measurements, impedance spectra were obtained with a potentiostat equipped with a frequency response analyzer (Reference 600, Gamry Instruments) using the same settings. Weekly electrochemical impedance spectroscopy measurements of all electrodes were made in fully awake rats held by an experienced handler.

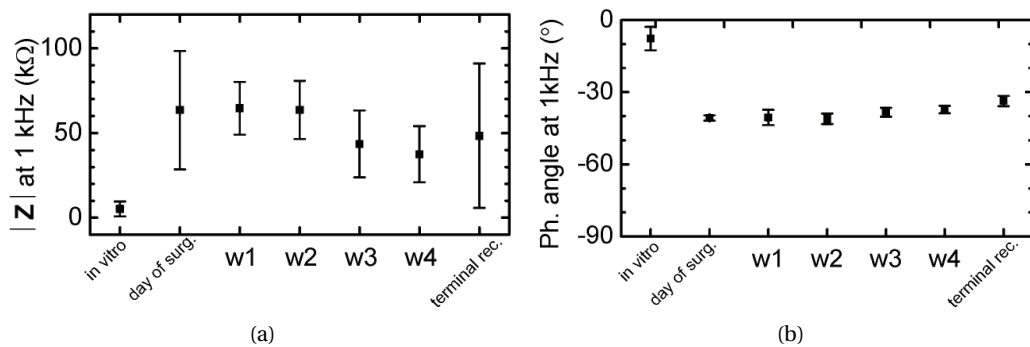


Figure 3.7 – Evolution of electrodes impedance *in-vivo*

Modulus (a) and phase (b) at 1 kHz (n = 28 total electrodes, mean ± SD, across four rats) recorded *in-vitro*, then *in-vivo* immediately after implantation and weekly until terminal procedure. Adapted from [83].

Chapter 3. Electrical stimulation and biopotential recording e-dura implants using micro-cracked gold technology

Result : Impedance at 1 kHz remained constant through-out the 5 weeks of implantation, demonstrating stability of stretchable electrodes *in-vivo*.

FES of the spinal cord

We demonstrated the chronic stimulation capability of e-dura implant by restoring locomotion with FES in a rat model of spinal cord injury [89].

Method : Each adult rat received a clinically relevant contusion at the thoracic level, which spared less than 10% of spinal tissues at the lesion epicenter and led to permanent paralysis of both legs as seen in figure 3.8a. After a 7 days recovery period, each rat was trained daily for 30 min. The e-dura implant was used to elicit gait patterns by stimulating spinal locomotor circuits located below injury in combination with a serotonergic replacement therapy (5HT_{1A/7} and 5HT₂ agonists) [20] injected intratechally via the integrated chemotrode. Continuous electrical stimulation was delivered on the lateral aspect of L2 and S1 segments (40 Hz—, 0.2 ms, 50 to 150 μ A) [18]. The neurorehabilitation experiments were performed on a treadmill using a robotic body weight compensation system (Robomedica)(see figure 3.8b).

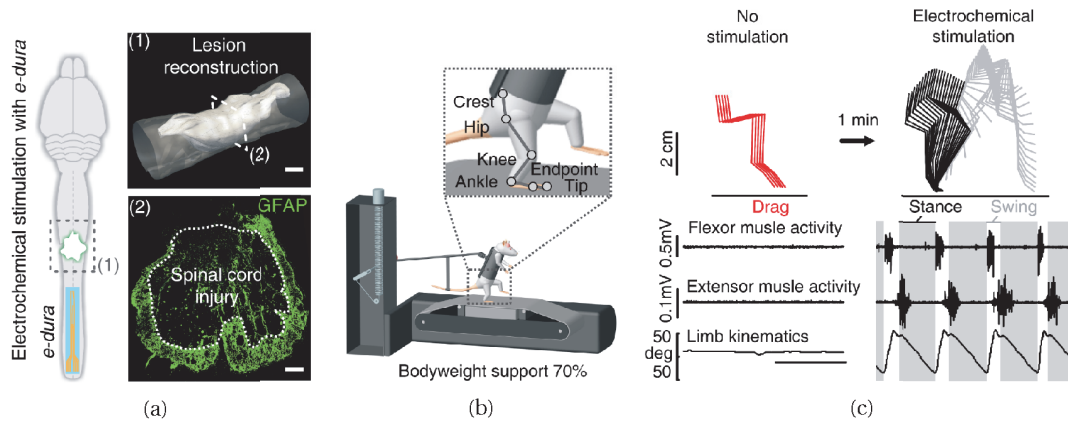


Figure 3.8 – FES for spinal cord rehabilitation

a - Spinal cord contusion **b** - Treadmill and robotic body weight compensation system for neurorehabilitation therapy. **c** - Recording without and with electrochemical stimulation during bipedal locomotion under robotic support after 3 weeks of rehabilitation. Stick diagram decompositions of hindlimb movements are shown together with leg muscle activity and hindlimb oscillations. Adapted from [83].

Result : The combination of electrical and chemical stimulations enabled the paralysed rats to retrieve walking gait patterns whereas controlled experiments left rat's hindlimbs paralysed. The implant electrodes and chemotrode maintained functionality during the duration of the experiments allowing specific electrical stimulation and direct intrathecal drug delivery.

These combined results demonstrated the mechanical robustness and long-term functionality of the soft e-dura electrodes and integrated chemotrodes.

3.4 Biopotentials recording validation

In this section, the long term biopotential recording functionality of e-dura implants is reported. Micro-ECoG implants were designed to record from rodent and mini-pig cortex. First, light-evoked potentials in mouse expressing Channelrhodopsin-2 ubiquitously were recorded, then cortical states are extracted from chronic recordings in freely behaving rats. Eventually, somatosensory evoked potentials obtained with clinical ECoG grid and e-dura micro-ECoG in mini-pig animal model are compared.

3.4.1 Micro-ECoG implants

Rodent micro-ECoG specifications : The rodent micro-ECoG was designed to cover a 2.25 mm^2 recording area and featured 8 recording and 1 reference electrodes. The electrodes were layed out in a 3 by 3 matrix with a nominal pitch of $750 \mu\text{m}$, supposed to be an optimal inter-electrode spacing for BMI application as suggested by Slutzky et al. [45]. Each electrode had a diameter of $150 \mu\text{m}$ and the PDMS substrate had a thickness of $120 \mu\text{m}$. A picture of the ECoG is shown in figure 3.9a.

Pig micro-ECoG specifications : The mini-pig micro-ECoG was designed to cover a 24 mm^2 recording area and featured 15 recording electrodes a reference electrode. The electrodes were layed out in a 5 by 3 matrix with a nominal pitch of 1 or 2 mm. Each electrode had a diameter of $300 \mu\text{m}$ while the reference electrode had a diameter of 1.5 mm. The PDMS substrate had a thickness of $120 \mu\text{m}$. A picture of the pig micro-ECoG is shown in figure 3.11c.

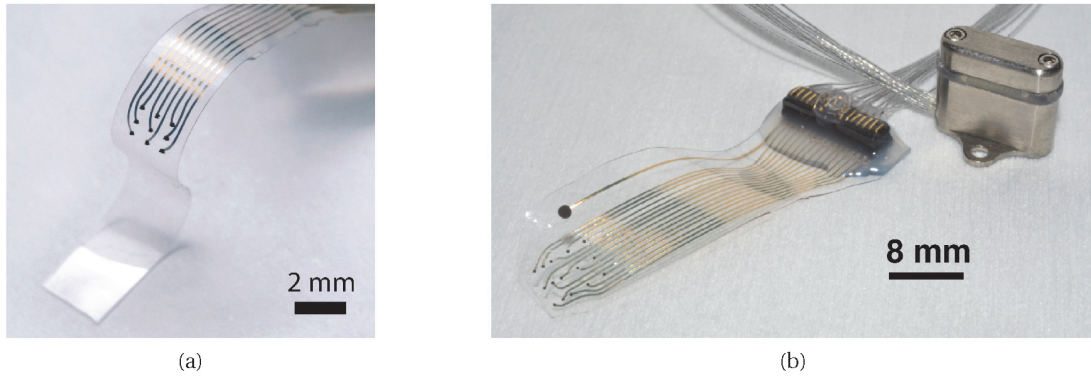


Figure 3.9 – e-dura micro-ECoG implants

a - Micro-ECoG designed for rodent. Adapted from [98]. **b** - Micro-ECoG designed for mini-pig.

Chapter 3. Electrical stimulation and biopotential recording e-dura implants using micro-cracked gold technology

3.4.2 *In-vivo* validation in rodent

Acute recording in mouse

In this section, the ability of e-dura micro-ECoG to record light evoked potentials with spacial selectivity on mouse expressing Channelrhodopsin-2 is demonstrated.

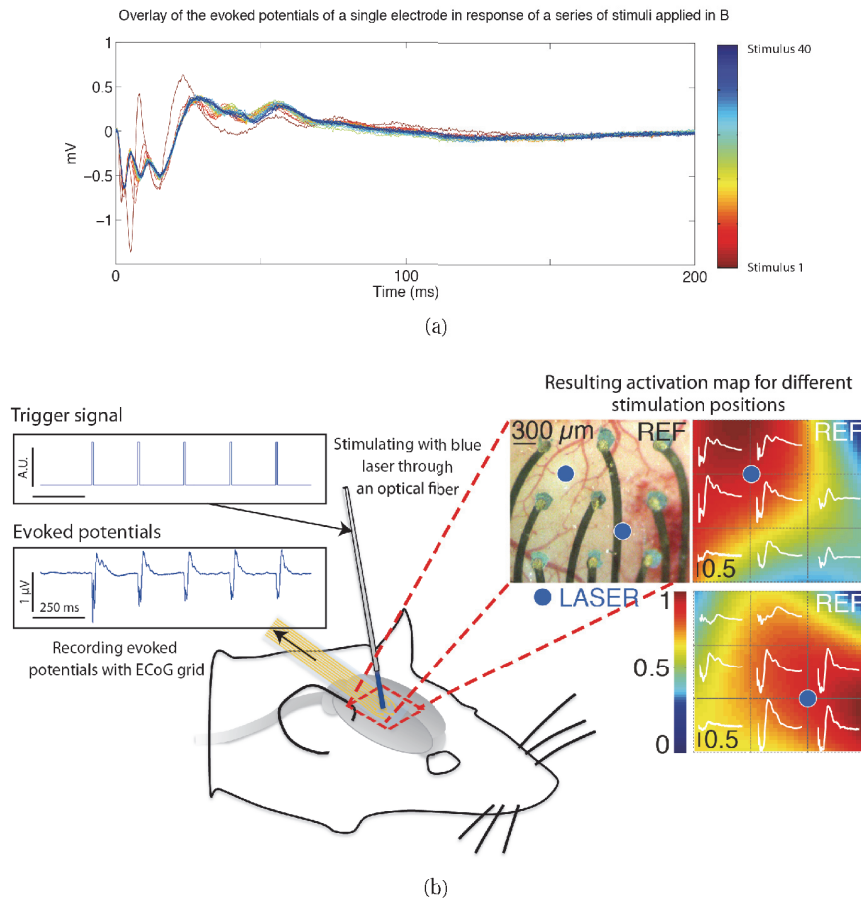


Figure 3.10 – Micro-ECoG recordings of light evoked potentials on mouse expressing Channelrhodopsin-2.

a - Overlay of raw evoked potentials of a single micro-ECoG electrode in response of a series of photo stimuli applied in the same location. **b** - Schematic of the experimental setup and recorded evoked potentials activation maps as a function of the position of the light stimuli (blue dot) . Adapted from [98].

Method : A mouse expressing Channelrhodopsin-2 (Thy1::ChR2) mice was anesthetized with Ketamine/Xylasine to preserve brain activity. The animal head was fixed in a stereotaxic frame (David Kopf Instruments) and a $2 \times 2 \text{ mm}^2$ craniotomy was performed over the leg area of the motor cortex, which was verified by the induction of leg movements in response to optogenetic stimulation. The e-dura micro-ECoG was placed over the exposed motor cortex

and covered with physiological saline. We employed a diode-pumped solid state blue laser (473 nm, Laserglow technologies) coupled via a FC/PC terminal connected to a 200 μm core optical fiber (ThorLabs) to deliver optical stimulation. Using a micro-manipulator, the fiber was placed at the center of each square formed by 4 adjacent electrodes.

Optical stimulation was delivered through the transparent elastomeric substrate to illuminate the surface of the motor cortex. A train of light pulses was delivered at 4 Hz, 9 ms duration, 30 mW intensity for each site of stimulation. Resulting potentials and trigger signals were acquired using a TDT neurophysiology workstation (Tucker Davies Technologies Inc.) and sampled at 24.414 kHz. For each electrode, the amplitude of light-induced electrocorticograms was extracted and normalized to the maximum recorded amplitude for that electrode, and the peak to peak amplitude calculated.

Results : Recorded signals displayed low background noise of 60 μV peak-to-peak, and negative potentials of up to 2 mV were evoked. Spatially defined potentials could be observed with multiple negative and positive potential peaks in accordance with the literature [102]. Figure 3.11a displays an overlay of evoked potentials recorded by one electrode in response to light stimulation (150 mW/mm², 472 nm, 9 ms pulse). The values measured across all the electrodes were used to generate color-coded neuronal activation maps that were specific for each site of stimulation as shown in figure 3.11b.

Chronic recording in freely behaving rat

In this section, the capability of e-dura micro-ECoG to record cortical state in freely behaving rat is demonstrated. Recording of electrocorticograms were obtained in a group of rats ($n = 3$) that were implanted with an e-dura over the leg area of the motor cortex, and with bipolar electrodes into ankle muscles of both legs. Electrocorticograms were measured in conjunction with whole body kinematics and muscle activity recordings during standing and walking in freely behaving rats. These rats followed the same behavioral training as rats in the biocompatibility group described in section 2.3.1.

Surgical procedure : The subdural implantation of micro-ECoG over the cortex was performed with a similar approach than the one developed for spinal implants. The implant was sled below the dura after performing two craniotomy and was mechanically secured in a cortical orthosis as shown in figure 3.11. The detailed surgical procedure is given in appendix A.6.4.

Method : The rats were tested every week for 3 weeks after chronic subdural implantation of micro-ECoG over the hindlimb area of the motor cortex. A lateral active site integrated in micro-ECoG was used as a reference for differential amplification. Differential recordings

Chapter 3. Electrical stimulation and biopotential recording e-dura implants using micro-cracked gold technology

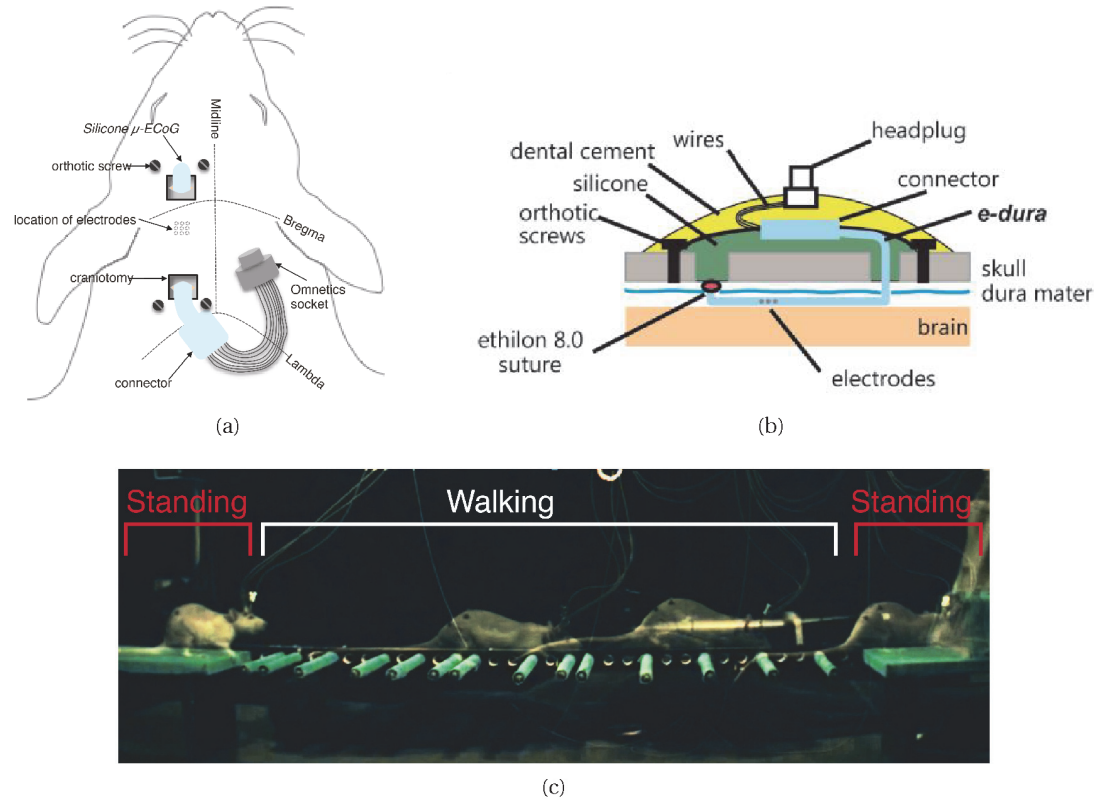


Figure 3.11 – Chronic ECoG surgical procedure

a - Surgical procedure to slide the e-dura below the dura mater covering the motor cortex. **b** - Side view describing the engineered cortical orthosis that secures the e-dura and its connector, ensuring chronic recordings of electrocorticograms in freely moving rats. **c** - Overlay images of rat performing a motor task above a horizontal ladder. Adapted from [83].

were obtained using a TDT RZ2 system (Tucker Davis Technologies), amplified with a PZ2 Pre-amplifier, sampled at 24.414 kHz, and digital band-passed filtered (0.1 - 5000 Hz). Kinematic and muscle activity recordings were used to dissociate standing and walking states.

Raw electrocorticograms were elaborated using previously described methods [103] depicted in figure 3.12. Briefly, each electrocorticogram was Fourier transformed into time resolved power spectral densities (trPSD), shown in units of standard deviation (std). Each trPSD was then normalized to mean trPSD in each frequency in order to account for drop in power with increasing frequencies. To calculate the time-resolved power of electrocorticograms within each contiguous band, we integrated the electrode-averaged trPSD across that band. We then compared all time-resolved power measurements during walking periods against all time-resolved power measurements during standing periods for each band using Wilcoxon rank-sum test. The low (LFB) and high (HFB) frequency bands (shared areas) were identified as bands with the local minima of p values.

3.4. Biopotentials recording validation

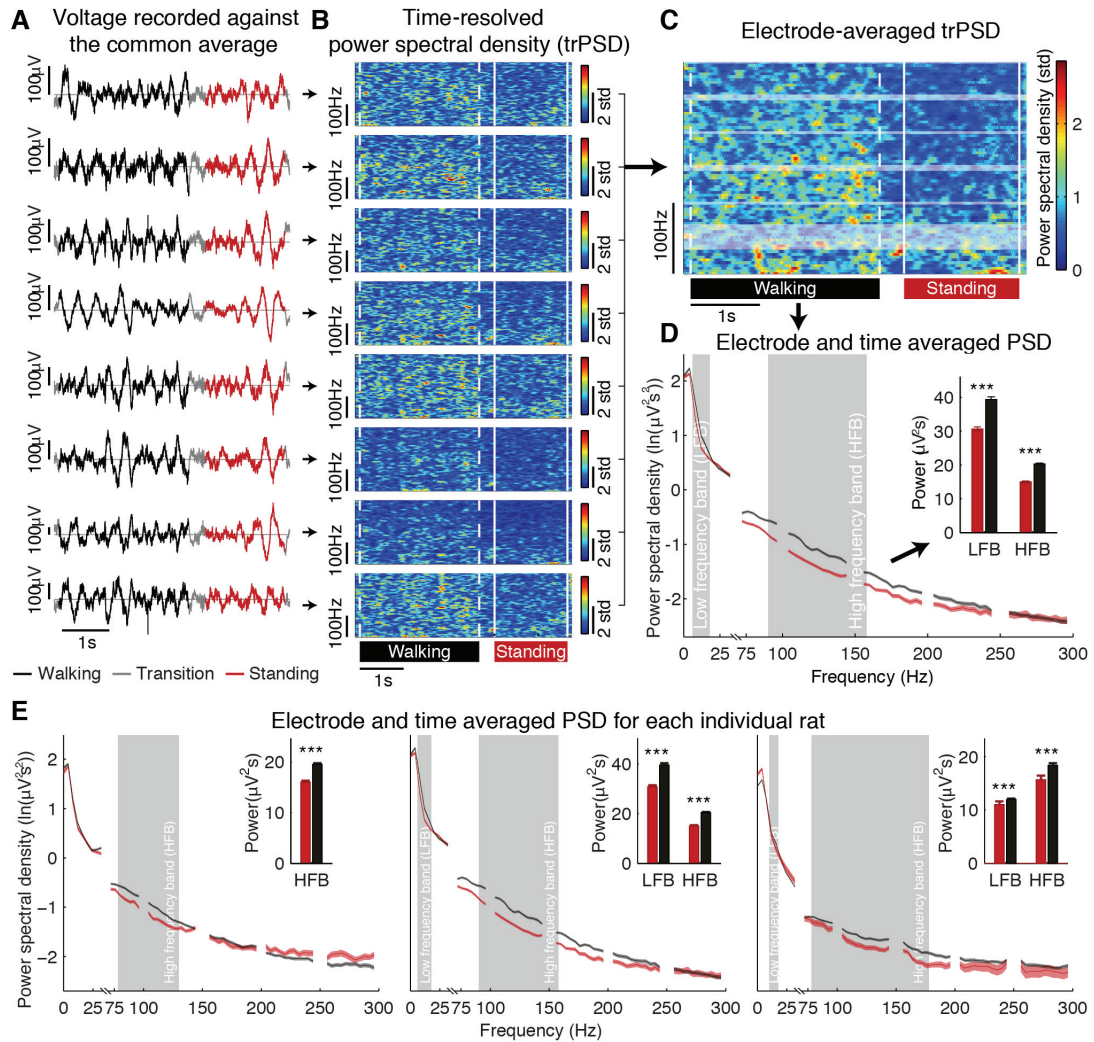


Figure 3.12 – Analysis of recorded micro-ECoG signals during unconstrained walking compared to standing rats

A - Voltage recorded against the common average on each electrode **B** - Time resolved power spectral density (trPSD) estimates on each electrode. **C** - Electrode averaged trPSD **D** - Electrode and time average PSD **E** Electrode and time average PSD for each individual rat. Adapted from [83].

Results: Power spectral density analysis applied on electrocorticograms clearly identified standing and locomotor states. Elevated power in low and high frequency bands during walking compared to standing is consistent with electrocorticogram recordings during hand movements in humans [103].

3.4.3 *In-vivo* validation in Pig

Translation of soft e-dura technology to non-human primates and patients requires first testing in a large animal species such as mini pig. In this section we reported accurate recordings of sensory-evoked potentials with standard clinical ECoG grid (2×4 subdural electrodes, AD-TECH) and micro-ECoG e-dura on pig. The Ad-tech consisted in a 2×4 grid of 2.3 mm diameter electrodes spaced by 10 mm. The goal of these experiments was to demonstrate the functionality of the e-dura technology for neural recordings in large animal models and compare them with standard clinical devices.

Surgical procedure : A 22 kg pig was kept under deep anesthesia (induced with propofol, ketamine xylazine). A mid-line sagittal skin incision was performed and a retractor placed. The site of the craniotomy was exposed (4×4 cm), the most posterior point of the craniotomy was located midline 1.5 cm behind the coronal suture, and the most anterior point was 2.5 cm in front of the coronal suture. With this exposure we avoided the large frontal sinuses and exposed correctly the sensori-motor cortex representing the snout. The dura mater was opened in a U shape with the pedicle in the midline. According to the visual observation of the gyri and sulci, ECoGs were placed on the sensory motor cortex.

Method : Ambu[®] neuroline subdermal electrodes were inserted in the snout to evoked potentials by subdermal electrical stimulation of the snout (charge balanced bipolar pulses, 1 mA, 100 ms, 1.1 Hz) and differential recordings were obtained using a TDT RZ2 system (Tucker Davis Technologies), amplified with a PZ2 Pre-amplifier, sampled at 25 kHz, and digital band-passed filtered (0.1 - 5000 Hz). The snout somatosensory region was localized by recording evoked potentials with the clinical macro-ECoG grid, the grid was then replaced by an e-dura micro-ECoG grid (see figure 3.13). Evoked potentials were then recorded for two different stimulation positions on the snout (see figure 3.15a).

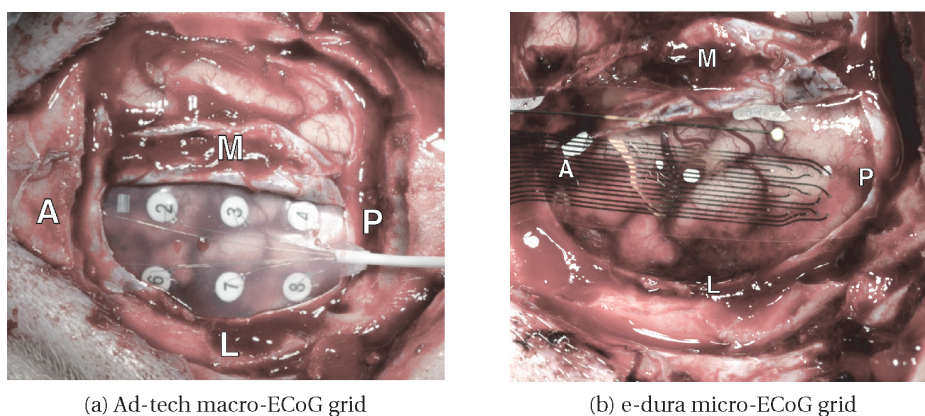
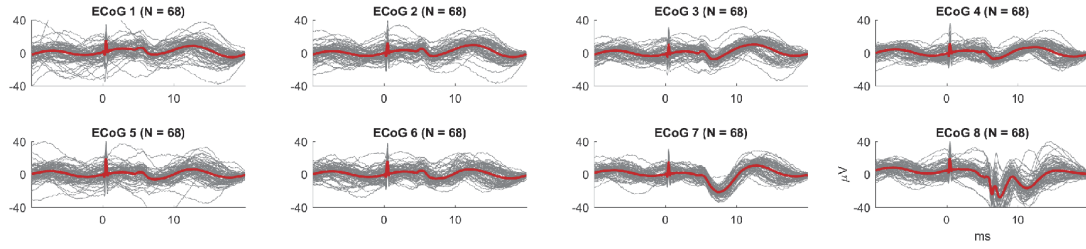


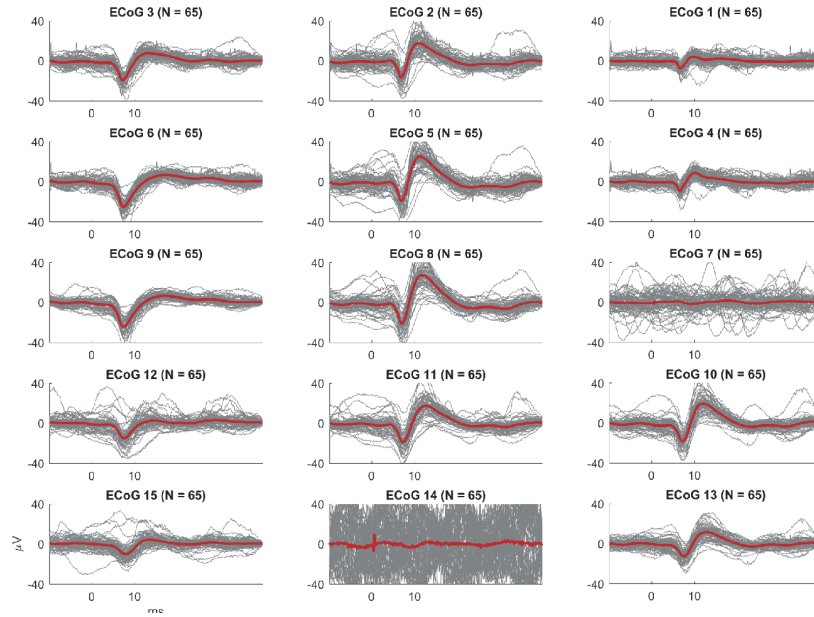
Figure 3.13 – Picture of ECoG grids on pig cortex

Results : Evoked potentials recorded with clinical macro-ECoG and e-dura micro-ECoG are

3.4. Biopotentials recording validation



(a) Evoked potentials recorded with clinical macro-ECoG grid



(b) Evoked potentials recorded with e-dura micro-ECoG grid

Figure 3.14 – Comparison between electrocorticograms recorded with clinical grid (a) and e-dura micro-ECoG (b)

compared in figure 3.14. The macro-ECoG could locate the somatosensory region on the cortex however significant evoked potential could only be recorded on one electrode. The size of the electrodes and pitch of the macro-ECoG grid prevented any site specific recording. Comparatively the e-dura micro-ECoG enabled to record potentials with spatial selectivity. Changing the stimulation position on the snout resulted in different activation maps as depicted in figure 3.15.

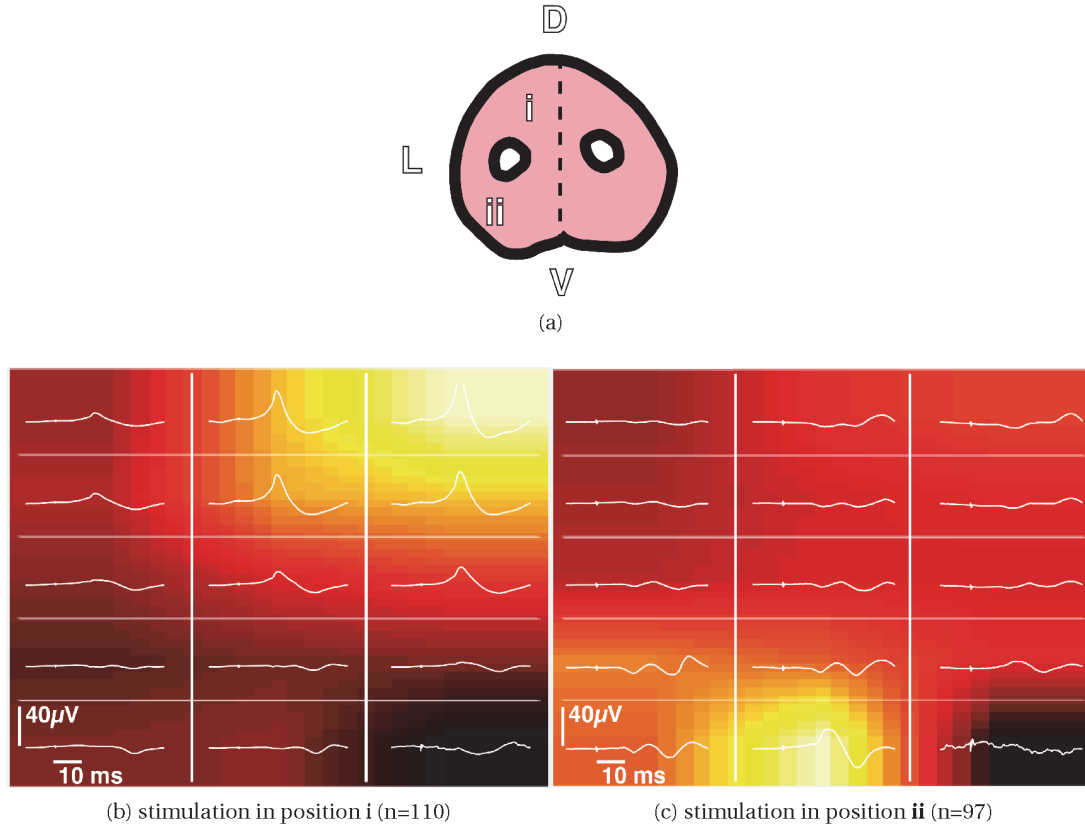


Figure 3.15 – Evoked cortical activation maps after snout electrical stimulation
a - Schematic frontal view of the pig snout and sites of stimulation (**i**, **ii**). **b** & **c** - Cortical activation maps reconstructed from normalized averaged electrocorticograms, shown in white.

3.5 Discussion

In the previous sections we presented soft silicone e-dura implants made from micro-cracked gold interconnects and platinum/silicone composite electrodes. We designed implants to deliver functional electrical stimulation to the spinal cord or record biopotentials on the surface of the cortex. We demonstrated the long-term functionality of these devices *in-vitro* and *in-vivo* in relevant animal models. However the micro-cracked gold metalization also has limitations that are discussed below:

Electrical resistance of micro-cracked gold : The stretchable micro-cracked structure of the metalization is the result of very specific deposition conditions. In particular, we only observed their formation in films thinner than 100 nm [104]. Thicker films gradually lose their stretchability and lead to macro cracks and electrical failure of the conductor. Consequently stretchable micro-cracked gold metalization produce thin and rather resistive films with sheet resistance ranging from 10 to 100 Ω/\square . For a interconnect of width W and length L , the

resistance of the interconnect tract is given by the following formula:

$$R = R_{\square} \times \frac{L}{W} \quad (3.1)$$

where R_{\square} is the sheet resistance of the conductive film and $\frac{L}{W}$ the aspect ratio of the conductive track. However, electrical interconnects for medical applications often have high aspect ratio. Resulting interconnects made of stretchable micro-cracked gold have thus a non-negligible resistance. For example a 200 μm wide and 10 cm long interconnect made of stretchable micro-cracked gold would have a resistance of at least 5 k Ω . While this has a limited impact for applications requiring limited transfer of charges like biopotentials recordings, it is more problematic when significant electrical currents are required. In particular powering a LED or delivering several mA electrical pulses would require significant voltage and trigger important joule losses. Consequently it is technically not possible at the moment to integrate active electronic components with micro-cracked gold interconnects.

Interconnects patterning and density : Certain applications like ECoGs for BMI require a high number and density of electrodes. However addressing a high number of electrodes with micro-cracked gold interconnects can be challenging. Indeed the micro-cracked gold metalization is a planar process. The deposition process enables to pattern conductive interconnects only in a single plane preventing crossing of electronically independent interconnects. This generates very challenging wire routing problems specially when addressing matrix of electrodes. A solution consists in using several metalized layers stacked onto each other and interconnected by electrical vias. While bonding and metalizing several layers is a simple task providing reliable vias with micro-cracked gold on different layers remainsto be achieved. Moreover if patterning the interconnects using photolithography is possible [105], it involves resists and chemicals that are hardly compatible with implants. Stencil masks are usually preferred but can be delicate to fabricate and manipulate for high density and aspect ratio features. Eventually size of the micro-cracks ($\sim 1\text{-}10\text{ }\mu\text{m}$) limits the practical minimal width of interconnects to 100 μm .

Soft to hard interface : When a mechanically heterogeneous assembly is deformed stresses concentrate at the interface between soft and stiff components [106]. As a result it is quite delicate to interface micro-cracked gold interconnects with stiff components such as wire or surface mounted devices. Local strain in the gold interconnects near the soft to hard interface may exceed the maximal strain allowed and cause failure of the track. We used conductive paste made of silver particles as a mechanical buffer to interface gold interconnects with wires and stiff connectors. Alternatives to silver should be found for translation to human applications.

3.6 Conclusion

In this chapter we demonstrated the fabrication and functionality of soft silicone e-dura implants made with micro-cracked gold interconnects and platinum/silicone composite electrodes. We first demonstrated the electro-chemical stability, mechanical robustness, and long-term functionality of these devices through *in-vitro* experiments. Implants were subjected to repeated mechanical deformations and aging in saline solutions and maintained functionality over several weeks. Soft implants were used in long-term *in-vivo* experiments to restore walk in rat model of spinal cord injury and to record cortical state in freely behaving animals. We also provided first acute somato-sensory cortical recording in pig. In conclusion neural implants prepared with elastic materials and soft micro-cracked interconnects met the demanding static and dynamic mechanical properties of spinal and brain tissues and maintained functionality over extended periods of time. However translation of soft e-dura technology to non-human primates and patients will require further testing in large animal species. Eventually implants with higher electrode density and embedded electronics to read and write into the nervous system in real time will require additional technological developments. In the following chapter we will explore the use of gallium to provide highly conductive interconnects and enable integration of active electronic components.

3.7 Contribution

Data presented in this chapter are the result of a team effort :

- I participated to the fabrication of e-dura FES implant and to their *in-vitro* and *in-vivo* characterization. I designed and fabricated ECoG e-dura implants and led their *in-vitro* and *in-vivo* characterization and validation.
- Ivan Minev designed the FES e-dura implant and participated and led their fabrication and their *in-vitro* and *in-vivo* characterization.
- Surgeries and animal experimental work were performed by the team of Grégoire Courtine's laboratory including Pavel Musienko, Quentin Barraud, Nikolaus Wenger among others.
- Fabien Wagner, Tomislav Milekovic and Léonie Asboth provided analysis of recorded biopotential data.

4 Gallium thin film for high performance interconnects

Some neuroprosthetics application requires devices with embedded active electronic components like LED optrodes or bio-potentials multiplexer chips. However, integration of tissue-matched implants with power demanding active electronical components requires the development of highly conductive and robust stretchable interconnects. In this chapter, I explore the use of gallium liquid metal to create highly conductive and stretchable interconnects. A new method to deposit and pattern thin films of liquid gallium using physical vapor deposition is introduced. I characterize the growth and electro-mechanical performance of the obtained films and demonstrate multilayer integration of active components in stretchable assemblies. Next, the silicone substrates are optimized to produce tailored thin films of gallium by micro-structuring the surface of silicone PDMS and taking advantage of wetting phenomena. Eventually I report and discuss challenges and opportunities of this technology to create e-dura implants with embedded active electronics.

This chapter is adapted from the following publications :

- [107] HIRSCH*, Arthur, MICHAUD*, Hadrien O., GERRATT, Aaron P., DE MULATIER, Séverine., LACOUR, Stéphanie P. Intrinsically stretchable biphasic (solid–liquid) thin metal films. *Advanced Materials*, 2016, vol. 28, no 22, p. 4507-4512.
- [108] HIRSCH, Arthur, LACOUR, Stéphanie P. Gallium super-lyophilic silicone for smooth tailored liquid metal stretchable thin films. *under preparation*, 2017.

4.1 Introduction

4.1.1 Motivation

Context

Traditionally, active electronic components in implantable medical devices are confined in a single hermetic casing. For example, implantable pulse generators (IPGs) used to provide electrical stimuli for deep brain stimulation electrodes are encased in a hermetic titanium box that prevent adverse interaction between electronic components and surrounding biological medium. However, recent developments in neuroprosthetics have created a demand for implantable devices integrating distributed active electronic components at the vicinity of nervous tissue. For instance, academic research is investigating the use of light emitting diodes (LEDs) to provide localized light delivery capability for optogenetics applications without relying on external light sources and optical fibers connectors [59, 109, 110] and integration of transistors near electrodes enables high throughput bio-potentials recordings [111, 112]. Nonetheless, significant challenges lie ahead for the integration of these active components in soft tissue-matched implants. These active components need to be protected from biological environments with a proper miniaturized water tight packaging. Although this aspect is out of the scope of this thesis, promising approaches are being developed to solve this problem [113–115]. Moreover, these active components require to be powered by significant levels of electrical currents. However, manufacturing elastic wiring networks to distribute and carry electrical potentials and currents in soft circuits is a persistent challenge, as micrometer-scale structuring over large areas, high electrical conductivity, robustness, long-term stability, and reliable mechanical performance are rarely concurrent [116]. Liquid metals are particularly interesting for the design of stretchable interconnects as they can rearrange and maintain high electrical conductivity when deformed. In this chapter, the use of gallium liquid metal is explored to enable integration of active electronics components in soft assemblies.

Gallium properties

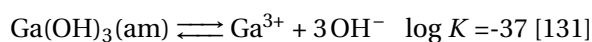
Gallium is a unique metallic liquid. With a melting point of 30°C and the ability to supercool [117, 118], it can be handled in the liquid state at room temperature. Unlike mercury, it has a near zero vapor pressure and low toxicity [119], making it safe to manipulate. Gallium and some gallium based alloys have recently gathered a significant interest from the scientific community as they offer a unique set of properties for the design of soft, stretchable and reconfigurable electronics [120]. Gallium is a good electrical conductor with a resistivity of 270 nΩ m at 20 °C. Enclosing gallium-based liquid metal in a soft elastomer enables the creation of highly deformable assemblies with unmatched combination of stretchability (~700 % strain) and conductivity [121]. This approach has been successfully implemented to create a wide range of soft sensors, stretchable circuits and antennas [122, 123].

Gallium in the biological context

Gallium is generally considered as a safe material for human handling and environmental

issue [124] [125]. Although Ga has no known physiological function in humans, it can be found naturally in small quantities in the body [126]. Gallium has found applications in the biomedical field and some of its compounds are FDA approved [127]. Therapeutic use of gallium mostly concerns its ionic form however it has also been used in solid alloys and amalgams and more recently in its liquid form.

Ga³⁺ ions: Gallium in its ionic form Ga³⁺ has therapeutic uses for antibacterial therapy [128] [129], cancer treatment [130] and medical imaging [127]. Ga³⁺ is thought to interfere with Fe³⁺ metabolism but on the contrary to iron cannot be reduced to bivalent ion Ga²⁺. Gallium is poorly soluble and requires chelating agents such as citrate and maltolate to be delivered at therapeutically relevant doses [128, 129]. Indeed, gallium ions have a strong tendency to bond with oxygen and forms chelates that limit their availability in aqueous solutions. Under physiological conditions, most Ga³⁺ ions precipitate to form amorphous insoluble Ga(OH)₃ with the following reaction:



Reports on the cytotoxicity of Ga³⁺ are contradictory and have to be taken with caution. Some studies reported cytotoxic effect for concentration larger than $36 \times 10^{-6} \text{M}$ in in-vitro assays to mammalian cells (Balb/c 3T3 fibroblasts) [132] [133]. Other studies supported no cytotoxic effects for concentrations up to $1 \times 10^{-3} \text{M}$ on various cell lines [134] [119] [135].

Solid Ga alloys : Ti-Ga alloys have emerged as potential biomaterials. Qiu et al. [136] reported that Ti-Ga alloy containing 10 wt % of gallium had suitable mechanical properties and cells (L-929 fibroblasts, MG63 osteosarcoma cells) were able to proliferate and adhere on the gallium alloy.

Liquid Ga and Ga alloys : Recently, Lu et al. [137] studied the *in-vitro* and *in-vivo* toxicity of eutectic GaIn alloy nanoparticles as a potential drug delivery vehicle. The liquid metal nanoparticles presented low toxicity against tested cell line (HeLa, 0.2 mM Ga) and injection into mice caused no tissue damage or allergic reaction and exhibited very low acute toxicity (maximum tolerated dose of 700 mg/kg), while both Ga and In metals were effectively removed both faeces and urine as previously suggested [138]. Kurtjak et al. [139] reported low cytotoxicity of hydroxyapatite loaded with metallic gallium nano-spheres (16 wt %) in the concentrations ranging from 0.1 to 1 mg/ml in *in-vitro* cell viability tests (IMR-90 human lung fibroblasts and L929 mouse fibroblasts).

In conclusion, gallium has gathered a lot of interest in the recent years as a potential bio-material in particular for its antibacterial effects. One of the most promising approach, consists of including gallium within implants [140, 141] to achieve controlled local delivery of gallium. Potentially, liquid gallium could also be used to realize stretchable electrical interconnects to within soft implant provided a proper encapsulation and a limited ionic release. If the biocompatibility of gallium in this context is still an open question, early results are encouraging [142].

Problem statement

Despite its interesting physical properties, the practical implementation of gallium for stretchable electronics has been hindered by its cumbrous rheology, making it difficult to process and pattern with conventional techniques [78].

In oxygen free environments, gallium behaves similarly to liquid mercury and does not wet materials like polymers or glass. The high surface tension of gallium (708 J/m^2) [143] prevents the design of free standing structures below the capillary length ($\approx 4 \text{ mm}$). When dispersed in such condition, gallium beads-up and forms puddles with a fixed thickness corresponding to the capillary length [144].

In the presence of oxygen, however, gallium spontaneously forms a solid passivation oxide skin ($\approx 3 \text{ nm}$) [145, 146]. The oxide can counterbalance the surface tension and enables the creation of non-spherical metastable shapes at length scales below the capillary length [122, 147] as shown in figure 4.1.

All alternative printing techniques, such as 3D printing, spraying or doctor blading, rely on the presence of the oxide to stabilise the liquid metal in a metastable state after forcing it into a prescribed shape. The primary limitation of these approaches is the absence of fine control on the thickness and roughness. Applications such as stretchable electronics require such control for creating films with repeatable electrical properties. In particular integration of standard electronic components in thin and stretchable assemblies with available gallium patterning technique is a persistent challenge.

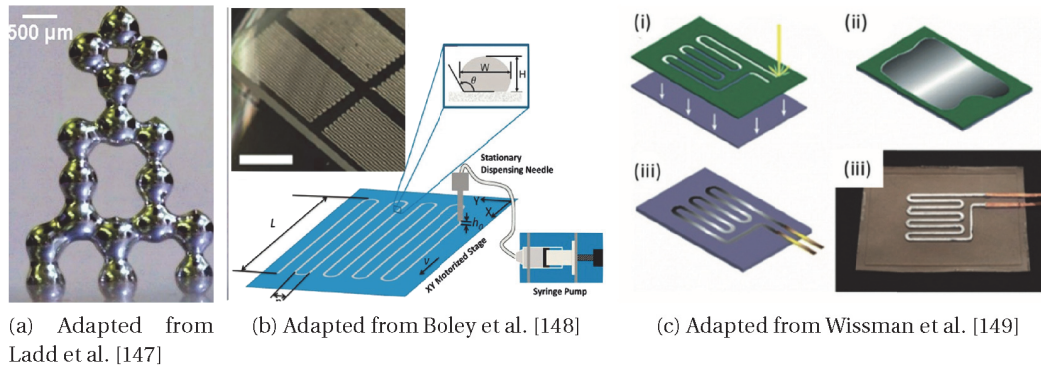


Figure 4.1 – Example of gallium printing techniques

a - 3D printing [147] **b** - Direct printing [149] **c** - Doctor blading through stencil mask [149]

4.1.2 Goal and specific aims

Goal

The overall goal of this chapter is to explore the use of gallium liquid metal to create highly conductive and stretchable interconnects to allow integration of active electronic components

4.2. Intrinsically Stretchable Biphasic (Solid–Liquid) Au/Ga thin film

in soft e-dura implants.

Specific aims

The specific aims of the project are listed below :

- Develop a high precision batch process to create thin films of gallium on silicone elastomer.
- Demonstrate the integration of active electronic components in stretchable assemblies.
- Evaluate the stability of the metalization in a biological environment.

4.2 Intrinsically Stretchable Biphasic (Solid–Liquid) Au/Ga thin film

In this section, a new method to deposit and pattern thin films of liquid gallium on various polymers substrates using thermal evaporation is reported. The growth and electro-mechanical performance of the obtained film is characterized and multilayer integration of active components in stretchable assemblies is demonstrated.

4.2.1 Deposition and characterization methods

Thermal evaporation is a physical vapor deposition process commonly used in the micro-electronics industry. The desired material is placed in a vacuum chamber and heated to form vapor that condenses on a receiving substrate. This process enables a fine control of the amount of material deposited and is particularly suitable to form thin films.

Deposition process : PDMS silicone membranes (100 μm) were prepared on a silicon carrier wafer following the previously described method (appendix A.1.1) and a customised stencil mask (Kapton, Dupont) with the negative of the desired pattern was laminated on the surface of the silicone. 60 nm of gold was then sputtered through the mask (DP 650 or AC 450, Alliance Concept) to form an alloying/wetting layer. Next, a mass of pure gallium ranging from 0.1 g to 1 g was thermally evaporated (VACO 250, Vacotec or E300, Alliance Concept) on the gold-coated substrate. After evaporation the mask was removed to reveal the pattern.

We defined the parameter β as the atomic ratio $\left(\frac{n_{Ga}}{n_{Au}}\right)$ in the biphasic film. Before gallium evaporation, $\beta = 0$. The atomic ratio was calculated from the total mass of gallium evaporated as detailed in appendix A.7. In this study we used β ratios ranging from 3 to 26.

Film characterization methods

Scanning Electron Microscopy : SEM images were acquired in a Merlin microscope from

Zeiss, using the Everhart–Thornley detector at a beam energy of 2 to 3 keV for topography contrast, and the backscattered electron detector at beam energy of 2 to 3 keV and grid voltage of 400 V for compositional contrast.

Atomic force microscope : Atomic force microscope (AFM) images were acquired in a Dimension Fastscan AFM from Bruker with ScanAsyst-Air-HR probes from same supplier.

X-Ray Diffraction Analysis : The analysis was conducted in a D8 Discover diffractometer from Bruker, with a Cu K_α radiation ($\lambda = 1.54 \text{ \AA}$, 0.05° steps, 2 s per step). All samples were prepared and scanned on a float glass support wafer.

Laser Profilometer : Laser profilometer data were acquired using an OLS 4100 from Olympus and further analysed with custom matlab code.

4.2.2 Composition of the film

Evaporation of gallium on the previously gold coated substrate resulted in a heterogeneous film composed of clusters of solid intermetallic alloy AuGa_2 and supercool liquid gallium forming a continuous network and dispersed liquid metal bulges. Figure 4.2a shows a picture of a biphasic gold-gallium obtained on PDMS substrate. On the macroscopic scale the film appeared homogeneous however microscope observations revealed accumulation of liquid gallium in dispersed bulges ($\sim 10 \mu\text{m}$ in diameter). EDS-SEM images shown in figure 4.2b, suggested a higher elemental concentration of gallium in the bulges in accordance with images obtained with BSE detector depicting elemental contrast (figure 4.3.a). X-ray diffraction analysis, presented in figure 4.4, confirmed the presence of the AuGa_2 intermetallic compound.

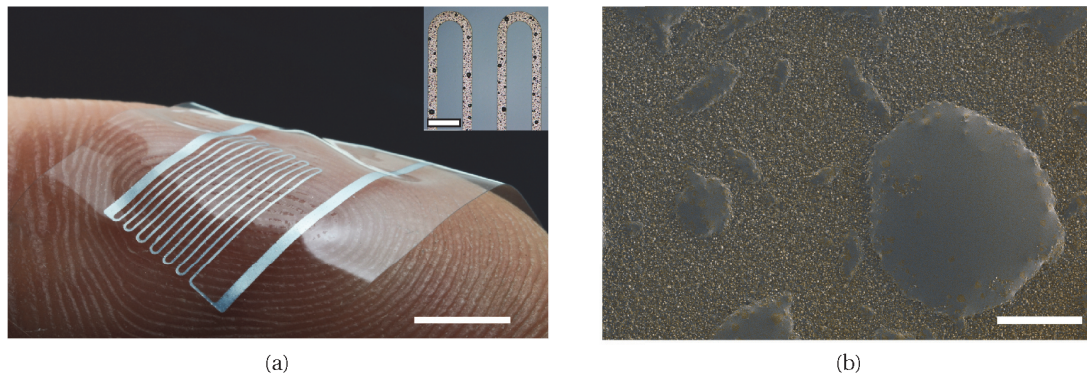


Figure 4.2 – Biphasic Au/Ga thin film

a - Picture of a biphasic gold-gallium film patterned by photolithography with critical dimension of $100 \mu\text{m}$ on a $40 \mu\text{m}$ thick poly(dimethylsiloxane) (PDMS) elastomer membrane. Scale bar: 5 mm; Inset scale bar: $500 \mu\text{m}$ **b** - False color SEM image of the surface of the biphasic gold-gallium film. The yellow and gray colors correspond to the AuGa_2/Ga film and the liquid Gallium, respectively. Color mask was obtained from backscattered electron detector (BSE) image. Scale bar: $5 \mu\text{m}$. Adapted from [107].

4.2. Intrinsically Stretchable Biphasic (Solid-Liquid) Au/Ga thin film

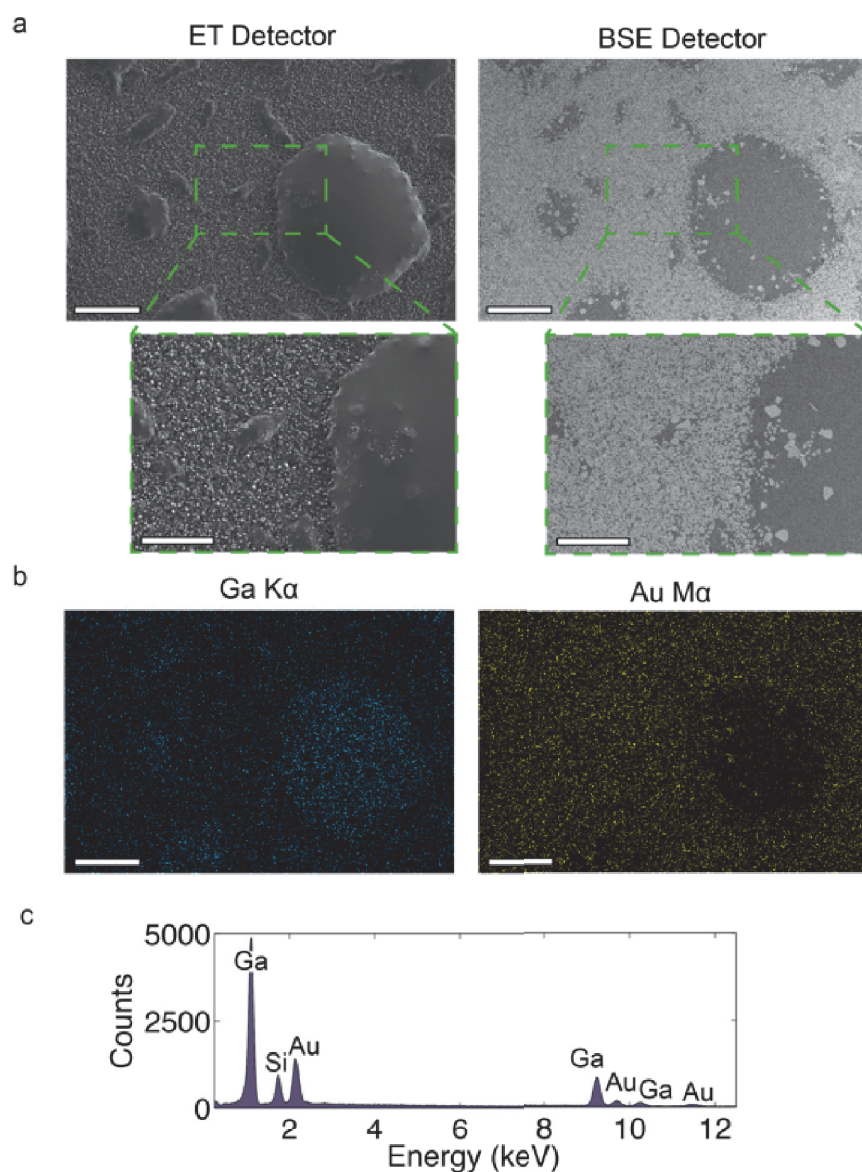


Figure 4.3 – EDS-SEM analysis of the gold-gallium films.

a - SEM images of the surface of a biphasic gold-gallium thin film deposited on a PDMS substrate with Ga/Au atomic ratio $\beta = 13$. Left-hand images were acquired with an Everhart-Thornley (ET) detector. Right-hand images were acquired using a backscattered electron (BSE) detector. Scale bars are 10 μm (5 μm in the magnified views). **b** - Energy-dispersive X-Ray spectroscopy (EDS) mapping of the area observed in **a** for Gold and Gallium. Scale bars are 10 μm . **c** EDS spectrum corresponding to the mapping shown in **b**. Adapted from [107].

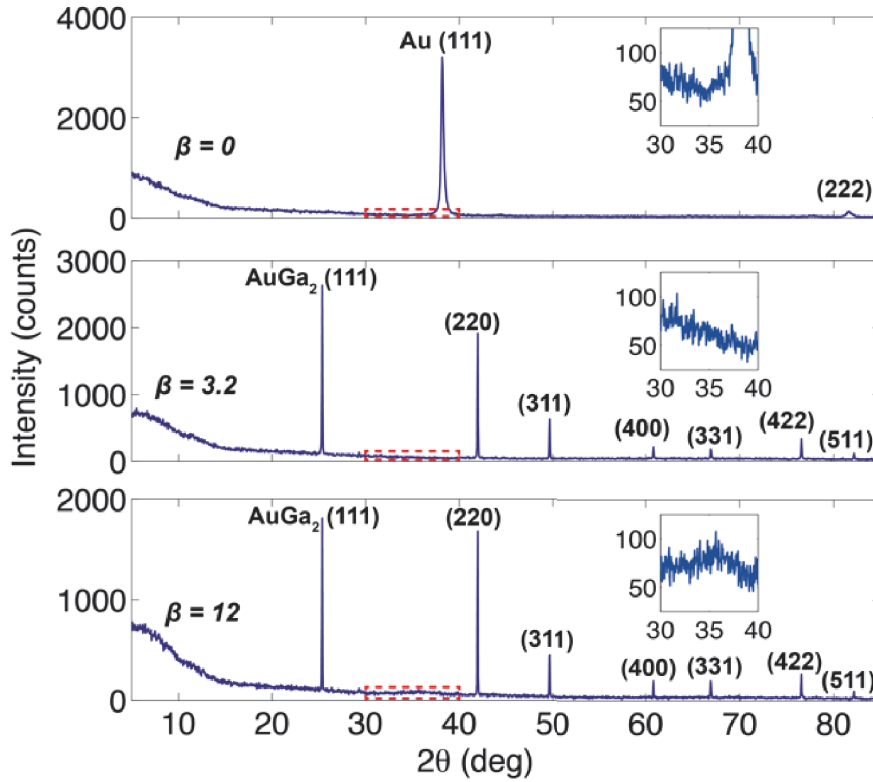


Figure 4.4 – X-Ray diffraction analysis of biphasic gold-gallium thin film.

All samples were prepared by spin-coating a 120 μm thick PDMS layer on a float glass wafer. The PDMS was then coated with 60 nm of sputtered Au and a controlled amount of Ga was evaporated to form the biphasic gold-gallium film. We identified the peaks corresponding to Au (for $\beta = 0$, ICDD PDF Card 00-004-0784) and AuGa_2 (for $\beta = 3.2$ and $\beta = 12$, ICDD PDF Card 01-072-5268). Insets show the increase in baseline signal around 35° attributed to liquid gallium. Adapted from [107].

4.2.3 Role of the Au underlayer :

During the deposition process, the lack of oxygen under vacuum prevented the formation of oxide on the surface of the deposited gallium. At this scale, the shape of the condensing gallium drops is determined only by capillary effect. In the absence of Au underlayer, gallium did not wet the silicone and formed non percolating spherical drops as expected from Young-Laplace equation [144] and shown in figure 4.5. The Au coating acted as a wetting and alloying layer. During the deposition the gallium alloyed with gold forming an inter-metallic compound which allowed the liquid gallium to wet the surface and form a continuous film.

4.2. Intrinsically Stretchable Biphasic (Solid–Liquid) Au/Ga thin film

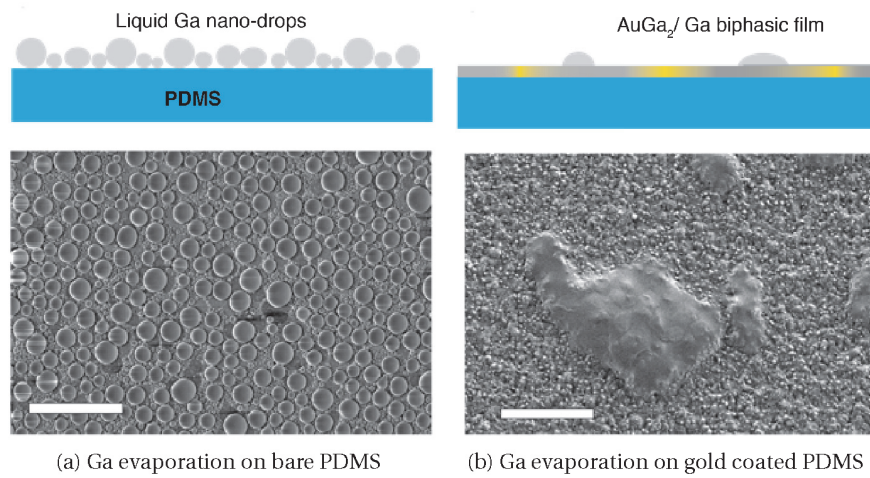


Figure 4.5 – Thermal evaporation of gallium on bare and gold-coated PDMS substrates

Schematic (top) and scanning electron microscope image (bottom) of gallium deposited by thermal evaporation on a bare **a** and gold coated **b** PDMS substrate. On bare PDMS, gallium condensed on the substrate to form a non-percolating layer of micro-droplets while the thin gold coating (60 nm) allowed the gallium to spread by diffusing and alloying. Scale bar is 5 μm . Adapted from [107].

4.2.4 Growth of biphasic thin film

We assessed the growth of the gold gallium films and the transition from a solid to a biphasic material. We prepared samples with different gallium/gold atomic ratio β and we analyzed their surface with scanning electron and atomic force microscopies. Results are gathered in figure 4.6.

Before gallium evaporation, $\beta = 0$. The gold-coated PDMS surface revealed characteristic wrinkles resulting from compressive stress induced by thermal expansion of the elastomeric substrate during deposition of the solid metal film [150].

For $\beta = 3.2$, pronounced buckling with micrometer amplitude and wavelength was observed. The gold film completely alloyed with the evaporated gallium to form the intermetallic compound AuGa_2 as already shown in figure 4.4. Gold–gallium alloying results in large volume expansion (340%) of the film as the lattice constant of the metal increases from 4.08 Å in pure gold to 6.08 Å in AuGa_2 [151]. This likely induces larger compressive stress in the thin film on the PDMS substrate, reinforcing its wavy topography.

As the ratio was increased further ($\beta = 3.9$), the buckling in the film disappeared. This was also concomitant to accumulation of liquid gallium in microscopic bulges of different sizes ($< 1 \mu\text{m}$).

Adding more gallium resulted in a distribution of larger bulges ($< 20 \mu\text{m}$ for $\beta = 13$) while the rest of the AuGa_2/Ga film remained flat. In films prepared with very high β ($\beta = 26$), more than

80% of the film surface area remained thin ($< 1 \mu\text{m}$ thick).

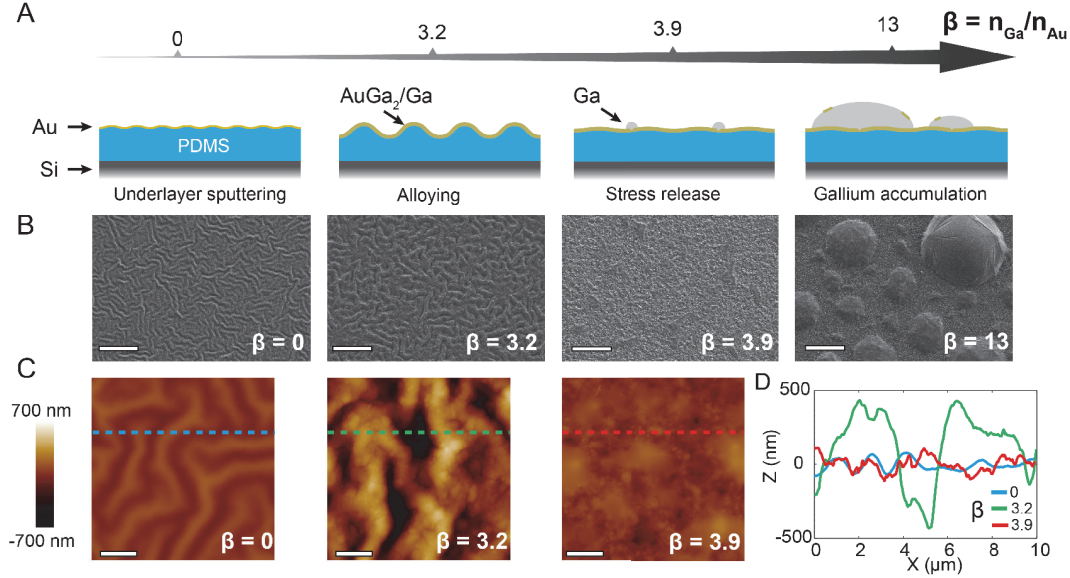


Figure 4.6 – Growth of biphasic gold-gallium thin films on a PDMS membrane.

A. Schematic representations of the growth of the biphasic film on a PDMS substrate as a function of the gallium/gold atomic ratio, β . The PDMS substrate was first coated with a 60 nm thick film of sputtered gold. Gallium was then deposited by thermal evaporation. At $\beta = 3.2$, gallium alloyed with gold to form the AuGa_2 intermetallic compound; an increased roughness was observed. At $\beta = 3.9$, the film flattened and micrometer-size gallium accumulations appeared at the surface of the film. At $\beta = 13$, additional gallium further accumulated to form bulges. **B,C.** SEM and atomic force microscopy (AFM) images of the surface of the biphasic films deposited on PDMS substrates and as a function of increasing β ratio, respectively. SEM scale bar: $10 \mu\text{m}$. AFM scale bar: $2 \mu\text{m}$. **D.** Cross-section profiles along the dotted lines indicated on the AFM scans displayed in C. Adapted from [107].

4.2.5 Surface topography of the film

We evaluated the surface topography of the obtained film using a confocal laser microscope. Figure 4.22 shows the representative topography for a film with $\beta = 12$. As previously described the film was heterogeneous at the micro-metric scale and featured thin protion portions ($< 0.5 \mu\text{m}$) and larger liquid metal drops ($< 1 \mu\text{m}$). The film was characterized with an averaged thickness $\bar{h} = 0.48 \mu\text{m}$, a root mean square roughness $R_q = 1.15 \mu\text{m}$ and a maximum profile height $R_t = 11.58 \mu\text{m}$.

The averaged Young's contact angle formed by the liquid gallium drops on the biphasic film surface was computed from the profilometer data using a custom Matlab code. We interpolated the cross section profile of different drops ($n=10$) with a circular interpolation and computed the contact angle as shown in figure 4.7c. The gallium drops displayed a Young's contact angle $\theta_0 = 22.9^\circ \pm 4.6^\circ$ (mean \pm std).

4.2. Intrinsically Stretchable Biphasic (Solid–Liquid) Au/Ga thin film

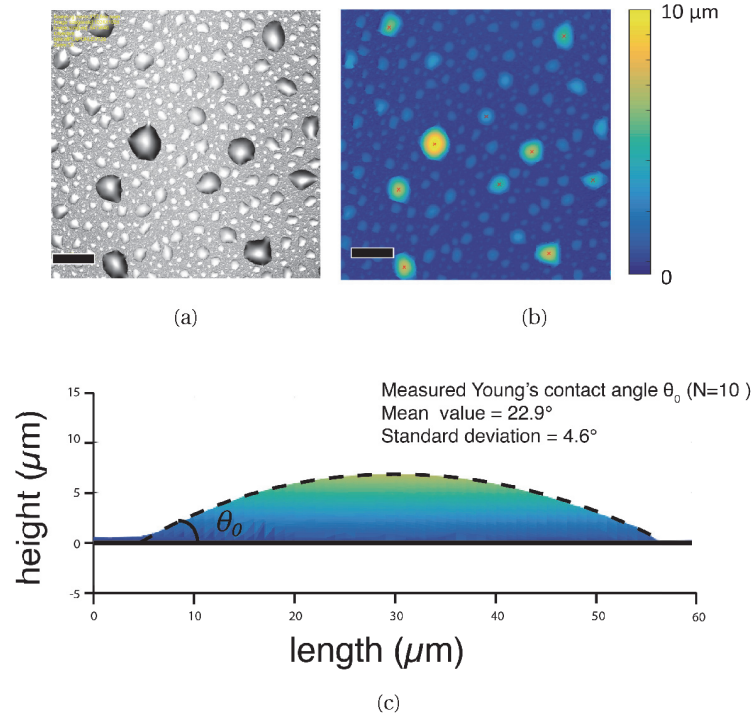


Figure 4.7 – Wetting angle of gallium AuGa₂/Ga biphasic thin film on unstructured PDMS

a,b - Optical image and laser profilometer image of the surface of the gold/gallium biphasic film deposited on unstructured PDMS $\beta = 12$. Drops identified by the red marks were used to compute Young's contact angle θ_0 . Scale bars are 100 μm . **c** - Cross section profile of a drop of gallium on from a biphasic Au/Ga film on PDMS substrate. The dashed line represent the circular interpolation of the drop. Adapted from [108].

4.2.6 Electromechanical properties

In this section, the electro-mechanical characterization of the obtained Au/Ga biphasic thin films for different atomic ratio β are reported. Test samples were uni-axially stretched and subsequent changes of resistance recorded.

Methods : Biphasic gold–gallium thin film conductors were stencil-patterned on 120 μm thick PDMS to produce 15 mm long and 0.3 mm wide electrical conductors. Samples were subsequently cut in 10 mm by 30 mm rectangles and peeled from the wafer. Samples were mounted on a custom-built uniaxial tensile stretcher programmed to actuate two clamps moving in opposite directions along the horizontal plane. Each clamp featured two contact pads that provided constant electrical and mechanical contact to the sample under test. The position of the clamps and the electrical resistance of the conductor, measured using a four-point probe method (2400 source-meter, Keithley), were acquired synchronously at 3.8 Hz on a computer running a dedicated LabVIEW program.

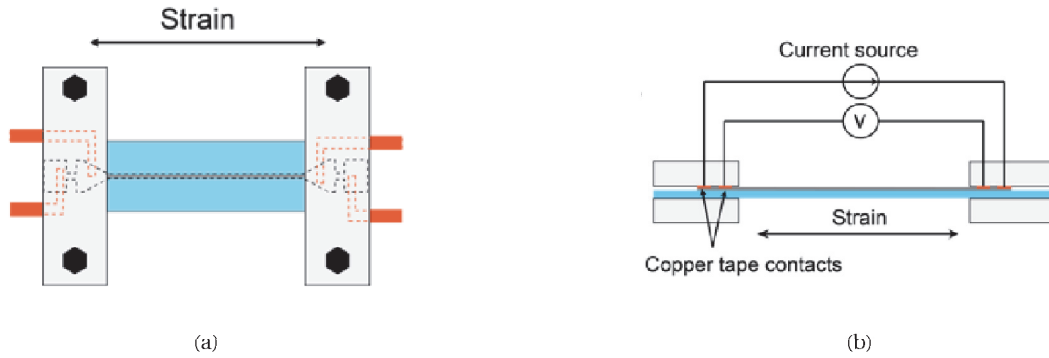


Figure 4.8 – Preparation of samples for electromechanical characterization

Top **(a)** and side **(b)** schematics of clamped samples for electromechanical characterization. Each clamp featured two contact pads that enabled constant electrical and mechanical contact with the tested sample. Resistance of the track, measured using the 4-point probes method (Keithley 2400 source-meter), and the position of the clamps were measured continuously. Adapted from [107].

For fatigue experiments, the stretcher was programmed to perform one million stretch-relaxation cycles (0–0.5 strain at a frequency of 1.4 Hz). Ten times per decade, counting cycles on a logarithmic scale, the stretcher slowed to 0.14 Hz for five cycles in order to record the position of the clamps and resistance of the sample.

Results

Depending on the atomic ratio β the electro-mechanical properties of the films were different as shown in figure 4.9.

Films prepared with $\beta < 3.2$ were conductive after fabrication but failed with catastrophic cracking during release from the carrier substrate and subsequent handling.

For $\beta = 3.9$, the films maintained electrical conduction when strained up to 0.8. For large deformations (strain > 0.1), the amount of liquid gallium available was not sufficient to prevent the formation of cracks thereby leading to irreversible damage in the film and permanent degradation of its macroscopic electrical conductivity. Scanning electron microscopy images suggest the biphasic film coped with the applied deformation by maintaining partial continuity.

In films prepared with $\beta > 6$, liquid gallium percolated throughout the AuGa₂ clusters and maintained electrical continuity in the tested strain range (0–0.8 strain).

4.2. Intrinsically Stretchable Biphasic (Solid–Liquid) Au/Ga thin film

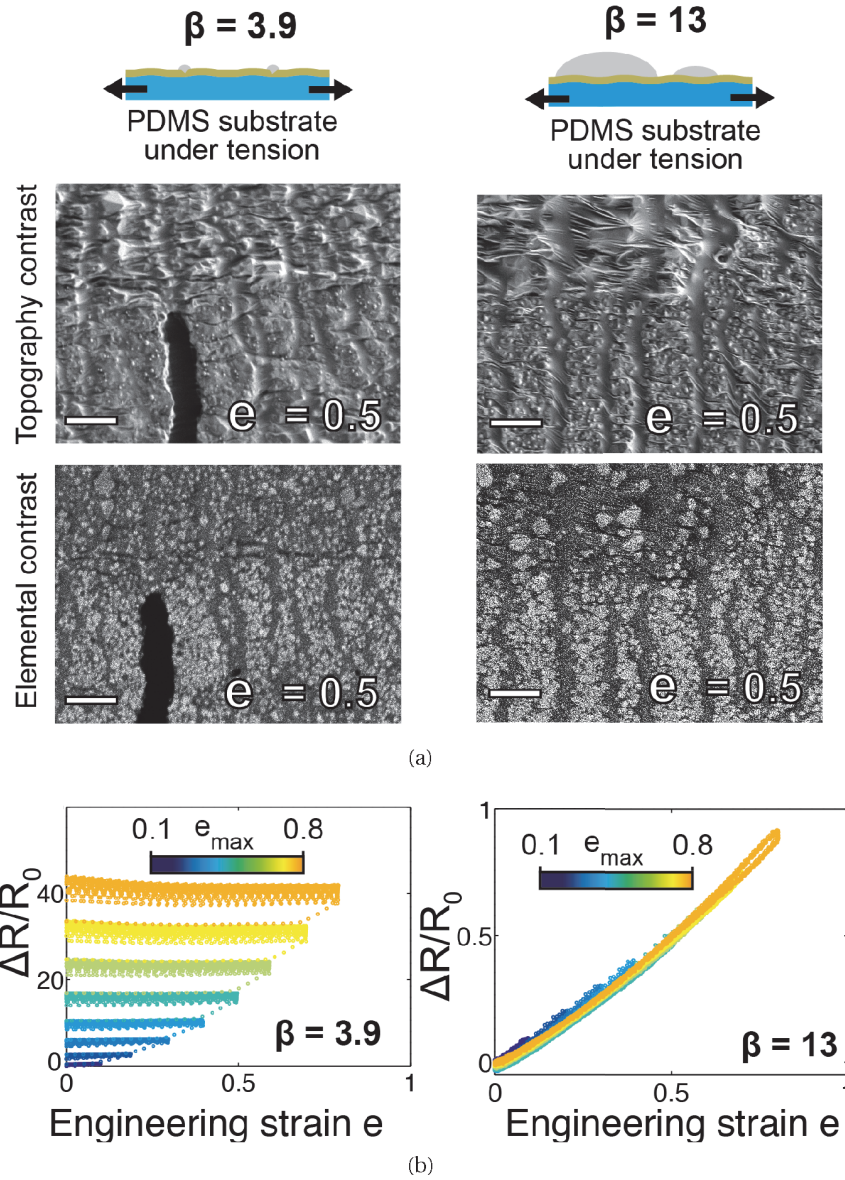


Figure 4.9 – Electromechanical response of biphasic gold-gallium films under large uniaxial deformation

a - SEM images of the surface of biphasic gold-gallium thin films prepared with atomic ratio β of 3.9 and 13 on PDMS substrates. Top and bottom SEM images were obtained with the Everhart-Thornley (ET) detector for topographical contrast, and the backscattered electron (BSE) detector for elemental contrast, respectively. Scale bar: 2 μm . **b** - Relative change in electrical resistance as a function of applied engineering strain e of biphasic conductive tracks prepared with atomic ratio β of 3.9 (left) and 13 (right). The conductors were first cycled twenty times to 0.1 applied strain. Next, every 20 stretch cycles, the maximal applied strain was increased by 0.1 to reach a maximal strain of 0.8. Adapted from [107].

Electro-mechanical metrics

Three different metrics were extrapolated from the experimental data to characterize the electro-mechanical response of the films :

- The initial sheet resistance :

$$R_s = R_0 \frac{l}{w} \quad (4.1)$$

where R_0 is the initial resistance of the sample (before stretching) ; l and w are the length and width of the conductive tracks, respectively. The sheet resistance is reported assuming that the measurement is made over a length scale much greater than the thickness ($l \gg t$) and topology of the film, which can therefore be considered an electrically homogenous material.

- The relative change of resistance after cycling at 0.5 strain :

$$\frac{\Delta R_0^{0.5}}{R_0} = \frac{R_0^{0.5} - R_0}{R_0} \quad (4.2)$$

where $R_0^{0.5}$ is the measured resistance at 0 strain after the sample has been stretched 20 times to 0.5 strain; R_0 is the initial resistance of the conductor.

- The gauge factor (GF) : defined as the slope of the relative change of resistance as a function of the applied strain, and computed using a linear fit on the last cycle at 0.5 maximal applied strain.

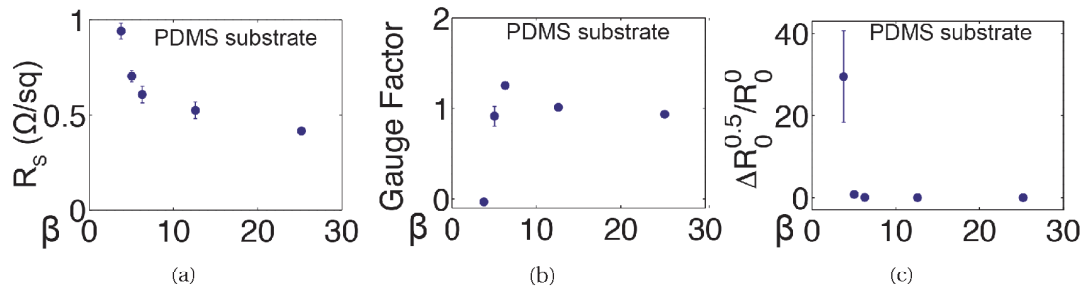


Figure 4.10 – Electromechanical metrics of biphasic thin film

a - Initial sheet resistance ($e = 0$), **b** - gauge factor (calculated over 0.5 strain cycle), **c** - and relative change in electrical resistance ($e = 0$) after cycling to 0.5 maximum applied strain ($n = 3$ samples, error bars: S.D.). Adapted from [107].

For sufficiently high atomic ratios ($\beta > 6$), the biphasic films combined low sheet resistance ($< 1 \Omega/\square$), low gauge factor (≈ 1), and no dependence on strain history. Increasing the amount of gallium deposited past $\beta \sim 10$ did not significantly decrease the sheet resistance below $< 0.5 \Omega/\square$ as most of the conductive material accumulated in the drops.

4.2. Intrinsically Stretchable Biphasic (Solid–Liquid) Au/Ga thin film

Fatigue and maximal strain

We evaluated the fatigue resistance of the biphasic films. A sample ($\beta = 13$) was stretched from 0 to 0.5 strain one million times over a period of 1.5 week. The film withstood the cyclic deformation, displaying minimal variation in resistance over time as shown in figure 4.11a.

PDMS substrates usually broke for strains greater than 120% while the biphasic film remained conductive. We evaluated the maximal strain that the film could handle on a more robust substrate. Ten samples were prepared on a polyurethane substrate ($\beta = 5.2$). The film was stretched to five times its initial length and maintained electrical conductivity as shown in figure 4.11b.

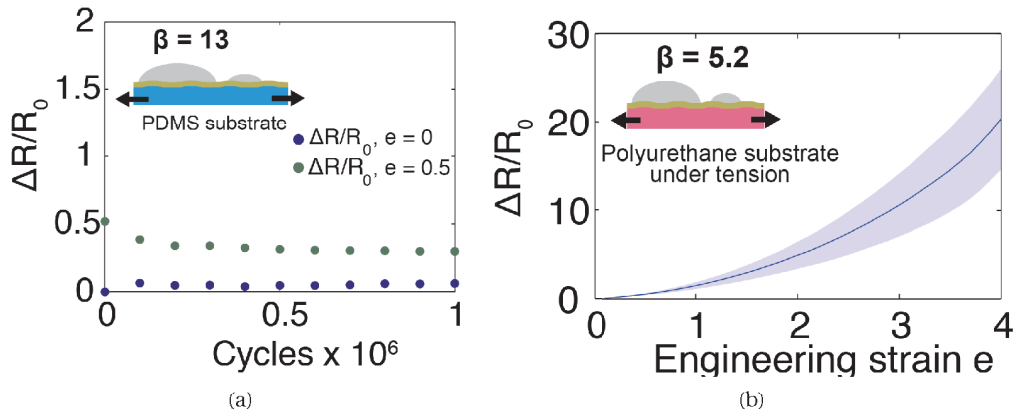


Figure 4.11 – Robustness of biphasic thin film

a - Relative change in electrical resistance over one million cycles to 0.5 strain of a biphasic gold-gallium conductor prepared with the atomic ratio $\beta = 13$. **b** - Relative change in electrical resistance of a biphasic gold-gallium conductor prepared with the atomic ratio $\beta = 13$ deposited on a polyurethane substrate. ($n = 10$ samples, \pm S.D.). Adapted from [107].

Maximal electrical current

We evaluated the biphasic film at high electrical currents (Figure 4.12a). Increments of direct current up to failure of the conductor, were sent to biphasic film test tracks ($\beta = 24$, 15×0.5 mm, $n=3$) while monitoring self heating of the conductor (Joule effect) with a thermal camera. The film rose in temperature and failed at 160 mA for a temperature elevation $\Delta T = 150$ °C. Inspection of the tracks with an optical microscope (Figure 4.12b) showed a depletion of the liquid gallium at the anode edge of the gallium drops that was attributed to electro-migration generated by a local increase in current concentration [152].

To explain the current concentration at the edges of the drops we ran a numerical simulation on a model of the biphasic film conductor. The model consisted of a $500 \mu\text{m}$ wide and $1000 \mu\text{m}$ long film with a thickness of 300 nm . The film had a $21 \mu\text{m}$ drop shaped protrusion in its center forming a spherical cap (23° contact angle). The geometry was meshed by regular hexahedron elements with a $10 \mu\text{m}$ square base and a height of $0.3 \mu\text{m}$. Dirichlet-type boundary conditions

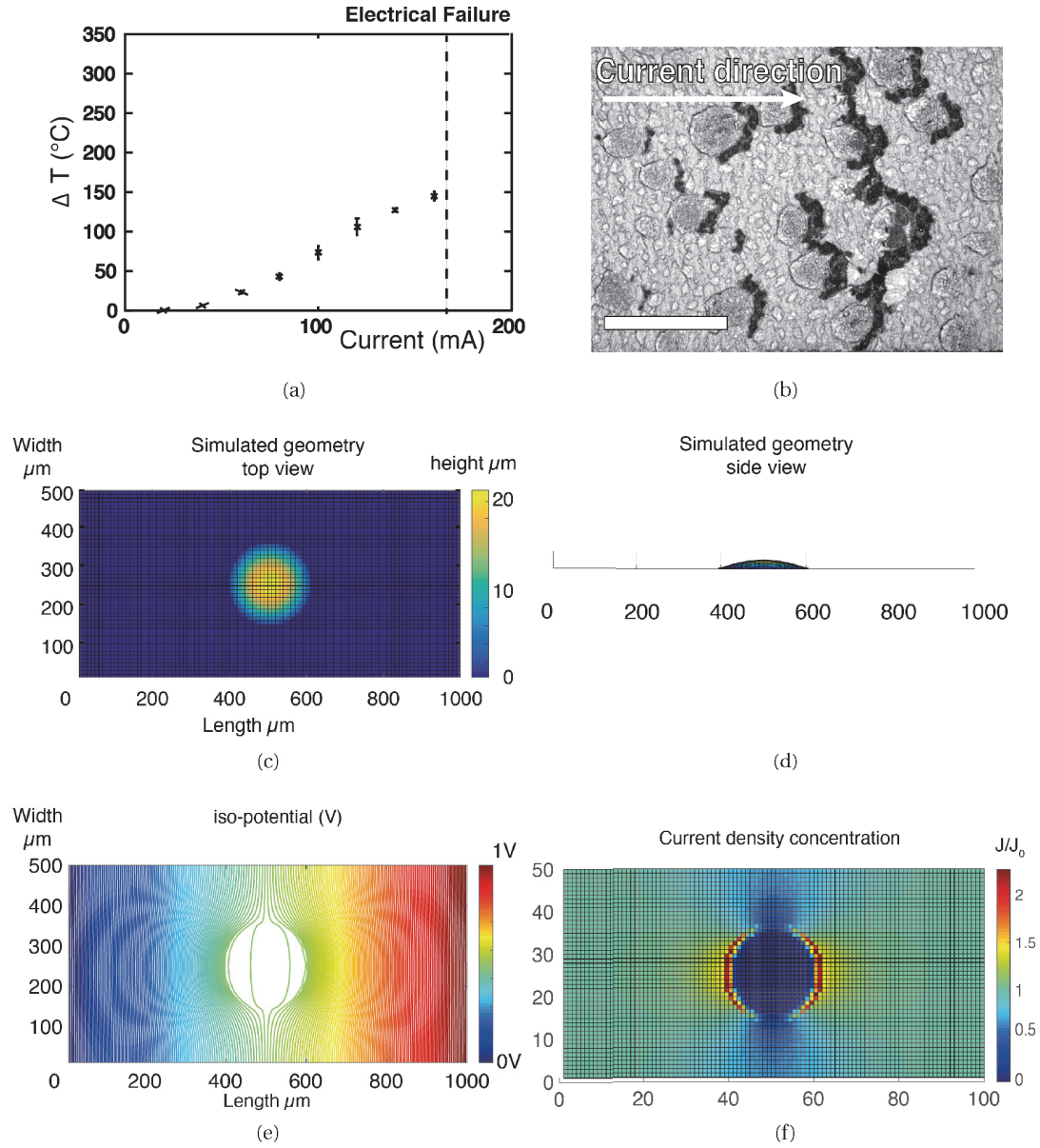


Figure 4.12 – Maximal current and current concentration in biphasic film

a - Elevation of temperature as function of electrical current in a self-heated gold-gallium thin film test tracks ($\beta = 24$, 15×0.5 mm). **b** - Optical microscope images of the failure point of a gallium thin film after running 160 mA. Metal conductor damages are located at the transition between gallium bulges and thinner part of the film. Scale bar is 200 μm . **c** & **d** - Top and side view of the simulated geometry. **e** - Iso-potential distribution in the film. **f** - Normalised current density in the bottom layer of the conductor. Current density at the vicinity of the drop can be twice as much as in the rest of the film. Adapted from [108].

to the potential were applied to the left and right extremities of the film and we solved the potentials using current conservation and Ohm law's as previously detailed [153]. The iso-

4.2. Intrinsically Stretchable Biphasic (Solid–Liquid) Au/Ga thin film

potential curves are shown in figure 4.12e, and the current density in the film are given in figure 4.12f. Current concentrated at the edges of the drops in the main axes ($J > 2J_0$) which corresponded to the areas where gallium depletion was experimentally observed.

4.2.7 Applications

Integration of active electronics

We leveraged the high conductivity and robustness of the biphasic film to fabricate stretchable circuits with conventional active electronics components. We focused on the integration of miniaturized surface mounted (SMD) LEDs to enable optogenetic stimulation capabilities in soft implantable devices.

Methods : Biphasic gold-gallium thin film conductors were patterned on PDMS substrates using stencil masks. Drops of eutectic gallium indium (EGaIn, Sigma–Aldrich) were deposited on the contact pads of the circuits to form small bumps. Surface mounted LEDs (0.5 mm×1 mm × 0.2 mm, 0402, Everlight Electronics) were manually placed and secured with a drop of room temperature vulcanization silicone (734 flowable sealant, Dow Corning). Next, the assembly was coated with a 100 μm thick encapsulating PDMS film and cured at 80 °C for two hours.

We evaluated the electro-mechanical response of the stretchable assembly. A device with one LED interconnected with biphasic thin film was placed in a linear stretcher and current–voltage characteristic I(V) were evaluated for every 0.1 strain increment from 0 to 0.8 applied strain.

Figure 4.13 shows integration characteristic I–V transfer curves for a soft LED microcircuit stretched from 0 to 0.8 uniaxial strain. The assembly maintained function on the full range of deformation while the applied stretch minimally impacted the response of the diode circuit.

Multi-layer assembly

We demonstrated multi-layer stretchable assembly using biphasic film interconnects. Details of the process are given in appendix A.8 and summarized here.

A first membrane was prepared from silicone substrate and patterned with the biphasic film. A second membrane with pre-punched holes at the location of the vias was metallized and then aligned and plasma bonded to the first membrane. Drops of eutectic gallium indium (EGaIn, Sigma–Aldrich) were then deposited in the vias to form a conductive bond between the two metallized membranes.

We used this approach to prepare a stretchable matrix of 4 x 4 green LEDs interconnected with two planes of biphasic conductors as shown in figure 4.14. Powering of the LEDs was controlled and sequenced using an Arduino board. The circular membrane was clamped to

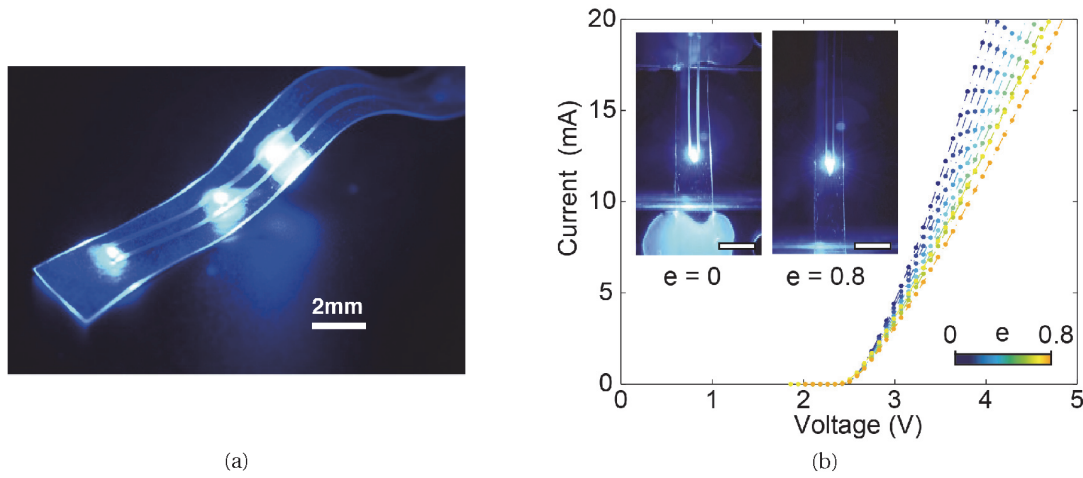


Figure 4.13 – LED integration

a - e-dura with active blue LED optrode **b** - $I(V)$ characteristics of an SMD LED in PDMS interconnected with biphasic gold-gallium conductors as a function of applied uniaxial strain. Scale bar: 2 mm. Adapted from [107].

a rigid frame through which pressurized air was cycled thereby inflating / releasing the soft optoelectronic skin.

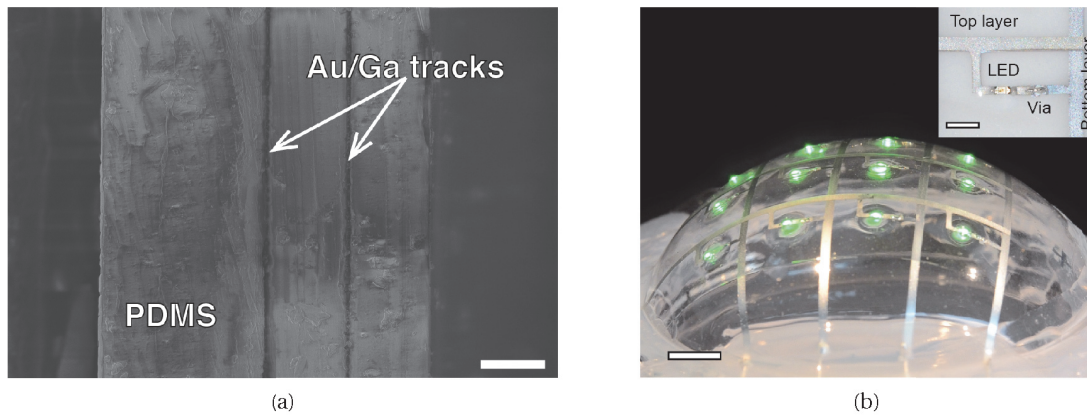


Figure 4.14 – Multilayered biphasic thin film assemblies

a - SEM image of the cross section of a multilayer assembly prepared with PDMS and biphasic gold-gallium thin film interconnects. Scale bar is 20 μm . **b** - Stretchable multilayered matrix of green surface mounted light emitting diodes interconnected and powered through biphasic gold-gallium conductors. Scale bar: 15 mm. Inset: the LEDs are interconnected with two biphasic conductor planes; scale bar: 2 mm. Adapted from [107].

4.2.8 Evidence of gallium corrosion

When used as stretchable interconnect in e-dura implant, the biphasic gold/gallium metalization would not be in direct contact with the biological medium as it would be encapsulated by a layer of silicone PDMS. In this section we evaluated the long-term stability of the biphasic film encapsulated in PDMS in phosphate buffer solution (PBS) over a 14 days period.

Method: Samples ($n=3$) of biphasic film ($\beta=12$, $1\text{ cm} \times 1\text{ cm}$) were prepared on borosilicate glass slide and further encapsulated by $100\mu\text{m}$ of PDMS (sylgard 184, Dow-corning) after plasma activation of the glass surface and fully cured in a convection oven (80°C , 2 h). The samples were then immersed in PBS for 14 days at 37°C .

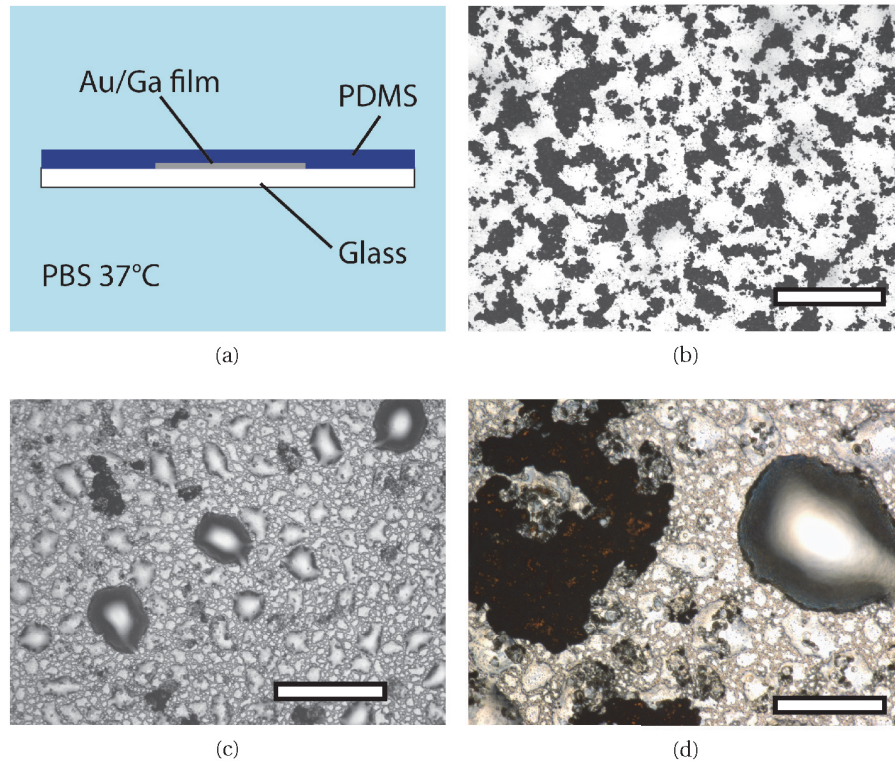


Figure 4.15 – Evidence of Au/Ga biphasic passive skin breakdown and corrosion in prolonged exposition to phosphate-buffered saline (PBS)

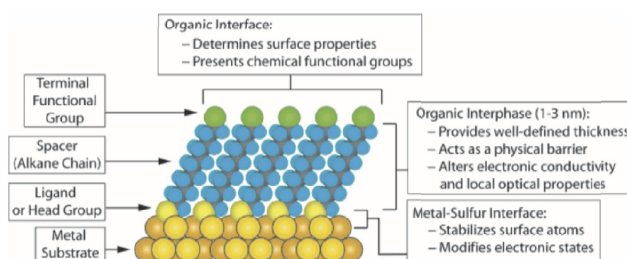
a - Schematic representation of the experimental set-up. Samples were submerged in PBS at 37°C for 14 days. **b** - Sample surface viewed through the glass slide. Scale bar is $100\mu\text{m}$. **c** - Sample surface viewed through the PDMS encapsulation. Scale bar is $100\mu\text{m}$. **d** - Detail of corroded area after 14 days exposition in PBS at 37°C . Scale bar is $60\mu\text{m}$.

Results: Figure 4.15 shows the results of the experiment. After 14 days immersion in PBS, the samples presented multiple points of corrosion, forming dark and dark gold precipitates. The corroded areas were highly visible through the glass slide and seemed to be limited to the thin biphasic part of the film, avoiding gallium drops. These observations confirmed the

results of Elerbrock et al. [154] who observed pitting corrosion of the passive gallium film in PBS. Consequently, a corrosion barrier will be required for applications requiring prolonged exposition to wet environment.

4.2.9 Thiol self-assembled mono-layer as corrosion barrier

Thiol (-SH) terminated organic group are commonly used to create self-assembled monolayers (SAM) on gold surface for a wide variety of applications including biosensors or corrosion protection [155]. These organic molecules form a highly packed and organized mono-layer acting as a physical barrier and altering the electronic conductivity at the metal interface. The thiol group (-SH) is able to form strong bond with different metals including gallium. It was recently used to form stable dispersions of liquid nano-droplets of gallium and gallium indium in aqueous environment [137, 156, 157]. In this section we explored the use of Alkanethiol (1-Octadecanethiol) to form hydrophobic SAMs on the surface of biphasic Au/Ga film and limit corrosion in wet environments.



Adapted from Love et al. [155]

Figure 4.16 – Alkanethiol SAM

Schematic diagram of an ideal, single-crystalline SAM of alkanethiolates supported on a gold surface.

Thiol SAMs are usually prepared by immersing samples in ethanol solution containing diluted thiol. However, thiols can not bond to the surface of oxidized gallium and an alternative approach had to be developed to enable formation of the SAM before the Ga film was exposed to air and formed an oxide passivation layer.

Methods: Boro silicate were sputtered with 60 nm of gold and immersed for 12 hours in a thiol solution (EtOH, 5mM 1-Octadecanethiol) and washed with IPA. Gallium was then thermally evaporated on the sample to form biphasic Au/Ga film. The presence of the SAM was evaluated by measuring the wetting contact angle (Kruss DSA-30E, 30 μ L DI water droplet) on control and treated surface. The samples were then encapsulated in 100 μ m PDMS as described in the previous section and immersed in PBS 37 $^{\circ}$ C for aging. The fraction of corroded surface was evaluated by image analysis from microscope pictures for different time points.

4.2. Intrinsically Stretchable Biphasic (Solid–Liquid) Au/Ga thin film

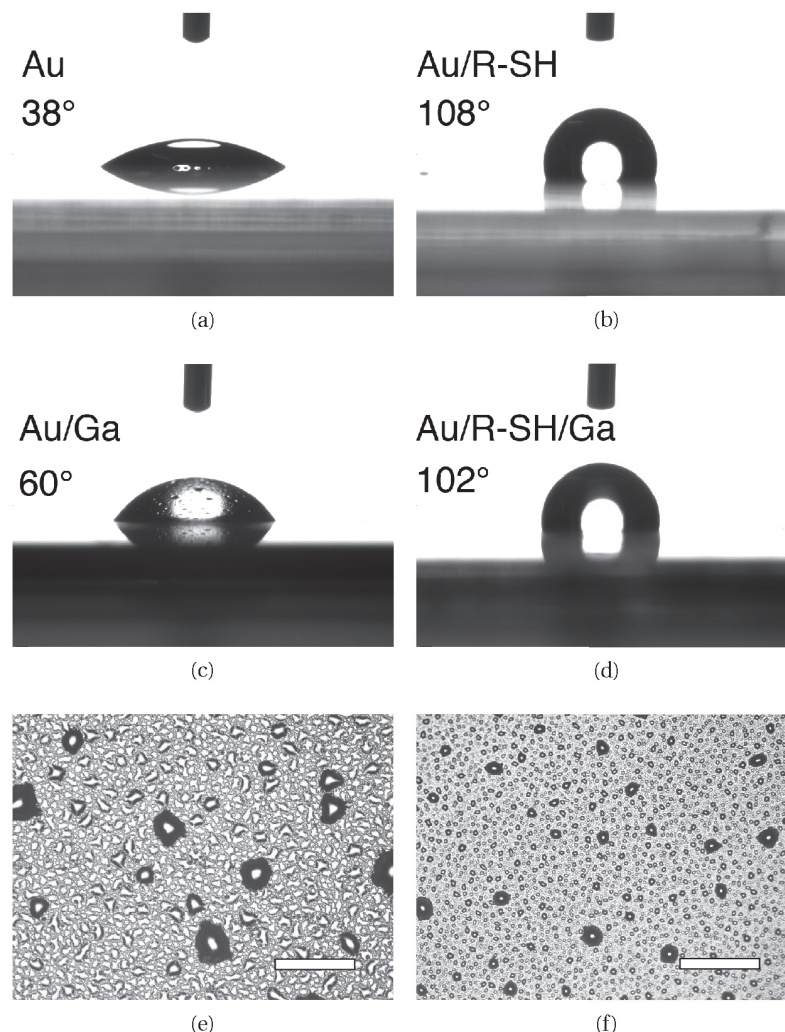


Figure 4.17 – Alkanethiol SAM on Au/Ga biphasic film

Contact angle of DI water droplets on gold coated (60 nm) surface (a), gold surface after 12 h immersion in Alkanethiol/EtOH solution (b), Au/Ga film (c) and gallium evaporated on gold sample treated with alkanthiol SAM (d). - Microscope image of the surface of biphasic Au/Ga film after evaporation on gold coated substrate (e) and gold coated substrate treated with 1-Octadecanethiol SAM layer. Gallium was evaporated on both samples during the same evaporation. Scale bars are 100 μm.

Results : The presence of the SAM was confirmed by measurement of water drop contact angle. Non treated gold surface were hydrophilic (38°) while surface treated with SAM were hydrophobic (108°) as expected. Biphasic Au/Ga film were also hydrophilic (60°) while biphasic film formed on gold treated with SAM conserved an hydrophobic surface (102°).

Biphasic Au/Ga films prepared on SAM treated gold had a noticeably smoother topology ($R_q = 0.548 \mu\text{m}$, $R_z = 8.55 \mu\text{m}$, $R_t = 9.5 \mu\text{m}$) than non treated gold coated samples ($R_q = 1.55 \mu\text{m}$, $R_z = 17.59 \mu\text{m}$, $R_t = 18.6 \mu\text{m}$) as shown in figure 4.17e and 4.17f.

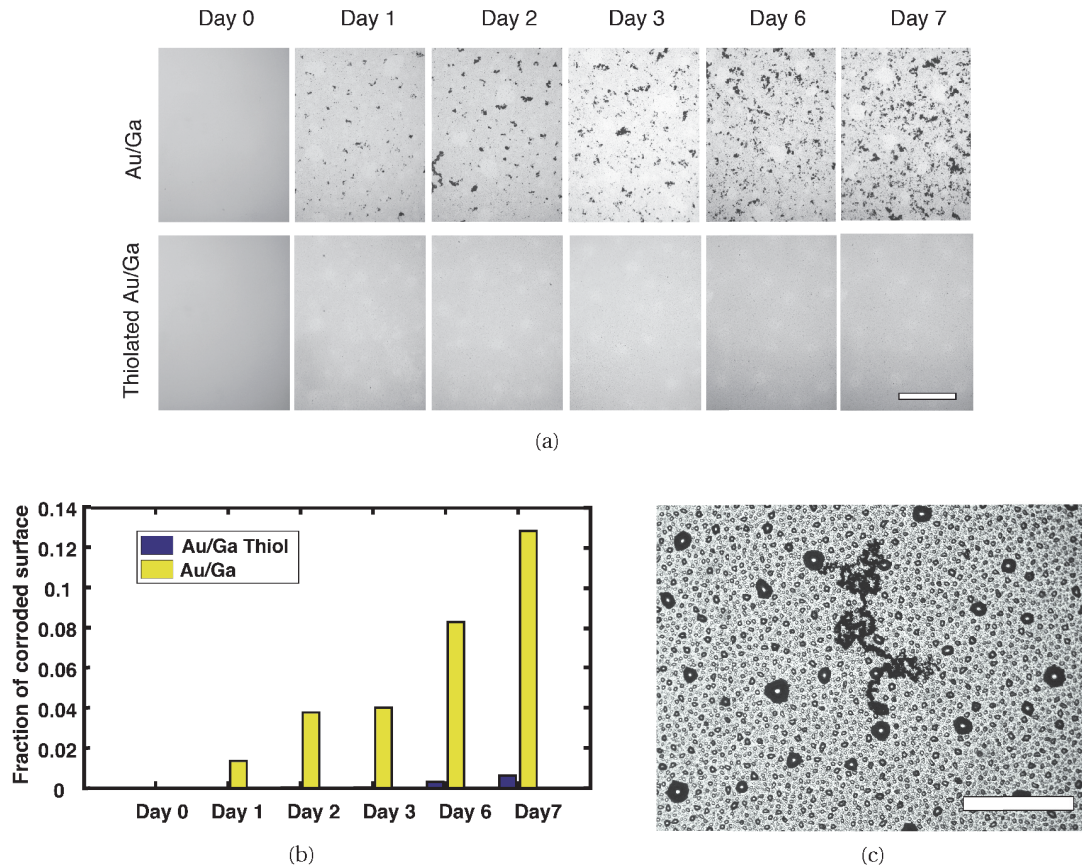


Figure 4.18 – Thiol SAM as corrosion barrier

a - Microscope image of biphasic film view through the glass slide after immersion in PBS. Scale bar is 200 μm . **b** - Fraction of corroded surface for different time points. **c** - Example of pitting corrosion of alkanethiol SAM treated biphasic film after 7 days immersion in PBS at 37 $^{\circ}\text{C}$. Scale bar is 300 μm .

The thiol SAM managed to delay the effect of corrosion in Au/Ga biphasic films as shown in figure 4.18. After one week of exposure to PBS, more than 12% of biphasic film surface was corroded while the film treated with alkanethiol SAM exhibited only 1% of corroded area as shown in figure 4.18b. On the SAM treated films, points of corrosion were more sparse but eventually propagated to large areas as shown in figure 4.18c. The detailed corrosion mechanism is unknown but is thought to initiate at defect points.

Even though this approach gave promising results, the SAMs did not provide sufficient corrosion protection to envision long-term implantable use of biphasic thin film. Alternative SAM formation techniques could be explored, in particular the vacuum chamber could be exposed to vapor of alkanethiol after the gallium evaporation to minimize defects of the SAM. This approach could unfortunately not be tested with the available equipment.

4.3 Engineering the surface of PDMS for smooth tailored liquid metal stretchable thin films

Available gallium deposition techniques are lacking control on the thickness and roughness of the deposited films. Applications such as stretchable electronics require such control for creating films with repeatable electrical properties. In this section I further optimized the PDMS substrate by engineering micro-structures on its surface to produce gallium super-lyophilic substrates. This new approach enabled to achieve smooth films of gallium on extended areas with tailored thickness and sheet resistance. I further derived the condition for the stable growth of smooth films and established a deterministic relation between the geometrical parameters of the micro-texture and the resulting sheet resistance.

4.3.1 Wetting of textured substrates

The wetting behaviour of a liquid to a substrate depends both on the chemical affinity of the materials and the surface topology of the substrate. Water is repelled by hydrophobic substrates, beading up to form drops with contact angles larger than 90° and spreading out on hydrophilic surfaces to form extended drops with a contact angles smaller than 90° . When referencing liquids other than water, the general used terms are lyophobic and lyophilic. The wetting properties can be further enhanced by controlling surface roughness.

Engineering micro-structures such as micro-pillars on a lyophobic substrate increases the contact angle [158] [159], and can be leveraged to produce super-lyophobic surfaces for applications such as self-cleaning surfaces. Similarly, increasing the roughness of a lyophilic substrate reduces the effective contact angle and even leads to the formation of a continuous liquid film through imbibition (wicking) of the surface roughness [160, 161]. Using a similar approach with gallium could enable to create liquid metal thin films.

Bico et al. [164] determined the theoretical thermodynamic imbibition criteria for a given liquid and micro-structured surface. The micro-structured surface is characterized by its solid roughness r (ratio of the actual solid area over its projected one) and its solid fraction ϕ_S (ratio of the surface in the valley to the projected surface). For a flat surface $r \rightarrow 1$ while for a porous medium $r \rightarrow \infty$. When the following criterion is verified the imbibition of the micro-structure is thermodynamically favorable [165] :

$$\theta_0 < \theta_C \text{ where } \cos(\theta_C) = \frac{1 - \phi_S}{r - \phi_S} \quad (4.3)$$

where θ_0 is the equilibrium contact angle on an ideal flat surface with the same chemical composition and θ_C is the critical wetting angle for imbibition.

As $r > 1$ and $\phi_S < 1$, we have $0 < \theta_C < \frac{\pi}{2}$. For a very rough surface ($r \rightarrow \infty$), we then have

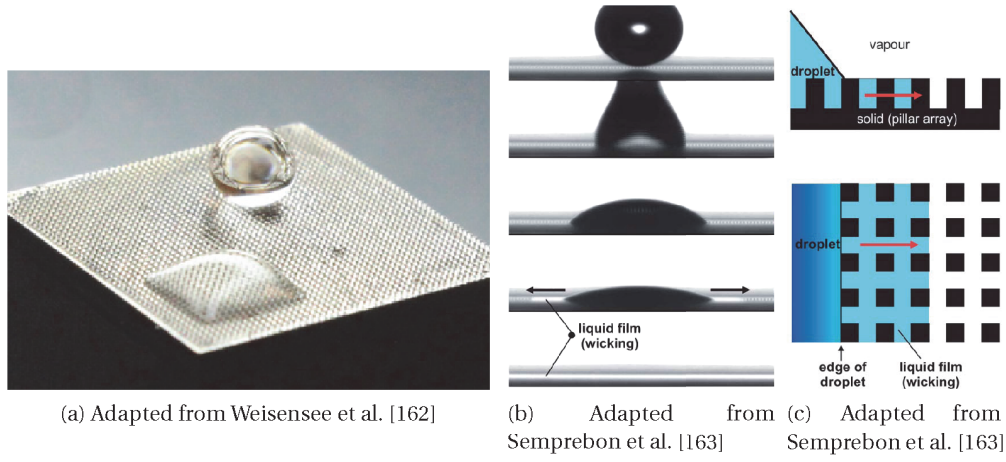


Figure 4.19 – Wetting on micro-structured substrate.

a - Photograph of water (back) and isopropanol droplet (front) on a micro-structured surface. **b** - Spreading of a droplet on a textured surface, followed by wicking which drains the liquid until only a film remains. **c** - Schematic of wicking in a pillar array viewed from the side and above.

$\cos(\theta_C) \rightarrow 0$ and $\theta_C \rightarrow \frac{\pi}{2}$. Consequently any liquid displaying a Young contact angle θ_0 smaller than $\frac{\pi}{2}$ would verify the imbibition criterion.

The imbibition criterion is necessary but not sufficient for a liquid drop to be fully drained in the roughness. Indeed as shown in figure 4.20a, a liquid drop can be pinned in a metastable state and require external energy for the contact line to progress to the next micro-structured pillars [160]. If we approximate the contact line as linear, attached to the top of the last pillar and forming wetting angle θ_0 (figure 4.20b) in the valley. The contact line reaches the next pillars if the following relation is verified:

$$\tan(\theta_0) = \frac{h}{l} \quad (4.4)$$

where h is the height of the pillars and l the inter pillar distance.

Bare silicone PDMS is a gallium lyophobic surface as shown previously in section 4.2.3. Surface modification with the biphasic film approach created a gallium lyophilic surface, enabling liquid gallium to form drops with an averaged contact angle $\theta_0 = 22.9^\circ$. In this section we explored the combination of silicone surface micro-structuring with the biphasic film metalization to create gallium super-lyophilic substrate and smooth liquid metal film by imbibition of the surface roughness.

4.3. Engineering the surface of PDMS for smooth tailored liquid metal stretchable thin films

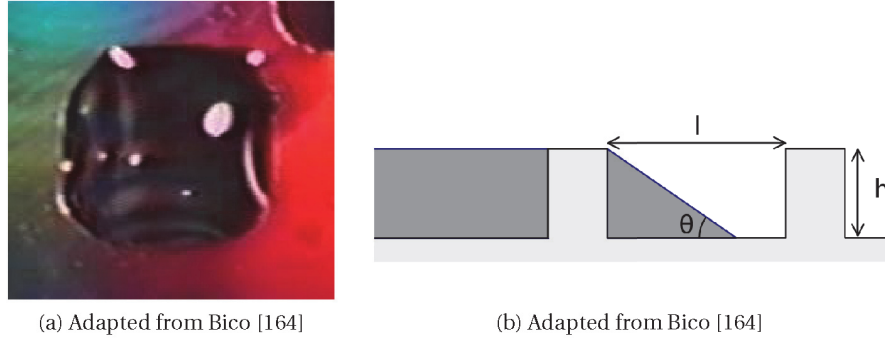


Figure 4.20 – Pinning Condition

a -Metastable pinned drop on a textured substrate **b** Schematic representation of the meniscus contact line between two adjacent micro-structured pillars.

4.3.2 Micro-structured PDMS fabrication

Method : First, micro-structured moulds were prepared using photoresist structuring. 4 in. silicon wafers were exposed to Bis(trimethylsilyl)amine (HMDS) and spin-coated to form a 2 to 5 μm thick photoresist film (AZ-1512 from MicroChemicals) and then cured at 100 $^{\circ}\text{C}$ for 60 s. The resist was then exposed (MLA maskless aligner Heidelberg), developed in diluted AZ-400-K and dried. The wafer was then exposed to a short plasma and treated with a self-assembled layer of trichloro(1H,1H,2H,2H-perfluorooctyl) silane (Sygma Aldrich) in a dessicator. Then micro-structured silicone membranes were reproduced from the mould. PDMS (Sylgard 184, Dow Corning, mixed at 10:1 (w:w), prepolymer:crosslinker) was spin-coated on a micro-structured mould (500 RPM for 1 min) and cured at 80 $^{\circ}\text{C}$ for at least 2 h in a convection oven. The PDMS layer was then pilled-off from the mould and manually transferred, with structured surface facing up, to a 4 in. carrier wafer. A custom Kapton shadow mask patterned with desired layout was aligned and laminated on the micro-structured PDMS substrate. Eventually, 60 nm of gold was sputtered through the shadow mask (AC 450, Alliance Concept).

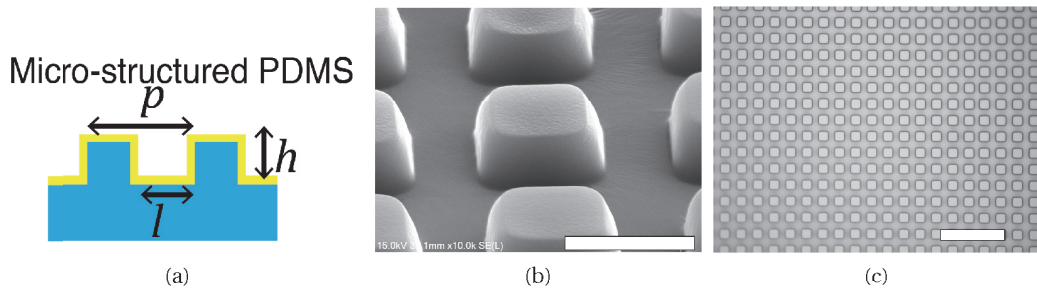


Figure 4.21 – Micro-structured PDMS substrate created by soft-lithography

a Geometrical parameters of the micro-structure: h height of the pillars, l inter pillar distance, p pitch of the pattern. **b** - SEM image of micro-structured PDMS. Scale bar is 5 μm . **c** Optical microscope image of micro-structured PDMS. Scale bare is 32 μm . Adapted from [108].

4.3.3 Gallium evaporation on super-lyophilic substrate

We evaluated the topology of gallium evaporated on different lyophilic micro-structured substrates verifying the imbibition criteria given in equation 4.3. A mass of pure gallium ranging from 0.5 g to 2 g was thermally evaporated (E300, Alliance Concept) on the gold-coated micro-structured substrates and un-structured controls.

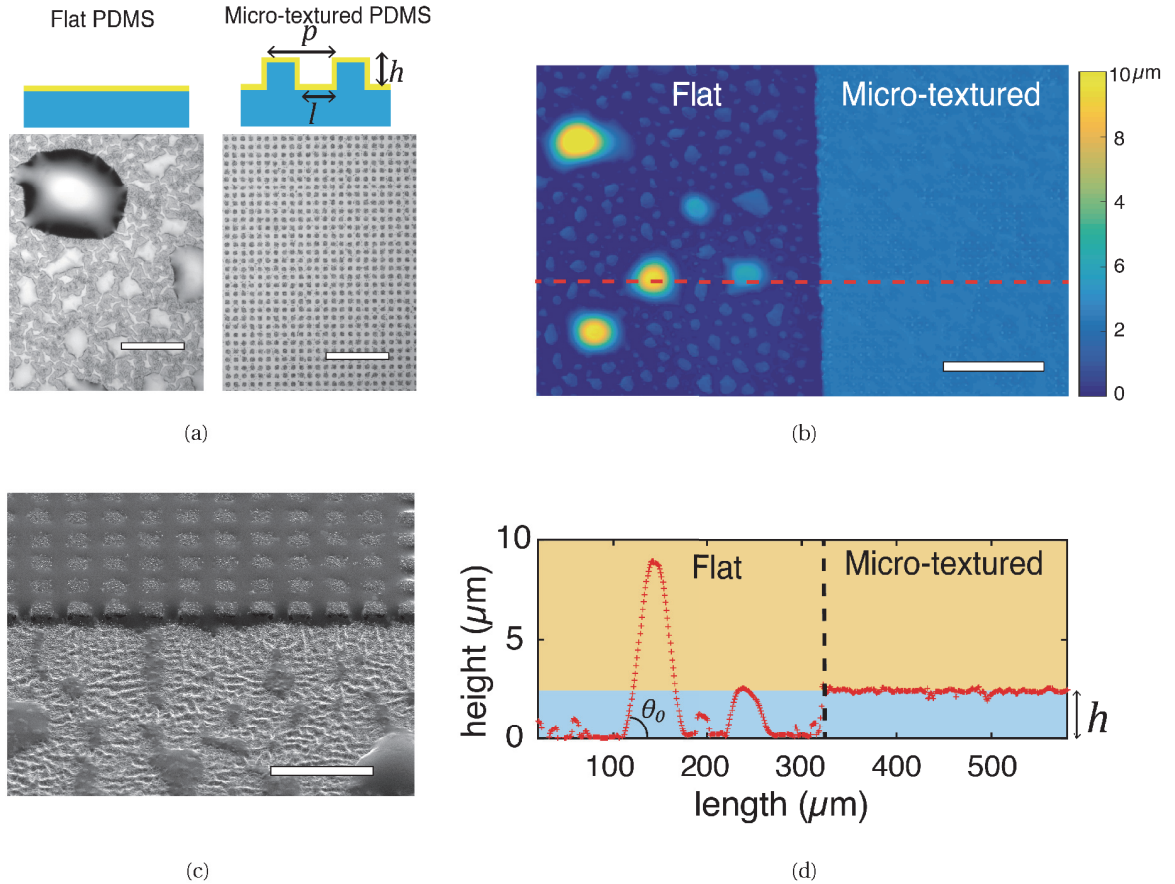


Figure 4.22 – Effect of micro-structured substrate on gallium thin film topology

a - Microscope images of thin film as deposited on flat (left) or micro-structured (right) poly(dimethylsiloxane) (PDMS) substrate. Gallium accumulates in large bulges on flat surface resulting in a highly inhomogeneous film while the liquid metal fills the micro-structure by imbibition to form a smooth film with controlled thickness. Scale bars: 60 μm . **b** - Interferometric optical profilometer image of the surface of the gallium film deposited on mix flat and micro-structured PDMS substrate. Scale bar: 150 μm . **c** - SEM image of gallium deposited on mix flat and micro-structured PDMS. Scale bar is 30 μm . **d** - Cross-section profile along the dotted line indicated on the interferometer image displayed in **b**. Adapted from [108].

Provided a proper choice of the micro-pillars dimensions, imbibition of the micro-structure by the condensing gallium was thermodynamically more favourable than the formation of drops. Thermal evaporation of gallium on the engineered substrate led to the formation of a

4.3. Engineering the surface of PDMS for smooth tailored liquid metal stretchable thin films

smooth film of gallium which, controlled thickness set by the height of the micro-pillars as shown in figure 4.22a.

We assessed the root mean square roughness (R_q) of the obtained film using an interferometric profilometer. Figure 4.22b and 4.22d shows the measured topology after gallium evaporation on a partially micro-structured substrate. The left side was unstructured whereas the right side of the substrate featured micro-pillars with an height (h) of $2.5\text{ }\mu\text{m}$, an inter-pillar distance (l) of $4\text{ }\mu\text{m}$ and a pitch (p) of $8\text{ }\mu\text{m}$. On the unstructured substrate, the gallium formed as in earlier observations an inhomogeneous film ($R_q = 1.6\text{ }\mu\text{m}$) with the majority of the liquid gallium accumulating in drops. On the other hand the structured substrate the gallium accumulated in between the pillars up to their extremity ($h = 12.5\text{ }\mu\text{m}$) forming a smooth film ($R_q = 84\text{ nm}$).

The projected surface area occupied by the liquid gallium was calculated from the pillar's geometrical features: $A = \frac{2pl-l^2}{p^2}$. In this particular case, liquid gallium occupied 75% of the area while the rest corresponded to the pillars. Increasing the inter-pillar distance and pitch maximized the gallium's projected area but eventually led to dewetting of the film.

4.3.4 Imbibition condition

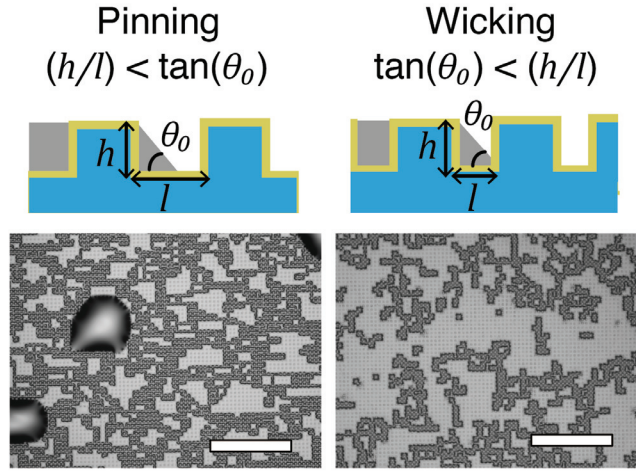


Figure 4.23 – Influence of the micro-texture geometrical parameters on imbibition regime.

Optical microscope images of gallium film in a *pinned* metastable state (left) and in a *wicking* state (right). Both micro-texture consisted in $l=4\text{ }\mu\text{m}$ squared micro pillars spaced by $4\text{ }\mu\text{m}$ with a height of $h=1.5\text{ }\mu\text{m}$ (left) or $h=2.5\text{ }\mu\text{m}$ (right). Scale bars are $150\text{ }\mu\text{m}$. Adapted from [108].

To determine the suitable micro-structure for the formation of a smooth film, we prepared different substrates by varying the height of the pillars (h), the inter-pillar distance (l) and the pitch of the pattern (p). Bico et al. [165] established the condition for imbibition of a liquid drop into a micro-structured substrate. Similarly to the results of Bico et al. presented in section 4.3.1, we observed that depending on the aspect ratio of the pillar ($\frac{h}{l}$) and the wetting properties on a unstructured substrate (θ_0), the condensation of evaporated gallium

on the super-lyophilic substrate either led to a smooth film by imbibition of the pattern when $\tan(\theta_0) < \frac{h}{l}$ or dewetting and formation of drops when $\tan(\theta_0) > \frac{h}{l}$. An aspect ratio $\frac{h}{l}$ close to 0.42 enabled to maximize the projected surface of liquid gallium.

4.3.5 Growth of liquid gallium film on micro-structured substrate

We further characterised the growth of the gallium film assuming that the imbibition criterion was verified (figure 4.24). Only a finite amount of liquid gallium could accumulate within the grooves of the substrate. The pattern was considered saturated when gallium occupied the whole volume in between the pillars. Under the saturation point, the dispersion of gallium was not homogeneous. By capillarity, the liquid gallium rearranges to form a stochastic dispersion of coalesced gallium clusters (figure 4.24b and 4.24c). Increasing the amount of gallium up to the point of saturation resulted in a smooth film. Above the saturation point the excess liquid metal aggregated in large macroscopic drops ($> 500 \mu\text{m}$) sitting on top of the saturated substrate.

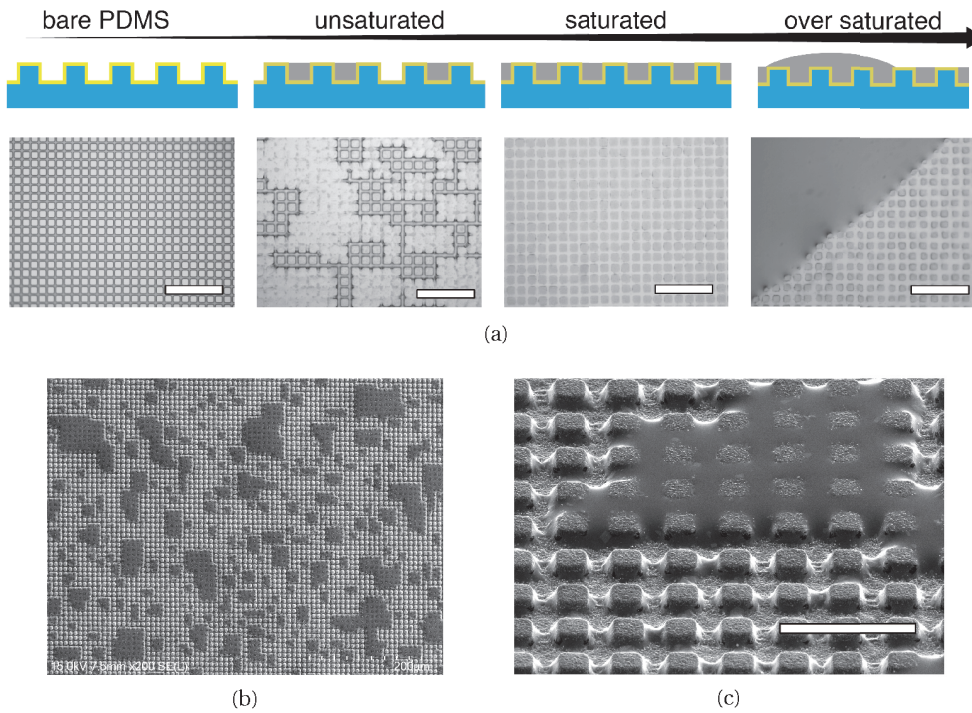


Figure 4.24 – Growth of liquid gallium film on micro-structured substrate

a Schematic representations and optical microscope images of the growth of the gallium film on micro-structured PDMS substrate. Scale bar are $30 \mu\text{m}$. **b,c** - SEM image of unsaturated film on micro-structured PDMS substrate. Adapted from [108].

4.3. Engineering the surface of PDMS for smooth tailored liquid metal stretchable thin films

4.3.6 Electromechanical properties

We next evaluated the electromechanical performance of the obtained saturated films during uni-axial stretching cycles with resistance measurements and scanning electron microscopy (SEM). Test tracks ($15 \times 0.5 \mu\text{m}$) were uni-axially stretched (0–0.8 strain) while measuring the resistance with a 4-point probe set-up. The gallium film on the structured substrate displayed significantly lower resistance compared to the un-structured control while maintaining similar stretchability as shown in figure 4.25a. Figure 4.25b shows a SEM image of a gallium film on a structured substrate under 50% of applied engineered strain. The liquid gallium complied to the deformation and maintained a continuous and homogenous film while the distance between pillars increased as the substrate was stretched.

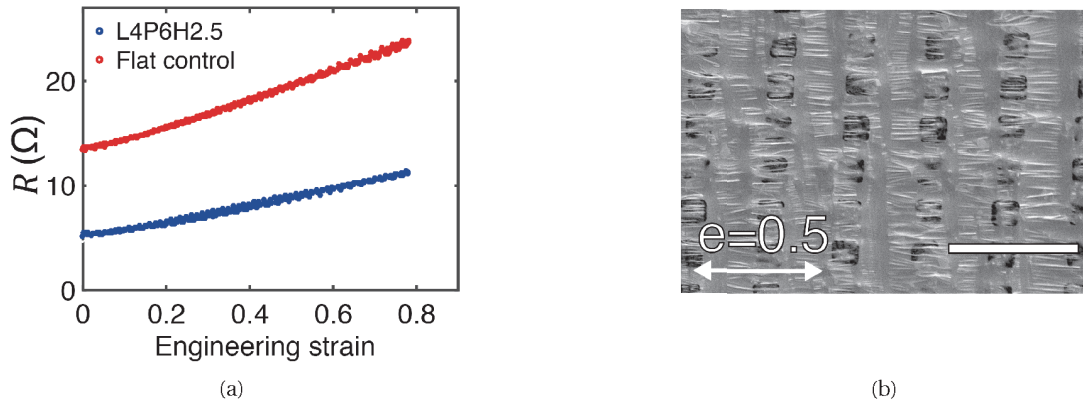


Figure 4.25 – Electromechanical response of biphasic gold–gallium films on micro-structured substrates under large uniaxial deformation

a - Change of electrical resistance as a function of applied engineering strain e of biphasic conductive tracks ($15 \times 0.5 \text{ mm}$) on micro-structured (blue) and flat (red) PDMS substrate. Micro-texture consisted in $2 \mu\text{m}$ squared micro pillars spaced by $6 \mu\text{m}$ with a height of $2.5 \mu\text{m}$ (left) **b** - SEM images of the surface of biphasic gold–gallium thin film on micro-structured substrate under 50% applied engineered strain. Adapted from [108].

We modeled the electrical resistance of the saturated film by a network of resistors as depicted in Figure 4.28a. Due to the symmetry of the system, every node sharing the same abscissa along the principal axis has the same potential. As a result the resistors perpendicular to the main axes can be neglected. The theoretical sheet resistance of the film at the relaxed state then corresponds to the resistance of a unit resistor from the grid and is given by the following equation: $R_{\square} = \frac{\rho_{Ga} p}{hl}$, where ρ_{Ga} is the electrical conductivity of gallium and p, h, l the geometrical parameters of the pillars array.

Consequently the sheet resistance of the film can be tailored to a specific value by choosing the correct geometrical parameters. We compared our model to experimental measurements of the sheet resistance for 6 different micro-pillar designs as depicted in figure 4.28b. The model showed good agreement with the experimental measurements except for one sample

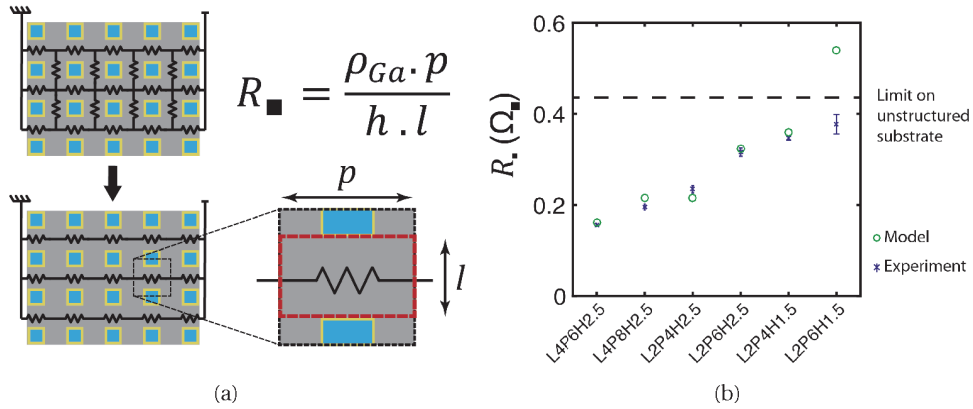


Figure 4.26 – Sheet resistance of biphasic film on structured substrate

a - Equivalent electrical circuit and theoretical sheet resistance as function of geometrical parameters of the micro-pillars. **b** - Theoretical (green) and experimentally measured (blue, mean \pm std) sheet resistance of gallium film on different micro-structured substrates). Adapted from [108].

approaching the resolution limit of the used lithography process.

4.4 Discussion

In this section, the challenges, limitations and opportunities associated with the use of liquid gallium thin films are discussed :

Gallium thin film for long term implant : Despite the very promising electro-mechanical properties of the biphasic Au/Ga thin film, the use of this technology for long-term implantable device is hampered by pitting corrosion of the surface of the film after prolonged exposition to wet environments. Defects in the gallium oxide skin can trigger local corrosion points that eventually propagate to large areas. Elerbrock et al. [154] suggested that Cl^- ions play an important role in this phenomenon. Consequently application in wet environments will require the development of proper water barrier. Indeed PDMS silicone encapsulation is a poor water vapor barrier [166]. Development of stretchable water and gas barriers is an active field of research [167–169] and could provide alternative substrates to package gallium films for applications in wet environments.

Gallium thin film as sensors : In this thesis, we focused on the use of stretchable interconnects to realize soft implants. However the developed liquid metal thin films could benefit other application fields such as wearable electronics or soft robotics. In particular we demonstrated fabrication and functional use of skin-like sensors to finely monitor joint angles or integration of touch sensors in thin compliant membranes as shown in figure 4.27. These aspects are covered with more details in the thesis of Hadrien Michaud [170].

Critical patterning dimensions : Biphasic films were patterned either by stencil mask or

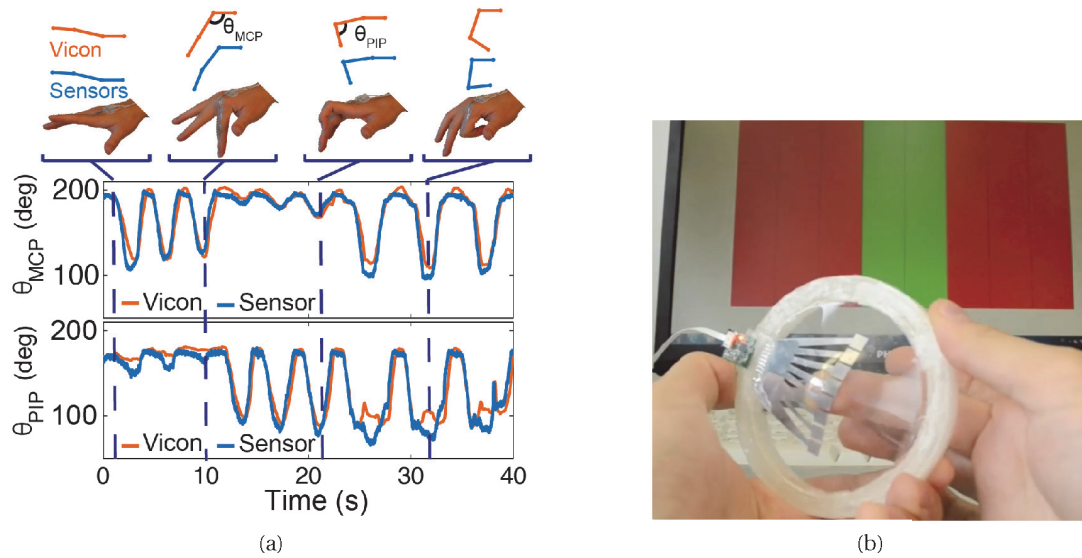


Figure 4.27 – Gallium thin film as sensors

a - Epidermal resistive flexion sensor skin monitoring the position of the metacarpophalangeal (MCP) and proximal interphalangeal (PIP) joints of a finger. Joint angles as a function of time monitored by a soft biphasic gold–gallium sensor (blue) and Vicon motion capture system (orange). **b** - Stretchable capacitive touch sensor. Adapted from [107].

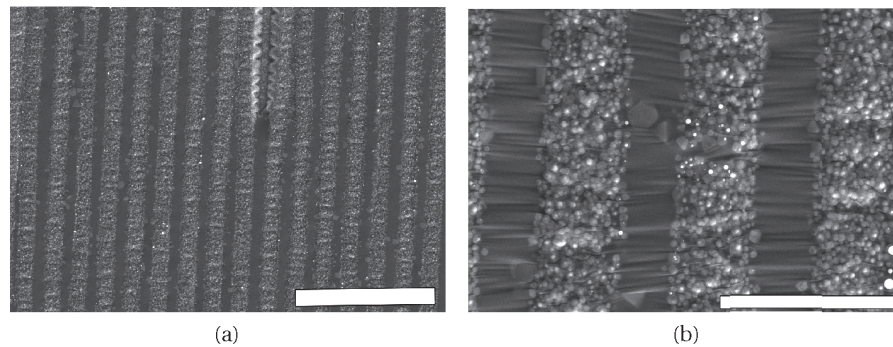


Figure 4.28 – Evaporated gallium on micro-trenches

a,b - SEM image of gallium evaporated on micro-structured substrate featuring micro-trenches. Scale bars are 20 μm in (a) and 5 μm in (b).

through a photo-resist lift-off process as shown in appendix A.9. The lift-off process enabled to reliably form structures of 50 μm with a minimal pitch of 200 μm over large areas. The inhomogeneity of the film and the large gallium drops prevented the proper lift-off of the film for dimensions smaller than 50 μm . While this is sufficient to connect with most standard packaging for SMD components, interfacing bare dies is not possible at the moment and will require more development. Using micro-textured substrates in conjunction with a lift-off

process might enable patterning with smaller critical dimension as it would prevent formation of large gallium drops.

Components integration : We demonstrated proof-of-concept multi-layer circuits, vias and active components integration. The fabrication processes still count several cumbersome manual or wafer to wafer transfer steps that limit the fabrication yield and scalability. Development of tailored automatize equipment would enable a more reliable assembly process. Moreover Gallium is know to alloy with a wide variety of metals. We did not observe any catastrophic diffusion of gallium in the integrated SMD components over the time scale of our experiments. Specific gallium diffusion barriers on components pad might be required for long term applications.

Alternative micro-structured substrate : In section 4.3 we only presented micro-structured substrates consisting of square micro pillar arrays. These micro-structures were convenient to produce and study however many other micro-patterns could be used for various applications. Figure 4.28 shows gallium evaporated on a micro-structured substrate featuring micro-trenches. The resulting film appeared to be anisotropic as gallium accumulated within the trenches. This type of pattern could be particularly interesting too for anisotropic conductors and may find applications for sensors.

4.5 Conclusion

In summary, we introduced a deposition and patterning technique relying only on wetting phenomena to form controlled thin film of gallium on elastomeric substrates. The vacuum deposition technique prevented the oxide skin formation during the deposition while engineering the substrate surface chemistry and topology allowed to overcome the high surface tension of gallium to form extended films below the capillary length.

Compared with peer approaches, our process enabled to form smooth films with tailored thickness and electrical properties while maintaining excellent electro-mechanical performance. These metalizations were used to form complex stretchable multi-layer assemblies with distributed active electronic components that were able to sustain repeated multiaxial mechanical loading. Gallium thin film conductors offer a promising approach to generate stretchable devices and circuits for a wide ange of applications such as tactile electronic skins, deployable circuits, soft robotics, and soft bioelectronics. However, use of gallium thin films in chronic implantable devices will require additional technological developments to prevent or delay pitting corrosion of gallium conductors.

4.6 Contribution

Data presented in this chapter are the result of a team effort :

- I initiated experiments on gallium thin films and led the different experiments presented in this chapter unless stated otherwise.
- Hadrien Michaud participated to the experimental design, characterized the composition of the biphasic films, developed the lift-off patterning of the biphasic films and realized the skin like sensors.
- Aaron Gerratt assisted the design and realization of experiments on the biphasic films.
- Séverine de Mulatier realized the AFM measurements.

5 Conclusion and outlook

5.1 Summary and impact of the work

In this thesis, I reported the fabrication, characterization and functional evaluation of a new class of surface neural interfaces designed to mimic the mechanical properties of the dura mater.

E-dura implants, much like meningeal tissue, are made of soft and compliant materials. E-dura implants conform to the circumvolutions of the brain and spinal cord and can accommodate their dynamic deformations without damaging the surrounding neural tissues. In contrast with conventional neural technologies, e-dura implants are fabricated on soft silicone substrates. Embedded in the implant are stretchable electrodes, electrical interconnects and chemotrodes, which enables bio-potential recording, neural stimulation and localized drug delivery. This multimodal neural interface holds very strong promise for the development of long-term neuroprosthetic systems and brain machine interfaces.

The biointegration of a neural implant within its surrounding meningeal and neural tissue is an important factor for the success of any chronic neuroprosthetics approach. In the second chapter of the thesis, we tested the hypothesis that implants designed to mimic the static and dynamical mechanical properties of targeted tissues display better long-term biointegration. Spinal cord e-dura implants were designed to match rat dura mater and were tolerated by the animals after 6-week subdural implantation, while stiff implants failed to integrate and impaired the animals' mobility. A spinal cord surrogate model was realized to study the biomechanical coupling between implants and neural tissue. During in-vitro experiments the stiff implant failed to accommodate the complex bidirectional curvature of the spinal cord surrogate, which resulted in buckling and large out of plane deformations in the implant. Flexural rigidity for simple unidirectional bending is often used as a design metric for flexible implants. However, we observed that surface implants can undergo two-dimensional bending, which necessarily results in internal stresses and curvature-induced stiffening. Soft material-based implants deform multi-axially while stiff implants buckle, creating locally stiffened folds. This phenomenon is likely to play a significant role in the success of surface implant

biointegration and must be considered in the design of surface implants.

In the third chapter of the thesis, the long-term recording and stimulation functionality of e-dura implants was evaluated through in-vitro and in-vivo experiments. Rodents micro-ECoGs and spinal FES e-dura implants were fabricated using micro-cracked gold stretchable interconnects and platinum/PDMS composite electrodes. A refined fabrication process was developed and resulted in improved fabrication yield and higher electrode density. Devices were subjected to repeated mechanical deformations in saline solution and yet maintained their functionality over several weeks of continuous testing. Additionally, chronically implanted devices provided stable high-resolution neuronal recordings and managed to deliver concurrent electrical and chemical stimuli over extended periods. While translation of the e-dura technology to clinical applications will require further developments, this work provides the first demonstration of such technology in chronic animal experiments and creates a path for the development of novel neurotechnologies.

Integrating active electronic components within e-dura platform, such as LED's optrodes, requires high conductivity stretchable electrical interconnects. Gallium, a liquid metal, is a particularly promising material for high conductivity stretchable electronics, however its practical implementation has been hindered by its difficult processability. In the fourth chapter of the thesis, a new approach for depositing and patterning thin films of gallium was presented. In contrast to peer approaches, formation of surface oxide skin during deposition was prevented by working in vacuum and engineering of the surface topology and chemistry of silicone substrate enabled the formation of smooth and controlled gallium thin films by capillary effect. A deterministic relationship between the geometrical parameters of the substrate micro-structures and the resulting sheet resistance was derived and will enable the fabrication of electrically-tailored stretchable interconnects. The resulting films were also compatible with lift-off patterning and were used to form robust stretchable multi-layer electronic assemblies with distributed active electronic components. In conclusion, this work supports the development of more reliable stretchable electronics by providing repeatable and controlled high performance stretchable electrical conductors. However, development of a proper encapsulation will be necessary to prevent or delay pitting corrosion of gallium in chronic implantable applications. Nonetheless, gallium thin films find also applications in wearable bio-electronic systems and soft robotics.

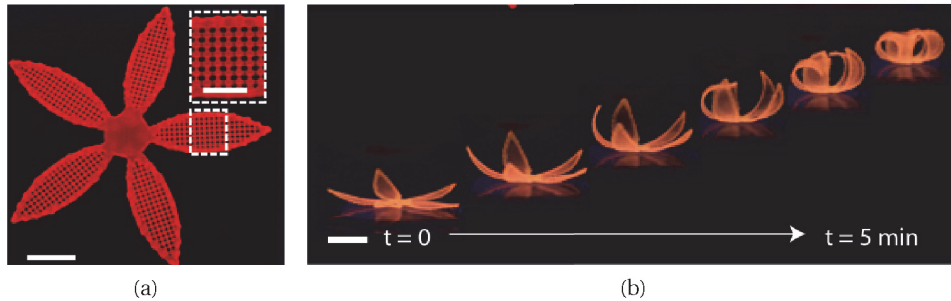
5.2 Future developments and challenges

Based on the results and insights of this thesis work, the following general recommendations are formulated for future work to improve the performance of e-dura neural interfaces design and functionality:

- **E-dura for interhemispheric fissure :** The interhemispheric fissure hosts many regions of interest for neuroprosthetic or BMI applications. In particular, the leg motor cortex

is located in the interhemispheric fissure and cannot be accessed with regular rigid implants. Specific surgical procedures will have to be developed in order to insert the e-dura in this highly vascularized area. For example, a transient packaging or a delivery vehicle might be necessary to provide sufficient rigidity during the insertion of the e-dura.

- **Accelerated aging :** In this thesis, aging of e-dura devices was evaluated over a maximum of 6 weeks *in-vivo* and two weeks *in-vitro*. Extensive aging tests should be performed on e-dura devices to assess their operational stability over decades, as would be required for translation of the technology. Accelerated aging in high temperature and high humidity environments can be used to reduce time of experiments.
- **2.5D surface implant :** In this thesis I used homogeneous isotropic silicone and 2D planar processes to fabricate e-dura implants. Consequently, the resulting devices were flat at relaxed state. Engineering localized prescribed stresses within the substrate could enable generation of 2.5D conformations to match the geometry of the targeted tissue or organ. For example, inclusion of hydrogels within the substrate could be used to generate anisotropic swelling, therefore inducing complex three-dimensional morphologies after immersion in wet environment. The group of Jennifer A. Lewis developed a particularly elegant biomimetic 4D printing process [171] that could benefit for the design of 2.5D surface implant.



Adapted from Gladman, Matsumoto et al. [171]

Figure 5.1 – Complex morphologies generated by biomimetic 4D printing

a - Printed structure. **b** -Resulting swollen structure. (scale bars, 5 mm, inset = 2.5 mm)

- **Integration of application-specific integrated circuit (ASIC) :** Integration of ASICs within e-dura devices could be interesting for several applications. In particular, amplification and multiplexing biopotential signals in closer proximity to the electrodes would reduce the number of electrical interconnects and achieve high throughput biopotential recordings. ASIC can now be produced on ultra-thin flexible silicon chips [172]. However, their integration in e-dura devices will require high density and high conductivity soft to hard interconnects to ASIC and hermetic encapsulation.

A Appendix

A.1 Soft e-dura materials and fabrication process

The fabrication steps of the three components integrated in e-dura implants are detailed below and illustrated in figure A.4 :

A.1.1 Interconnects

1. First a 100 μm thick substrate of polydimethylsiloxane (PDMS, Sylgard 184, Dow Corning, mixed at 10:1, w:w, pre-polymer:cross-linker) was spin-coated on a 3 inch silicon carrier wafer pre-coated with polystyrene sulfonic acid (water soluble release layer). The PDMS substrate was then cured overnight in a convection oven (80 °C).
2. Then a customized Kapton[®] shadow mask patterned with the negative of the electrode layout was laminated on the PDMS substrate. Thermal evaporation of 5/35 nm of chromium/gold (Cr/Au) metal films through the shadow mask deposited the interconnect tracks (Auto 360, Edwards).

A.1.2 Electrical passivation layer

1. The interconnect passivation layer was prepared in parallel. A 5 inch wafer sized, 5 mm thick slab of PDMS was produced and its surface was functionalized with a 1H,1H,2H,2H-perfluorooctyltriethoxysilane (Sigma-Aldrich) release monolayer under weak vacuum. Two thin PDMS layers of 20 μm thickness were sequentially spin-coated on the thick PDMS slab, individually cured then treated with the debonding monolayer. In cross-section, the structure was a triple stack consisting of a thick PDMS slab and two thin PDMS layers. The release coatings allowed for each of the 20 μm thick layers to be peeled off independently at a later stage.
2. Using a hollow glass capillary of a pre-defined tip diameter, both 20 μm thick PDMS

layers were simultaneously punctured at locations corresponding to the sites of the electrodes.

A.1.3 Encapsulation

1. Both PDMS triple stack and interconnect wafers were exposed to brief air plasma activating the silicone surfaces. The triple stack was flipped upside down to align the punctured holes with the underlying electrodes.
2. The two pieces were brought together to form a covalent bond. The thick PDMS slab was peeled off, leaving behind the two 20 μm thick PDMS layers on top of the interconnects.

A.1.4 Soft platinum-silicone composite preparation and patterning

1. E-dura electrode sites were coated with a customized platinum-silicone composite. The conductive composite was a blend of platinum nano-micro particles and PDMS (Sylgard 184, Dow Corning). The PDMS pre-polymer, mixed with its cross-linker, was diluted in heptane in a 1:2 w:w ratio to create a low viscosity liquid. In a small container, 100 mg of platinum microparticles (Pt powder, particle size 0.5-1.2 μm , Sigma-Aldrich) was added to 5 mg of PDMS (15 μL of heptane diluted PDMS). This mixture was thoroughly stirred and put aside for evaporation of the heptane fraction. The addition of 5 mg doses of PDMS was repeated until the mixture (after heptane evaporation) became a paste. Paste formation occurs when the PDMS content is 15-20% by weight. Immediately before dispensing onto the electrode sites, the paste may be thinned with a drop of pure heptane.
2. To form the active electrode coating, a bolus of conductive composite paste was printed i.e. spread and pressed into the holes of the upper encapsulation layer.
3. The upper encapsulation layer was then peeled off, leaving bumps of conductive composite precisely at the active electrode sites. The bottom 20 μm thick PDMS layer remained permanently bonded to the electrode-interconnect e-dura substrate, thereby providing electrical encapsulation. The array was placed in a convection oven at 60 $^{\circ}\text{C}$ overnight to ensure full polymerization of the conductive paste.

A.1.5 Microfluidic and connector integration

1. To form the microfluidic delivery system, an additional 80 μm thick PDMS layer was bonded to the metallized e-dura substrate. This layer covered approximately a third of the length of the implant and contained a central microfluidic channel (100x50 μm in cross section), terminating 2 mm caudally from the 3 caudal electrodes. The connector side of the microchannel was interfaced with a polyethylene capillary (0.008" i.d., 0.014" o.d., Strategic Applications Inc.) and sealed with a bolus of fast-cure silicone (KWIK-SIL,

A.1. Soft e-dura materials and fabrication process

World Precision Instruments).

2. A custom-made soft-to-wires electrical connector was assembled for all the e-dura implants. De-insulated ends of 'Cooner' wires (multistranded steel insulated wire, 300 μ m o.d., Cooner wire Inc.) were carefully positioned above the terminal pads of the gold film interconnects. The electrical contact was enhanced by 'soldering' the wires to the contact pads with a conductive polymer paste (H27D, component A, EPO-TEK) deposited below and around each electrical wire. To stabilize the connector, the 'solder' connection area was flooded with a silicone adhesive to form a package (One component silicone sealant 734, Dow Corning)

A.1.6 Release

1. The contour of the finished implant was cut out from the wafer using a razor blade. The implant was released from the carrier wafer upon a brief immersion in water.

Appendix A. Appendix

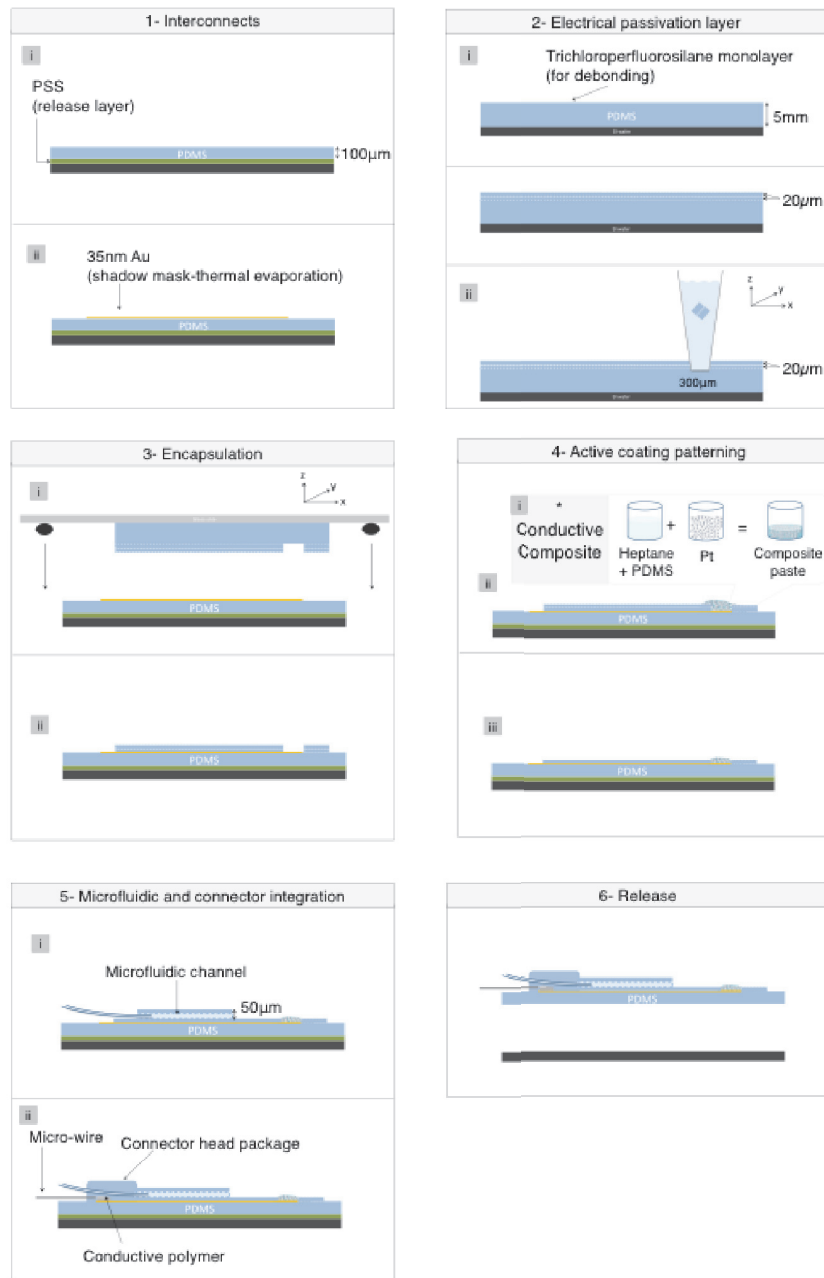


Figure A.1 – Soft neurotechnology for e-dura implants

The process flow, illustrated in cross-sectional views, consists of 6 main steps. (1) Elastomeric substrate and stretchable interconnects fabrication. Patterning (2) and bonding (3) of interconnects' passivation layer. (4) Coating of the electrodes with a customized platinum-silicone composite screen-printed above the electrode sites. (5) Integration of the PDMS microfluidic channel and connector. (6) Release of the e-dura implant in water.

A.2 Compression modulus of the hydrogel

Verification of the compression modulus of the hydrogel was conducted through an indentation test. A large slab (6 cm thickness, 12 cm diameter) of gelatin hydrogel was prepared and indented with a spherical indenter (6 mm diameter) mounted on a mechanical testing platform (Model 42, MTS Criterion). By fitting a Hertz contact model to experimental force versus displacement data we obtained a compressive elastic modulus of 9.2(6) kPa (n=5 test runs) for the 10% gelatin hydrogel.

$$F = \frac{4}{3}ER^{\frac{1}{2}}d^{\frac{3}{2}} \quad (\text{A.1})$$

where F is the normal indentation force, E the compressive modulus of indented hydrogel, R the radius of the indenting sphere, and d the indenting depth.

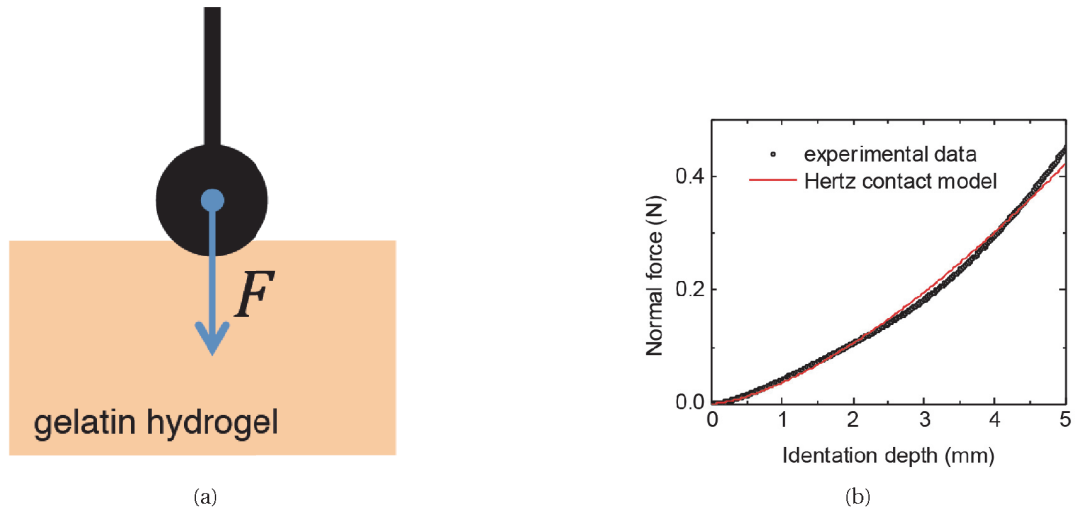


Figure A.2 – Evaluation of gelatin stiffness for spinal cord surrogate

a - Schematic of indentation test on gelatin slab. **b** - Normal force as function of indentation depth (black) and hertz contact model fitting (red).

A.3 Mechanical spinal cord surrogate model fabrication process

A.3.1 Dura surrogate

Dura surrogate was fabricated from PDMS. One end of a polystyrene rod (20 cm long, 3.2 mm diameter) was attached to the drive shaft of a mixer. The mixer was positioned so that the rod was horizontal and rotating about its long axis, approximately a centimeter above the surface of a hotplate. Several grams of freshly prepared PDMS pre-polymer (Sylgard 184, Dow

Appendix A. Appendix

Corning) were dispensed along the length of the rotating rod. By adjusting the rotation speed, the distance between rod and hotplate, and the hotplate temperature, the thickness of the PDMS film that coated the polystyrene rod was controlled. Following thorough curing of the silicone coating, the polystyrene core was dissolved by immersion in acetone overnight. Thorough rinsing and de-swelling of the silicone in water left a PDMS tube with wall thickness ranging 80-120 μm . One end of the tube was pinched and sealed with a bolus of fast-cure silicone (KWIK- SIL, World Precision Instruments), the other end was trimmed to a total tube length of 8.5 cm.

A.3.2 Spinal cord tissue surrogate

Artificial spinal tissue was fabricated from gelatin hydrogel. Warm ($\approx 40^\circ\text{C}$) gelatin solution (10% gelatin by weight in water, gelatin from bovine skin, Sigma-Aldrich) was poured into a silicone mold containing a cylindrical cavity, 3.2 mm in diameter and 10 cm long. The mold was then placed in a fridge for 1h to allow for the gel to set.

A.3.3 Assembly of surrogate

The gelatin ‘spinal tissue’ was recovered from the mold and placed in a desiccator under mild vacuum for several hours. Partial loss of water content caused shrinkage and stiffening of the gelatin ‘spinal tissue’. This allowed for its insertion inside the surrogate dura mater tube together with a stiff or soft implant. The assembled model was then immersed in water overnight to re-hydrate the hydrogel ‘spinal tissue’ and secure the implant in the artificial intrathecal space. The open end of the model was then sealed with quick setting silicone and the model was ready for mechanical tests.

A.4 Micro-Computed Tomography

A.4.1 Micro-Computed Tomography of spinal cord surrogate model

Non-destructive computed tomography (CT) reconstructions of the spinal cord model were obtained with a Skyscan 1076 scanner (Bruker microCT, Kontich, Belgium). The following settings were used: accelerating voltage 40 kV, accelerating current 250 μA , exposure time per image 180 ms, angular resolution 0.5° . The resultant projection images were reconstructed into 3D renderings of the model using NRecon and GPURecon Server (Bruker microCT, Kontich, Belgium). The resultant volumetric reconstructions had a voxel size of 37 μm . This limit prevented the direct visualization of stiff implants, whose thickness was 25 μm .

A.4.2 In-vivo micro-computed tomography of implants

Imaging of implanted e-dura (5 weeks post implantation) was conducted in the same scanner. Rats were kept under Isoflurane anesthesia during the scan to reduce motion artifacts. Scanner settings were adjusted to avoid artefacts induced by metallic parts of the spinal orthosis (typical settings were: 1 mm aluminum filter, voltage 100 kV, accelerating current 100 μ A, exposure time 120 ms, rotation step 0.5). Prior to imaging, a contrast agent (Lopamiro 300, Bracco, Switzerland) was injected through the microfluidic channel of the implants to enable visualization of soft tissues and e-dura. Segmentation and 3D model were constructed with Amira® (FEI Visualization Sciences Group, Burlington, USA).

A.5 Histology and Morphology of explanted spinal cord

A.5.1 Immunohistochemistry protocols

Microglial and astrocytic reactivity was revealed by performing immunohistological staining against glial fibrillary acidic protein (GFAP) and ionized calcium binding adapter molecule 1 (Iba1), respectively. Briefly, lumbosacral spinal cord coronal sections were incubated overnight in serum containing anti-Iba1 (1:1000, Abcam, USA) or anti-GFAP (1:1000, Dako, USA) antibodies. Immunoreactions were visualized with appropriate secondary antibodies labeled with Alexa fluor® 488 or 555. A fluorescent counterstaining of the Nissl substance was performed with the Neurotrace 640/660 solution (1:50, Invitrogen, USA). Sections were mounted onto microscope slides using anti-fade fluorescent mounting medium and covered with a cover-glass. The tissue sections were observed and photographed with a laser confocal fluorescence microscope (Leica, Germany).

Immunostaining density was measured offline using 6 representative confocal images of lumbosacral segments per rat. Images were acquired using standard imaging settings that were kept constant across rats. Images were analyzed using custom-written Matlab scripts according to previously described methods [89]. Confocal output images were divided into square regions of interest (ROI), and densities computed within each ROI as the ratio of traced fibers (amount of pixels) per ROI area. Files were color-filtered and binarized by means of an intensity threshold. Threshold values were set empirically and maintained across sections, animals and groups. All the analyses were performed blindly.

A.6 Surgical procedures complement

A.6.1 Implantation of electrodes to record muscle activity

Bipolar intramuscular electrodes (AS632; Cooner Wire) were implanted into the tibialis anterior and medial gastrocnemius muscles, bilaterally. Recording electrodes were fabricated by removing a small part (1 mm notch) of insulation from each wire. A common ground wire (1 cm of Teflon removed at the distal end) was inserted subcutaneously over the right shoulder. All electrode wires were connected to a percutaneous amphenol connector (Omnetics Connector Corporation) cemented to the skull of the rat. The proper location of EMG electrodes was verified post-mortem.

A.6.2 Spinal cord injury

Under Isoflurane/Dorbene anesthesia, a dorsal midline skin incision was made from vertebral level T5 to L2 and the underlying muscles were removed. A partial laminectomy was performed from around T8 to expose the spinal cord. The exposed spinal cord was then impacted with a metal probe with a force of 250 kDyn (IH-0400 Impactor, Precision Systems

and Instrumentation). The accuracy of the impact was verified intra-operatively, and all the lesions of the animals used in this study were reconstructed post-mortem.

A.6.3 Rehabilitation procedures after spinal cord injury

Rats with severe contusion spinal cord injury were trained daily for 30 min, starting 7 days post-injury. The neurorehabilitation program was conducted on a treadmill using a robotic body-weight support system (Robomedica) that was adjusted to provide optimal assistance during bipedal stepping. To enable locomotion of the paralyzed legs, a serotonergic replacement therapy combining quipazine (0.03 mL) and 8-OHDPAT (0.02 ml) was administered through the microfluidic channel of chronically implanted e-dura, and tonic electrical stimulation was delivered through the electrodes located overlying the midline of lumbar (L2) and sacral (S1) segments (40Hz, 0.2ms pulse duration, 50-200 μ A) [89] [18].

A.6.4 Implantation of e-dura into the cortical subdural space :

The e-dura were implanted under Isoflurane/Dorbene anesthesia. Under sterile conditions, 2 trepanations were performed on the left half of the skull to create two windows rostral and caudal to the leg area of the motor cortex. The first window was located cranially with respect to the coronal suture, while the second window was located cranially with respect to the interparietal suture. Both windows were located close to sagittal suture in order to position the center of the e-dura electrodes 1 mm lateral and 1mm caudal relative to the bregma. The surgical insertion technique developed for passing e-dura into the spinal subdural space was also used to implant e- dura into the cortical subdural space. Excess PDMS material was cut in the cranial window, and the edge of the implants sutured to the dura mater using a Ethilon 8.0 suture. The exposed parts of the brain and external part of the e-dura were covered with surgical silicone (KWIK-SIL). A total of 4 screws were implanted into the skull around the e-dura connector before covering the entire device, the connector, and the percutaneous amphenol connector with dental cement.

A.7 Calibration of gallium evaporation and computation of the Ga/Au atomic ratio β

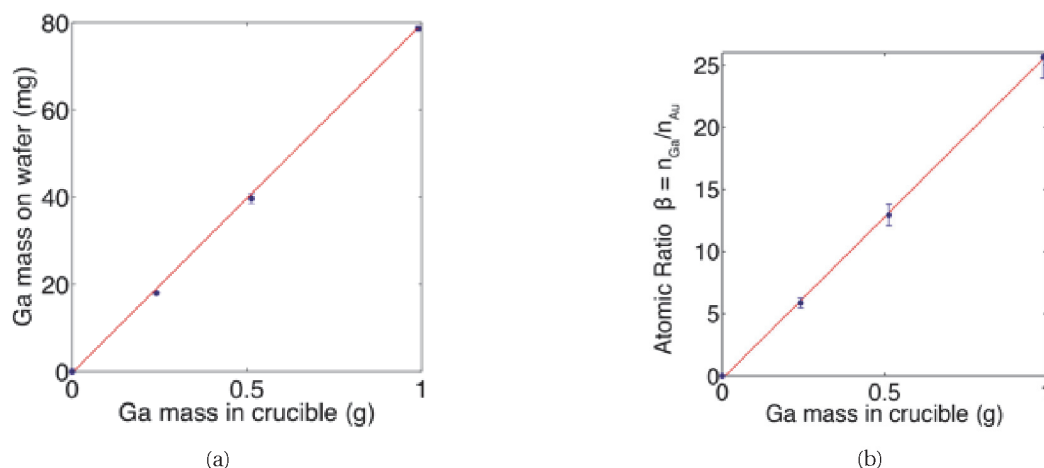


Figure A.3 – Calibration of gallium evaporation and computation of the Ga/Au atomic ratio β .

a - Gallium mass on glass wafers coated with 60 nm of sputtered gold as a function of gallium mass introduced in the crucible of the thermal evaporator. Masses were measured using a PB303-L precision scale from Mettler Toledo ($n = 3$ for each point, error bars: S.D.). **b** - Corresponding Ga/Au atomic ratio β derived from the mass of sputtered gold (8.7 ± 0.5 mg, mean \pm S.D., $n = 3$). Red line represents linear fit.

A.8 Multilayer assembly

The soft assembly consisted of two PDMS-biphasic conductors membranes. The bottom membrane was a 100 μm thick PDMS substrate metalized with the biphasic conductors using stencil patterning as described above. The top membrane was prepared on a 5 μm thick, 4 inch wafer sized slab of PDMS. The slab's surface was functionalized with a 1H,1H,2H,2H-perfluorooctyltriethoxysilane (Sigma-Aldrich) release monolayer under weak vacuum. A 100 μm thick PDMS layer (top layer) was then spin-coated on the PDMS slab and cured. Using a hole puncher (Technical Innovations), the top layer was punctured at locations corresponding to the sites of the vias and further metalized using stencil patterning as previously described. The top layer was then peeled-off from the PDMS slab, plasma activated (29 W, 20 s, PDC-32G-2 etcher, Harrick Plasma), aligned and bonded to the bottom membrane. Drops of eutectic gallium indium (EGaIn, Sigma-Aldrich) were then deposited in the vias to form a conductive bond between the two metallized membranes. The soft assembly was next spin-coated with a 100 μm thick PDMS encapsulation layer and cured at 80 $^{\circ}\text{C}$ for two hours. We used this

approach to prepare a stretchable matrix of 4 x 4 green LEDs interconnected with two planes of biphasic conductors. Powering of the LEDs is controlled and sequenced using an Arduino board. The circular membrane was clamped to a rigid frame through which pressurized air was cycled thereby inflating / releasing the soft optoelectronic skin.

A.9 Lift-Off Patterning of Biphasic Gold–Gallium Thin Films

PDMS substrate was exposed to oxygen plasma (200 mTorr, 29 W, 30 s), then spin-coated with photoresist (AZ-9260 from MicroChemicals) at 6000 rpm for 90 s and left at room temperature for 12 h. The resist was then exposed with a 210 mJ/cm² dose (MJB4 mask aligner from Suss MicroTec, 365 nm UV lamp), developed in diluted AZ-400-K (MicroChemicals, 4:1 deionized water to developer volume ratio) and dried for 15 min at 60 °C on a hot plate. 40 nm of gold was sputtered to form an alloying layer and then 0.2 g of gallium was thermally evaporated. Lift-off was performed in a bath of SVC-14 (Shipley) for 24 h, followed by drying at 60 °C on a hot plate for 15 minute.

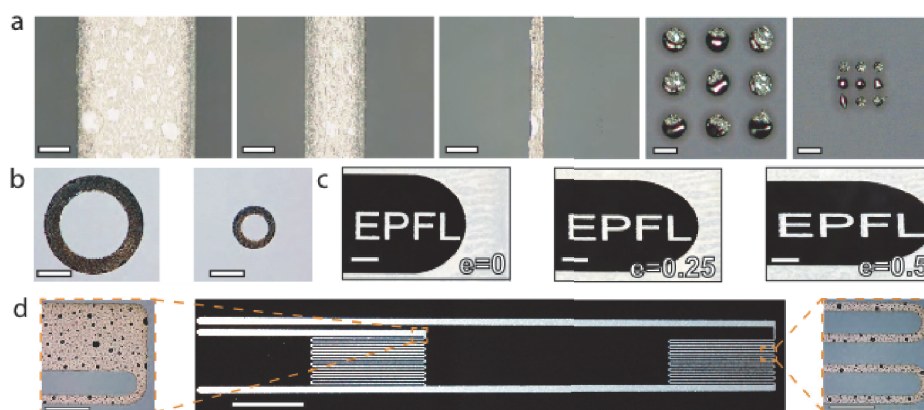


Figure A.4 – Micropatterning of biphasic gold-gallium conductors on PDMS substrates with lift-off processing

a - Optical microscope images of (left to right) 100 μm, 50 μm, and 10 μm wide tracks and 3 × 3 matrices of 25 μm and 10 μm dots of biphasic thin films patterned with a photolithographic lift-off process. Scale bar: 25 μm. **b,c** - Arbitrary patterns of biphasic gold-gallium thin films on PDMS substrates. Scale bars: 250 μm (b) and 1 mm (c). **d** - Pictures of patterns developed over large-area surfaces. Scale bars: 10 mm (main picture) and 500 μm (insets).

Bibliography

- [1] S. P. Lacour, G. Courtine, and J. Guck, "Materials and technologies for soft implantable neuroprostheses," *Nature Reviews Materials*, vol. 1, p. 16063, 2016.
- [2] G. Buzsáki, C. A. Anastassiou, and C. Koch, "The origin of extracellular fields and currents?eeg, ecog, lfp and spikes," *Nature reviews neuroscience*, vol. 13, no. 6, pp. 407–420, 2012.
- [3] L. R. Hochberg, D. Bacher, B. Jarosiewicz, N. Y. Masse, J. D. Simeral, J. Vogel, S. Haddadin, J. Liu, S. S. Cash, P. van der Smagt, *et al.*, "Reach and grasp by people with tetraplegia using a neurally controlled robotic arm," *Nature*, vol. 485, no. 7398, pp. 372–375, 2012.
- [4] D. M. Taylor, S. I. H. Tillery, and A. B. Schwartz, "Direct cortical control of 3d neuroprosthetic devices," *Science*, vol. 296, no. 5574, pp. 1829–1832, 2002.
- [5] J. L. Collinger, B. Wodlinger, J. E. Downey, W. Wang, E. C. Tyler-Kabara, D. J. Weber, A. J. McMorland, M. Velliste, M. L. Boninger, and A. B. Schwartz, "High-performance neuroprosthetic control by an individual with tetraplegia," *The Lancet*, vol. 381, no. 9866, pp. 557–564, 2013.
- [6] K. A. Ludwig, J. D. Uram, J. Yang, D. C. Martin, and D. R. Kipke, "Chronic neural recordings using silicon microelectrode arrays electrochemically deposited with a poly (3, 4-ethylenedioxythiophene)(pedot) film," *Journal of neural engineering*, vol. 3, no. 1, p. 59, 2006.
- [7] M. Jorfi, J. L. Skousen, C. Weder, and J. R. Capadona, "Progress towards biocompatible intracortical microelectrodes for neural interfacing applications," *Journal of neural engineering*, vol. 12, no. 1, p. 011001, 2014.
- [8] J. A. Perge, M. L. Homer, W. Q. Malik, S. Cash, E. Eskandar, G. Friehs, J. P. Donoghue, and L. R. Hochberg, "Intra-day signal instabilities affect decoding performance in an intracortical neural interface system," *Journal of neural engineering*, vol. 10, no. 3, p. 036004, 2013.
- [9] E. C. Leuthardt, G. Schalk, J. R. Wolpaw, J. G. Ojemann, and D. W. Moran, "A brain–computer interface using electrocorticographic signals in humans," *Journal of neural engineering*, vol. 1, no. 2, p. 63, 2004.

Bibliography

- [10] S. Kellis, L. Sorensen, F. Darvas, C. Sayres, K. O'Neill, R. B. Brown, P. House, J. Ojemann, and B. Greger, "Multi-scale analysis of neural activity in humans: implications for micro-scale electrocorticography," *Clinical Neurophysiology*, vol. 127, no. 1, pp. 591–601, 2016.
- [11] E. A. Felton, J. A. Wilson, J. C. Williams, and P. C. Garell, "Electrocorticographically controlled brain–computer interfaces using motor and sensory imagery in patients with temporary subdural electrode implants: report of four cases," *Journal of neurosurgery*, vol. 106, no. 3, pp. 495–500, 2007.
- [12] C. S. Mestais, G. Charvet, F. Sauter-Starace, M. Foerster, D. Ratel, and A. L. Benabid, "Wimagine: Wireless 64-channel ecog recording implant for long term clinical applications," *IEEE Transactions on Neural Systems and Rehabilitation Engineering*, vol. 23, no. 1, pp. 10–21, 2015.
- [13] K. N. Fountas and J. Smith, "A novel closed-loop stimulation system in the control of focal, medically refractory epilepsy," *Operative Neuromodulation*, pp. 357–362, 2007.
- [14] S.-F. Liang, Y.-C. Liao, F.-Z. Shaw, D.-W. Chang, C.-P. Young, and H. Chiueh, "Closed-loop seizure control on epileptic rat models," *Journal of neural engineering*, vol. 8, no. 4, p. 045001, 2011.
- [15] C. N. Heck, D. King-Stephens, A. D. Massey, D. R. Nair, B. C. Jobst, G. L. Barkley, V. Salanova, A. J. Cole, M. C. Smith, R. P. Gwinn, *et al.*, "Two-year seizure reduction in adults with medically intractable partial onset epilepsy treated with responsive neurostimulation: Final results of the rns system pivotal trial," *Epilepsia*, vol. 55, no. 3, pp. 432–441, 2014.
- [16] R. G. Bittar and P. J. Teddy, "Peripheral neuromodulation for pain," *Journal of Clinical Neuroscience*, vol. 16, no. 10, pp. 1259–1261, 2009.
- [17] T. L. Yaksh, C. J. Fisher, T. M. Hockman, and A. J. Wiese, "Current and future issues in the development of spinal agents for the management of pain," *Current neuropharmacology*, vol. 15, no. 2, pp. 232–259, 2017.
- [18] G. Courtine, Y. Gerasimenko, R. Van Den Brand, A. Yew, P. Musienko, H. Zhong, B. Song, Y. Ao, R. M. Ichiyama, I. Lavrov, *et al.*, "Transformation of nonfunctional spinal circuits into functional states after the loss of brain input," *Nature neuroscience*, vol. 12, no. 10, pp. 1333–1342, 2009.
- [19] Y. P. Gerasimenko, D. C. Lu, M. Modaber, S. Zdunowski, P. Gad, D. G. Sayenko, E. Morikawa, P. Haakana, A. R. Ferguson, R. R. Roy, *et al.*, "Noninvasive reactivation of motor descending control after paralysis," *Journal of neurotrauma*, vol. 32, no. 24, pp. 1968–1980, 2015.
- [20] C. A. Angeli, V. R. Edgerton, Y. P. Gerasimenko, and S. J. Harkema, "Altering spinal cord excitability enables voluntary movements after chronic complete paralysis in humans," *Brain*, vol. 137, no. 5, pp. 1394–1409, 2014.

-
- [21] D. D. Harrison, S. O. Harrison, A. C. Croft, D. E. Harrison, and S. J. Troyanovich, "Sitting biomechanics part i: review of the literature," *Journal of manipulative and physiological therapeutics*, vol. 22, no. 9, pp. 594–609, 1999.
- [22] A. Gilletti and J. Muthuswamy, "Brain micromotion around implants in the rodent somatosensory cortex," *Journal of neural engineering*, vol. 3, no. 3, p. 189, 2006.
- [23] B. Poncelet, V. Wedeen, R. Weisskoff, and M. Cohen, "Brain parenchyma motion: measurement with cine echo-planar mr imaging,," *Radiology*, vol. 185, no. 3, pp. 645–651, 1992.
- [24] M. E. Wagshul, P. K. Eide, and J. R. Madsen, "The pulsating brain: a review of experimental and clinical studies of intracranial pulsatility," *Fluids and Barriers of the CNS*, vol. 8, no. 1, p. 5, 2011.
- [25] P.-I. Branemark, "Osseointegration and its experimental background," *The Journal of prosthetic dentistry*, vol. 50, no. 3, pp. 399–410, 1983.
- [26] V. S. Polikov, P. A. Tresco, and W. M. Reichert, "Response of brain tissue to chronically implanted neural electrodes," *Journal of neuroscience methods*, vol. 148, no. 1, pp. 1–18, 2005.
- [27] J. C. Barrese, N. Rao, K. Paroo, C. Triebwasser, C. Vargas-Irwin, L. Franquemont, and J. P. Donoghue, "Failure mode analysis of silicon-based intracortical microelectrode arrays in non-human primates," *Journal of neural engineering*, vol. 10, no. 6, p. 066014, 2013.
- [28] J. C. Sanchez, N. Alba, T. Nishida, C. Batich, and P. R. Carney, "Structural modifications in chronic microwire electrodes for cortical neuroprosthetics: a case study," *IEEE Transactions on Neural Systems and Rehabilitation Engineering*, vol. 14, no. 2, pp. 217–221, 2006.
- [29] E. Patrick, M. E. Orazem, J. C. Sanchez, and T. Nishida, "Corrosion of tungsten microelectrodes used in neural recording applications," *Journal of neuroscience methods*, vol. 198, no. 2, pp. 158–171, 2011.
- [30] K. A. Potter, A. C. Buck, W. K. Self, and J. R. Capadona, "Stab injury and device implantation within the brain results in inversely multiphasic neuroinflammatory and neurodegenerative responses," *Journal of neural engineering*, vol. 9, no. 4, p. 046020, 2012.
- [31] J. Harris, J. Capadona, R. Miller, B. Healy, K. Shanmuganathan, S. Rowan, C. Weder, and D. Tyler, "Mechanically adaptive intracortical implants improve the proximity of neuronal cell bodies," *Journal of neural engineering*, vol. 8, no. 6, p. 066011, 2011.
- [32] J. K. Nguyen, D. J. Park, J. L. Skousen, A. E. Hess-Dunning, D. J. Tyler, S. J. Rowan, C. Weder, and J. R. Capadona, "Mechanically-compliant intracortical implants reduce the neuroinflammatory response," *Journal of neural engineering*, vol. 11, no. 5, p. 056014, 2014.

Bibliography

- [33] E. M. Maynard, C. T. Nordhausen, and R. A. Normann, "The utah intracortical electrode array: a recording structure for potential brain-computer interfaces," *Electroencephalography and clinical neurophysiology*, vol. 102, no. 3, pp. 228–239, 1997.
- [34] D. C. Rodger, A. J. Fong, W. Li, H. Ameri, A. K. Ahuja, C. Gutierrez, I. Lavrov, H. Zhong, P. R. Menon, E. Meng, *et al.*, "Flexible parylene-based multielectrode array technology for high-density neural stimulation and recording," *Sensors and Actuators B: chemical*, vol. 132, no. 2, pp. 449–460, 2008.
- [35] M. Reina, A. Lopez-Garcia, M. Dittmann, and J. De Andrés, "Structural analysis of the thickness of human dura mater with scanning electron microscopy," *Revista espanola de anestesiologia y reanimacion*, vol. 43, no. 4, pp. 135–137, 1996.
- [36] M. angel Reina, M. Dittmann, A. L. Garcia, and A. van Zundert, "New perspectives in the microscopic structure of human dura mater in the dorsolumbar region," *Regional Anesthesia and Pain Medicine*, vol. 22, no. 2, pp. 161–166, 1997.
- [37] D. J. Patin, E. C. Eckstein, K. Harum, and V. S. Pallares, "Anatomic and biomechanical properties of human lumbar dura mater.," *Anesthesia & Analgesia*, vol. 76, no. 3, pp. 535–540, 1993.
- [38] M. Runza, R. Pietrabissa, S. Mantero, A. Albani, V. Quaglini, and R. Contro, "Lumbar dura mater biomechanics: experimental characterization and scanning electron microscopy observations," *Anesthesia & Analgesia*, vol. 88, no. 6, pp. 1317–1321, 1999.
- [39] W. W. Fang, "An in-vivo measurement and analysis of viscoelastic properties of the spinal cord of cats," *spinal cord*, vol. 6, p. 7, 1988.
- [40] A. R. Tunturi, "Elasticity of the spinal cord dura in the dog," *Journal of neurosurgery*, vol. 47, no. 3, pp. 391–396, 1977.
- [41] J. T. Maikos, R. A. Elias, and D. I. Shreiber, "Mechanical properties of dura mater from the rat brain and spinal cord," *Journal of neurotrauma*, vol. 25, no. 1, pp. 38–51, 2008.
- [42] D. E. Harrison, R. Cailliet, D. D. Harrison, S. J. Troyanovich, and S. O. Harrison, "A review of biomechanics of the central nervous system?part iii: spinal cord stresses from postural loads and their neurologic effects," *Journal of manipulative and physiological therapeutics*, vol. 22, no. 6, pp. 399–410, 1999.
- [43] S. Bhattacharya, A. Datta, J. M. Berg, and S. Gangopadhyay, "Studies on surface wettability of poly (dimethyl) siloxane (pdms) and glass under oxygen-plasma treatment and correlation with bond strength," *Journal of microelectromechanical systems*, vol. 14, no. 3, pp. 590–597, 2005.
- [44] S. F. Cogan, "Neural stimulation and recording electrodes," *Annu. Rev. Biomed. Eng.*, vol. 10, pp. 275–309, 2008.

- [45] M. W. Slutzky, L. R. Jordan, T. Krieg, M. Chen, D. J. Mogul, and L. E. Miller, "Optimal spacing of surface electrode arrays for brain-machine interface applications," *Journal of neural engineering*, vol. 7, no. 2, p. 026004, 2010.
- [46] T. Kaiju, K. Doi, M. Yokota, K. Watanabe, M. Inoue, H. Ando, K. Takahashi, F. Yoshida, M. Hirata, and T. Suzuki, "High spatiotemporal resolution ecog recording of somatosensory evoked potentials with flexible micro-electrode arrays," *Frontiers in neural circuits*, vol. 11, 2017.
- [47] I. R. Mineev, N. Wenger, G. Courtine, and S. P. Lacour, "Research update: Platinum-elastomer mesocomposite as neural electrode coating," *APL Materials*, vol. 3, no. 1, p. 014701, 2015.
- [48] T. Rose and L. Robblee, "Electrical stimulation with pt electrodes. viii. electrochemically safe charge injection limits with 0.2 ms pulses (neuronal application)," *IEEE Transactions on Biomedical Engineering*, vol. 37, no. 11, pp. 1118–1120, 1990.
- [49] K. Wang, H. A. Fishman, H. Dai, and J. S. Harris, "Neural stimulation with a carbon nanotube microelectrode array," *Nano letters*, vol. 6, no. 9, pp. 2043–2048, 2006.
- [50] E. W. Keefer, B. R. Botterman, M. I. Romero, A. F. Rossi, and G. W. Gross, "Carbon nanotube coating improves neuronal recordings," *Nature nanotechnology*, vol. 3, no. 7, pp. 434–439, 2008.
- [51] R. A. Green, N. H. Lovell, G. G. Wallace, and L. A. Poole-Warren, "Conducting polymers for neural interfaces: challenges in developing an effective long-term implant," *Biomaterials*, vol. 29, no. 24, pp. 3393–3399, 2008.
- [52] T. D. Y. Kozai, N. B. Langhals, P. R. Patel, X. Deng, H. Zhang, K. L. Smith, J. Lahann, N. A. Kotov, and D. R. Kipke, "Ultrasoft implantable composite microelectrodes with bioactive surfaces for chronic neural interfaces," *Nature materials*, vol. 11, no. 12, p. 1065, 2012.
- [53] A. A. Guex, N. Vachicouras, A. E. Hight, M. C. Brown, D. J. Lee, and S. P. Lacour, "Conducting polymer electrodes for auditory brainstem implants," *Journal of Materials Chemistry B*, vol. 3, no. 25, pp. 5021–5027, 2015.
- [54] Z. Zhu, G. Yang, R. Li, and T. Pan, "Photopatternable pedot: Pss/peg hybrid thin film with moisture stability and sensitivity," *Microsystems & Nanoengineering*, vol. 3, p. 17004, 2017.
- [55] K. Deisseroth, G. Feng, A. K. Majewska, G. Miesenböck, A. Ting, and M. J. Schnitzer, "Next-generation optical technologies for illuminating genetically targeted brain circuits," 2006.
- [56] O. Yizhar, L. E. Fenno, T. J. Davidson, M. Mogri, and K. Deisseroth, "Optogenetics in neural systems," *Neuron*, vol. 71, no. 1, pp. 9–34, 2011.

Bibliography

- [57] V. Gilja, C. A. Chestek, I. Diester, J. M. Henderson, K. Deisseroth, and K. V. Shenoy, "Challenges and opportunities for next-generation intracortically based neural prostheses," *IEEE Transactions on Biomedical Engineering*, vol. 58, no. 7, pp. 1891–1899, 2011.
- [58] R. Pashaie, P. Anikeeva, J. H. Lee, R. Prakash, O. Yizhar, M. Prigge, D. Chander, T. J. Richner, and J. Williams, "Optogenetic brain interfaces," *IEEE reviews in biomedical engineering*, vol. 7, pp. 3–30, 2014.
- [59] M. T. Alt, E. Fiedler, L. Rudmann, J. S. Ordonez, P. Ruther, and T. Stieglitz, "Let there be light?optoprobes for neural implants," *Proceedings of the IEEE*, vol. 105, no. 1, pp. 101–138, 2017.
- [60] P. Musienko, R. van den Brand, O. Maerzendorfer, A. Larmagnac, and G. Courtine, "Combinatory electrical and pharmacological neuroprosthetic interfaces to regain motor function after spinal cord injury," *IEEE Transactions on Biomedical Engineering*, vol. 56, no. 11, pp. 2707–2711, 2009.
- [61] Y. Xia and G. M. Whitesides, "Soft lithography," *Annual review of materials science*, vol. 28, no. 1, pp. 153–184, 1998.
- [62] J. A. Rogers, R. Ghaffari, and D.-H. Kim, *Stretchable Bioelectronics for Medical Devices and Systems*. Springer, 2016.
- [63] M. Stoppa and A. Chiolerio, "Wearable electronics and smart textiles: a critical review," *Sensors*, vol. 14, no. 7, pp. 11957–11992, 2014.
- [64] C. Majidi, "Soft robotics: a perspective?current trends and prospects for the future," *Soft Robotics*, vol. 1, no. 1, pp. 5–11, 2014.
- [65] R. Verplancke, F. Bossuyt, D. Cuypers, and J. Vanfleteren, "Thin-film stretchable electronics technology based on meandering interconnections: fabrication and mechanical performance," *Journal of Micromechanics and Microengineering*, vol. 22, no. 1, p. 015002, 2011.
- [66] D.-H. Kim, N. Lu, R. Ma, Y.-S. Kim, R.-H. Kim, S. Wang, J. Wu, S. M. Won, H. Tao, A. Islam, *et al.*, "Epidermal electronics," *science*, vol. 333, no. 6044, pp. 838–843, 2011.
- [67] S. Xu, Y. Zhang, L. Jia, K. E. Mathewson, K.-I. Jang, J. Kim, H. Fu, X. Huang, P. Chava, R. Wang, *et al.*, "Soft microfluidic assemblies of sensors, circuits, and radios for the skin," *Science*, vol. 344, no. 6179, pp. 70–74, 2014.
- [68] S. P. Lacour, J. Jones, Z. Suo, and S. Wagner, "Design and performance of thin metal film interconnects for skin-like electronic circuits," *IEEE Electron Device Letters*, vol. 25, no. 4, pp. 179–181, 2004.
- [69] S. P. Lacour, J. Jones, S. Wagner, T. Li, and Z. Suo, "Stretchable interconnects for elastic electronic surfaces," *Proceedings of the IEEE*, vol. 93, no. 8, pp. 1459–1467, 2005.

- [70] I. M. Graz, D. P. Cotton, and S. P. Lacour, "Extended cyclic uniaxial loading of stretchable gold thin-films on elastomeric substrates," *Applied Physics Letters*, vol. 94, no. 7, p. 071902, 2009.
- [71] C. F. Guo, T. Sun, Q. Liu, Z. Suo, and Z. Ren, "Highly stretchable and transparent nanomesh electrodes made by grain boundary lithography," *Nature communications*, vol. 5, p. 3121, 2014.
- [72] D. J. Lipomi, J. A. Lee, M. Vosgueritchian, B. C.-K. Tee, J. A. Bolander, and Z. Bao, "Electronic properties of transparent conductive films of PEDOT:PSS on stretchable substrates," *Chemistry of Materials*, vol. 24, no. 2, pp. 373–382, 2012.
- [73] P. Lee, J. Lee, H. Lee, J. Yeo, S. Hong, K. H. Nam, D. Lee, S. S. Lee, and S. H. Ko, "Highly stretchable and highly conductive metal electrode by very long metal nanowire percolation network," *Advanced materials*, vol. 24, no. 25, pp. 3326–3332, 2012.
- [74] V. Martinez, F. Stauffer, M. O. Adagunodo, C. Forro, J. Voros, and A. Larmagnac, "Stretchable silver nanowire–elastomer composite microelectrodes with tailored electrical properties," *ACS applied materials & interfaces*, vol. 7, no. 24, pp. 13467–13475, 2015.
- [75] A. Larmagnac, S. Eggenberger, H. Janossy, and J. Vörös, "Stretchable electronics based on Ag-PDMS composites," *Scientific reports*, vol. 4, 2014.
- [76] K.-Y. Chun, Y. Oh, J. Rho, J.-H. Ahn, Y.-J. Kim, H. R. Choi, and S. Baik, "Highly conductive, printable and stretchable composite films of carbon nanotubes and silver," *Nature nanotechnology*, vol. 5, no. 12, pp. 853–857, 2010.
- [77] M. D. Dickey, "Liquid metals for soft and stretchable electronics," in *Stretchable Bioelectronics for Medical Devices and Systems*, pp. 3–30, Springer, 2016.
- [78] I. D. Joshipura, H. R. Ayers, C. Majidi, and M. D. Dickey, "Methods to pattern liquid metals," *Journal of Materials Chemistry C*, vol. 3, no. 16, pp. 3834–3841, 2015.
- [79] J.-B. Chossat, Y.-L. Park, R. J. Wood, and V. Duchaine, "A soft strain sensor based on ionic and metal liquids," *IEEE Sensors Journal*, vol. 13, no. 9, pp. 3405–3414, 2013.
- [80] C. Keplinger, J.-Y. Sun, C. C. Foo, P. Rothemund, G. M. Whitesides, and Z. Suo, "Stretchable, transparent, ionic conductors," *Science*, vol. 341, no. 6149, pp. 984–987, 2013.
- [81] Y. Cao, T. G. Morrissey, E. Acome, S. I. Allec, B. M. Wong, C. Keplinger, and C. Wang, "A transparent, self-healing, highly stretchable ionic conductor," *Advanced Materials*, vol. 29, no. 10, 2017.
- [82] S. P. Lacour, Z. Huang, Z. Suo, and S. Wagner, "Deformable interconnects for conformal integrated circuits," *MRS Online Proceedings Library Archive*, vol. 736, 2002.

Bibliography

- [83] I. R. Mineev, P. Musienko, A. Hirsch, Q. Barraud, N. Wenger, E. M. Moraud, J. Gandar, M. Capogrosso, T. Milekovic, L. Asboth, *et al.*, “Electronic dura mater for long-term multimodal neural interfaces,” *Science*, vol. 347, no. 6218, pp. 159–163, 2015.
- [84] K. Franze, P. A. Janmey, and J. Guck, “Mechanics in neuronal development and repair,” *Annual review of biomedical engineering*, vol. 15, pp. 227–251, 2013.
- [85] N. Dominici, U. Keller, H. Vallery, L. Friedli, R. Van Den Brand, M. L. Starkey, P. Musienko, R. Riener, and G. Courtine, “Versatile robotic interface to evaluate, enable and train locomotion and balance after neuromotor disorders,” *Nature medicine*, vol. 18, no. 7, pp. 1142–1147, 2012.
- [86] P. Musienko, R. van den Brand, O. Märzendorfer, R. R. Roy, Y. Gerasimenko, V. R. Edgerton, and G. Courtine, “Controlling specific locomotor behaviors through multidimensional monoaminergic modulation of spinal circuitries,” *Journal of Neuroscience*, vol. 31, no. 25, pp. 9264–9278, 2011.
- [87] N. Wenger, E. M. Moraud, S. Raspopovic, M. Bonizzato, J. DiGiovanna, P. Musienko, M. Morari, S. Micera, and G. Courtine, “Closed-loop neuromodulation of spinal sensorimotor circuits controls refined locomotion after complete spinal cord injury,” *Science translational medicine*, vol. 6, no. 255, pp. 255ra133–255ra133, 2014.
- [88] N. Wenger, E. M. Moraud, J. Gandar, P. Musienko, M. Capogrosso, L. Baud, C. G. Le Goff, Q. Barraud, N. Pavlova, N. Dominici, *et al.*, “Spatiotemporal neuromodulation therapies engaging muscle synergies improve motor control after spinal cord injury,” *Nature medicine*, vol. 22, no. 2, p. 138, 2016.
- [89] R. van den Brand, J. Heutschi, Q. Barraud, J. DiGiovanna, K. Bartholdi, M. Huerlimann, L. Friedli, I. Vollenweider, E. M. Moraud, S. Duis, *et al.*, “Restoring voluntary control of locomotion after paralyzing spinal cord injury,” *science*, vol. 336, no. 6085, pp. 1182–1185, 2012.
- [90] S. Cheng, E. C. Clarke, and L. E. Bilston, “Rheological properties of the tissues of the central nervous system: a review,” *Medical engineering & physics*, vol. 30, no. 10, pp. 1318–1337, 2008.
- [91] N. Elliott, C. Bertram, B. A. Martin, and A. Brodbelt, “Syringomyelia: A review of the biomechanics,” *Journal of Fluids and Structures*, vol. 40, pp. 1–24, 2013.
- [92] M. Marder, R. D. Deegan, and E. Sharon, “Crumpling, buckling, and cracking: elasticity of thin sheets,” *Physics Today*, vol. 60, no. 2, p. 33, 2007.
- [93] B. Li, Y.-P. Cao, X.-Q. Feng, and H. Gao, “Mechanics of morphological instabilities and surface wrinkling in soft materials: a review,” *Soft Matter*, vol. 8, no. 21, pp. 5728–5745, 2012.

- [94] P. Kim, M. Abkarian, and H. A. Stone, "Hierarchical folding of elastic membranes under biaxial compressive stress," *Nature materials*, vol. 10, no. 12, p. 952, 2011.
- [95] V. Pini, J. Ruz, P. Kosaka, O. Malvar, M. Calleja, and J. Tamayo, "How two-dimensional bending can extraordinarily stiffen thin sheets," *Scientific reports*, vol. 6, 2016.
- [96] J. A. Fan, W.-H. Yeo, Y. Su, Y. Hattori, W. Lee, S.-Y. Jung, Y. Zhang, Z. Liu, H. Cheng, L. Falgout, *et al.*, "Fractal design concepts for stretchable electronics," *Nature communications*, vol. 5, p. 3266, 2014.
- [97] L. Xu, S. R. Gutbrod, A. P. Bonifas, Y. Su, M. S. Sulkin, N. Lu, H.-J. Chung, K.-I. Jang, Z. Liu, M. Ying, *et al.*, "3d multifunctional integumentary membranes for spatiotemporal cardiac measurements and stimulation across the entire epicardium," *Nature communications*, vol. 5, p. 3329, 2014.
- [98] A. Hirsch, I. Minev, N. Pavlova, L. Asboth, G. Courtine, and S. P. Lacour, "Pdms based μ -ecog," in *proceedings MEA Meeting 2014*, pp. 237–238, 2014.
- [99] H. O. Michaud, J. Teixidor, and S. P. Lacour, "Soft metal constructs for large strain sensor membrane," *Smart Materials and Structures*, vol. 24, no. 3, p. 035020, 2015.
- [100] I. R. Minev, D. J. Chew, E. Delivopoulos, J. W. Fawcett, and S. P. Lacour, "High sensitivity recording of afferent nerve activity using ultra-compliant microchannel electrodes: an acute in vivo validation," *Journal of neural engineering*, vol. 9, no. 2, p. 026005, 2012.
- [101] D. J. Chew, L. Zhu, E. Delivopoulos, I. R. Minev, K. M. Musick, C. A. Mosse, M. Craggs, N. Donaldson, S. P. Lacour, S. B. McMahon, *et al.*, "A microchannel neuroprosthesis for bladder control after spinal cord injury in rat," *Science translational medicine*, vol. 5, no. 210, pp. 210ra155–210ra155, 2013.
- [102] T. J. Richner, S. Thongpang, S. K. Brodnick, A. A. Schendel, R. W. Falk, L. A. Krugner-Higby, R. Pashaie, and J. C. Williams, "Optogenetic micro-electrocorticography for modulating and localizing cerebral cortex activity," *Journal of neural engineering*, vol. 11, no. 1, p. 016010, 2014.
- [103] T. Pistohl, A. Schulze-Bonhage, A. Aertsen, C. Mehring, and T. Ball, "Decoding natural grasp types from human ecog," *Neuroimage*, vol. 59, no. 1, pp. 248–260, 2012.
- [104] O. Graudejus, P. Gorrn, and S. Wagner, "Controlling the morphology of gold films on poly (dimethylsiloxane)," *ACS applied materials & interfaces*, vol. 2, no. 7, pp. 1927–1933, 2010.
- [105] T. Adrega and S. Lacour, "Stretchable gold conductors embedded in pdms and patterned by photolithography: fabrication and electromechanical characterization," *Journal of Micromechanics and Microengineering*, vol. 20, no. 5, p. 055025, 2010.

Bibliography

- [106] A. Romeo, Q. Liu, Z. Suo, and S. P. Lacour, "Elastomeric substrates with embedded stiff platforms for stretchable electronics," *Applied Physics Letters*, vol. 102, no. 13, p. 131904, 2013.
- [107] A. Hirsch, H. O. Michaud, A. P. Gerratt, S. De Mulatier, and S. P. Lacour, "Intrinsically stretchable biphasic (solid–liquid) thin metal films," *Advanced Materials*, 2016.
- [108] A. Hirsch and S. P. Lacour, "Gallium super-lyophilic silicone for smooth tailored liquid metal stretchable thin films," *under preparation*, 2017.
- [109] K. Y. Kwon, B. Sirowatka, A. Weber, and W. Li, "Opto- μ ecog array: A hybrid neural interface with transparent μ ecog electrode array and integrated leds for optogenetics," *IEEE transactions on biomedical circuits and systems*, vol. 7, no. 5, pp. 593–600, 2013.
- [110] S. I. Park, D. S. Brenner, G. Shin, C. D. Morgan, B. A. Copits, H. U. Chung, M. Y. Pullen, K. N. Noh, S. Davidson, S. J. Oh, *et al.*, "Soft, stretchable, fully implantable miniaturized optoelectronic systems for wireless optogenetics," *Nature biotechnology*, vol. 33, no. 12, p. 1280, 2015.
- [111] J. Viventi, D.-H. Kim, L. Vigeland, E. S. Frechette, J. A. Blanco, Y.-S. Kim, A. E. Avrin, V. R. Tiruvadi, S.-W. Hwang, A. C. Vanleer, *et al.*, "Flexible, foldable, actively multiplexed, high-density electrode array for mapping brain activity in vivo," *Nature neuroscience*, vol. 14, no. 12, pp. 1599–1605, 2011.
- [112] D. Khodagholy, T. Doublet, P. Quilichini, M. Gurfinkel, P. Leleux, A. Ghestem, E. Ismailova, T. Hervé, S. Sanaur, C. Bernard, *et al.*, "In vivo recordings of brain activity using organic transistors," *Nature communications*, vol. 4, p. 1575, 2013.
- [113] A. Hogg, S. Uhl, F. Feuvrier, Y. Girardet, B. Graf, T. Aellen, H. Keppner, Y. Tardy, and J. Burger, "Protective multilayer packaging for long-term implantable medical devices," *Surface and Coatings Technology*, vol. 255, pp. 124–129, 2014.
- [114] A. Hogg, T. Aellen, S. Uhl, B. Graf, H. Keppner, Y. Tardy, and J. Burger, "Ultra-thin layer packaging for implantable electronic devices," *Journal of Micromechanics and Microengineering*, vol. 23, no. 7, p. 075001, 2013.
- [115] Y. Tokudome, T. Hara, R. Abe, and M. Takahashi, "Transparent and robust siloxane-based hybrid lamella film as a water vapor barrier coating," *ACS applied materials & interfaces*, vol. 6, no. 21, pp. 19355–19359, 2014.
- [116] N. Matsuhisa, M. Kaltenbrunner, T. Yokota, H. Jinno, K. Kuribara, T. Sekitani, and T. Someya, "Printable elastic conductors with a high conductivity for electronic textile applications," *Nature communications*, vol. 6, 2015.
- [117] L. J. Briggs, "Gallium: thermal conductivity; supercooling; negative pressure," *The Journal of Chemical Physics*, vol. 26, no. 4, pp. 784–786, 1957.

- [118] D. Carlson, J. Feder, and A. Segmüller, "Measurement of the liquid-structure factor of supercooled gallium and mercury," *Physical Review A*, vol. 9, no. 1, p. 400, 1974.
- [119] J. Chandler, H. Messer, and G. Ellender, "Cytotoxicity of gallium and indium ions compared with mercuric ion," *Journal of dental research*, vol. 73, no. 9, pp. 1554–1559, 1994.
- [120] M. D. Dickey, "Stretchable and soft electronics using liquid metals," *Advanced Materials*, 2017.
- [121] S. Zhu, J.-H. So, R. Mays, S. Desai, W. R. Barnes, B. Pourdeyhimi, and M. D. Dickey, "Ultra-stretchable fibers with metallic conductivity using a liquid metal alloy core," *Advanced Functional Materials*, vol. 23, no. 18, pp. 2308–2314, 2013.
- [122] M. D. Dickey, "Emerging applications of liquid metals featuring surface oxides," *ACS applied materials & interfaces*, vol. 6, no. 21, pp. 18369–18379, 2014.
- [123] S. Cheng and Z. Wu, "Microfluidic electronics," *Lab on a Chip*, vol. 12, no. 16, pp. 2782–2791, 2012.
- [124] J. Nriagu, *Encyclopedia of environmental health*. Newnes, 2008.
- [125] M. Grayson, R. E. Kirk, and D. F. Othmer, *Kirk-Othmer encyclopedia of chemical technology*. No. Ed. 4, J. Wiley, 1984.
- [126] E. Merian, M. Anke, M. Ihnat, M. Stoeppler, *et al.*, *Elements and their compounds in the environment: occurrence, analysis and biological relevance*. No. Ed. 2, Wiley-VCH Verlag GmbH & Co. KGaA, 2004.
- [127] L. R. Bernstein, "Mechanisms of therapeutic activity for gallium," *Pharmacological reviews*, vol. 50, no. 4, pp. 665–682, 1998.
- [128] C. E. Arnold, A. Bordin, S. D. Lawhon, M. C. Libal, L. R. Bernstein, and N. D. Cohen, "Antimicrobial activity of gallium maltolate against staphylococcus aureus and methicillin-resistant s. aureus and staphylococcus pseudintermedius: An in vitro study," *Veterinary microbiology*, vol. 155, no. 2, pp. 389–394, 2012.
- [129] O. Rzhepishevskaya, B. Ekstrand-Hammarström, M. Popp, E. Björn, A. Bucht, A. Sjöstedt, H. Antti, and M. Ramstedt, "The antibacterial activity of Ga^{3+} is influenced by ligand complexation as well as the bacterial carbon source," *Antimicrobial agents and chemotherapy*, vol. 55, no. 12, pp. 5568–5580, 2011.
- [130] M. Frezza, C. N. Verani, D. Chen, and Q. P. Dou, "The therapeutic potential of gallium-based complexes in anti-tumor drug design," *Letters in Drug Design & Discovery*, vol. 4, no. 5, pp. 311–317, 2007.
- [131] A. E. Martell and R. M. Smith, *Critical stability constants*, vol. 1. Springer, 1974.

Bibliography

- [132] J. C. Wataha, H. Nakajima, C. T. Hanks, and T. Okabe, "Correlation of cytotoxicity with elemental release from mercury-and gallium-based dental alloys in vitro," *Dental Materials*, vol. 10, no. 5, pp. 298–303, 1994.
- [133] J. C. Wataha, C. Hanks, and R. G. Craig, "The effect of cell monolayer density on the cytotoxicity metal ions which are released from dental alloys," *Dental Materials*, vol. 9, no. 3, pp. 172–176, 1993.
- [134] G. Xu, C. Zhang, and L. Ning, "Evaluation on the cytotoxicity of gallium alloy by mtt-assay," *Zhonghua kou qiang yi xue za zhi= Zhonghua kouqiang yixue zazhi= Chinese journal of stomatology*, vol. 36, no. 3, pp. 189–192, 2001.
- [135] A. Milheiro, K. Nozaki, C. J. Kleverlaan, J. Muris, H. Miura, and A. J. Feilzer, "In vitro cytotoxicity of metallic ions released from dental alloys," *Odontology*, vol. 104, no. 2, pp. 136–142, 2016.
- [136] K. Qiu, W. Lin, F. Zhou, H. Nan, B. Wang, L. Li, J. Lin, Y. Zheng, and Y. Liu, "Ti-ga binary alloys developed as potential dental materials," *Materials Science and Engineering: C*, vol. 34, pp. 474–483, 2014.
- [137] Y. Lu, Q. Hu, Y. Lin, D. B. Pacardo, C. Wang, W. Sun, F. S. Ligler, M. D. Dickey, and Z. Gu, "Transformable liquid-metal nanomedicine," *Nature communications*, vol. 6, p. 10066, 2015.
- [138] E. Bingham, B. Cohrssen, C. H. Powell, *et al.*, *Patty's toxicology. Volume 2: toxicological issues related to metals, neurotoxicology and radiation metals and metal compounds*. No. Ed. 5, John Wiley and Sons, 2001.
- [139] M. Kurtjak, M. Vukomanović, L. Kramer, and D. Suvorov, "Biocompatible nano-gallium/hydroxyapatite nanocomposite with antimicrobial activity," *Journal of Materials Science: Materials in Medicine*, vol. 27, no. 11, p. 170, 2016.
- [140] R. Sahdev, T. I. Ansari, S. M. Higham, and S. P. Valappil, "Potential use of gallium-doped phosphate-based glass material for periodontitis treatment," *Journal of biomaterials applications*, vol. 30, no. 1, pp. 85–92, 2015.
- [141] S. P. Valappil, D. Ready, E. A. A. Neel, D. M. Pickup, W. Chrzanowski, L. A. O'Dell, R. J. Newport, M. E. Smith, M. Wilson, and J. C. Knowles, "Antimicrobial gallium-doped phosphate-based glasses," *Advanced functional materials*, vol. 18, no. 5, pp. 732–741, 2008.
- [142] N. Hallfors, A. Khan, M. D. Dickey, and A. M. Taylor, "Integration of pre-aligned liquid metal electrodes for neural stimulation within a user-friendly microfluidic platform," *Lab on a Chip*, vol. 13, no. 4, pp. 522–526, 2013.
- [143] X. Zhao, S. Xu, and J. Liu, "Surface tension of liquid metal: role, mechanism and application," *Frontiers in Energy*, pp. 1–33, 2017.

- [144] P.-G. De Gennes, F. Brochard-Wyart, and D. Quéré, *Capillarity and wetting phenomena: drops, bubbles, pearls, waves*. Springer Science & Business Media, 2013.
- [145] A. Plech, U. Klemradt, H. Metzger, and J. Peisl, “In situ x-ray reflectivity study of the oxidation kinetics of liquid gallium and the liquid alloy,” *Journal of Physics: Condensed Matter*, vol. 10, no. 5, p. 971, 1998.
- [146] Y. Wang, Y. Doong, T. Chen, and J. Haung, “Oxidation of liquid gallium surface: Nonequilibrium growth kinetics in 2+ 1 dimensions,” *Journal of Vacuum Science & Technology A: Vacuum, Surfaces, and Films*, vol. 12, no. 4, pp. 2081–2086, 1994.
- [147] C. Ladd, J.-H. So, J. Muth, and M. D. Dickey, “3d printing of free standing liquid metal microstructures,” *Advanced Materials*, vol. 25, no. 36, pp. 5081–5085, 2013.
- [148] J. W. Boley, E. L. White, G. T.-C. Chiu, and R. K. Kramer, “Direct writing of gallium-indium alloy for stretchable electronics,” *Advanced Functional Materials*, vol. 24, no. 23, pp. 3501–3507, 2014.
- [149] J. Wissman, T. Lu, and C. Majidi, “Soft-matter electronics with stencil lithography,” in *SENSORS, 2013 IEEE*, pp. 1–4, IEEE, 2013.
- [150] N. Bowden, S. Brittain, A. G. Evans, J. W. Hutchinson, and G. M. Whitesides, “Spontaneous formation of ordered structures in thin films of metals supported on an elastomeric polymer,” *Nature*, vol. 393, no. 6681, p. 146, 1998.
- [151] R. P. Elliott and F. A. Shunk, “The au- ga (gold-gallium) system,” *Bulletin of Alloy Phase Diagrams*, vol. 2, no. 3, pp. 356–358, 1981.
- [152] I. Dutta and P. Kumar, “Electric current induced liquid metal flow: Application to coating of micropatterned structures,” *Applied Physics Letters*, vol. 94, no. 18, p. 184104, 2009.
- [153] W. Cao, P. Görrn, and S. Wagner, “Modeling the electrical resistance of gold film conductors on uniaxially stretched elastomeric substrates,” *Applied Physics Letters*, vol. 98, no. 21, p. 212112, 2011.
- [154] D. J. Ellerbrock and D. D. Macdonald, “Passivity breakdown on solid versus liquid gallium,” *Journal of The Electrochemical Society*, vol. 141, no. 10, pp. 2645–2649, 1994.
- [155] J. C. Love, L. A. Estroff, J. K. Kriebel, R. G. Nuzzo, and G. M. Whitesides, “Self-assembled monolayers of thiolates on metals as a form of nanotechnology,” *Chemical reviews*, vol. 105, no. 4, pp. 1103–1170, 2005.
- [156] J. N. Hohman, M. Kim, G. A. Wadsworth, H. R. Bednar, J. Jiang, M. A. LeThai, and P. S. Weiss, “Directing substrate morphology via self-assembly: ligand-mediated scission of gallium-indium microspheres to the nanoscale,” *Nano letters*, vol. 11, no. 12, pp. 5104–5110, 2011.

Bibliography

- [157] L. Ren, J. Zhuang, G. Casillas, H. Feng, Y. Liu, X. Xu, Y. Liu, J. Chen, Y. Du, L. Jiang, *et al.*, “Nanodroplets for stretchable superconducting circuits,” *Advanced Functional Materials*, vol. 26, no. 44, pp. 8111–8118, 2016.
- [158] A. Lafuma and D. Quéré, “Superhydrophobic states,” *Nature materials*, vol. 2, no. 7, pp. 457–460, 2003.
- [159] D. Quéré, “Wetting and roughness,” *Annu. Rev. Mater. Res.*, vol. 38, pp. 71–99, 2008.
- [160] L. Courbin, E. Denieul, E. Dressaire, M. Roper, A. Ajdari, and H. A. Stone, “Imbibition by polygonal spreading on microdecorated surfaces,” *Nature materials*, vol. 6, no. 9, pp. 661–664, 2007.
- [161] C. Ishino and K. Okumura, “Wetting transitions on textured hydrophilic surfaces,” *The European Physical Journal E: Soft Matter and Biological Physics*, vol. 25, no. 4, pp. 415–424, 2008.
- [162] P. B. Weisensee, E. J. Torrealba, M. Raleigh, A. M. Jacobi, and W. P. King, “Hydrophobic and oleophobic re-entrant steel microstructures fabricated using micro electrical discharge machining,” *Journal of Micromechanics and Microengineering*, vol. 24, no. 9, p. 095020, 2014.
- [163] C. Semprebon, P. Forsberg, C. Priest, and M. Brinkmann, “Pinning and wicking in regular pillar arrays,” *Soft Matter*, vol. 10, no. 31, pp. 5739–5748, 2014.
- [164] J. Bico, *Mécanismes d’imprégnation: surfaces texturées, bigouttes, poreux*. PhD thesis, 2000.
- [165] J. Bico, C. Tordeux, and D. Quéré, “Rough wetting,” *EPL (Europhysics Letters)*, vol. 55, no. 2, p. 214, 2001.
- [166] A. Vanhoestenbergh and N. Donaldson, “Corrosion of silicon integrated circuits and lifetime predictions in implantable electronic devices,” *Journal of neural engineering*, vol. 10, no. 3, p. 031002, 2013.
- [167] F. Xiang, S. M. Ward, T. M. Givens, and J. C. Grunlan, “Super stretchy polymer multilayer thin film with high gas barrier,” *Acs Macro Letters*, vol. 3, no. 10, pp. 1055–1058, 2014.
- [168] K. M. Holder, B. R. Spears, M. E. Huff, M. A. Priolo, E. Harth, and J. C. Grunlan, “Stretchable gas barrier achieved with partially hydrogen-bonded multilayer nanocoating,” *Macromolecular rapid communications*, vol. 35, no. 10, pp. 960–964, 2014.
- [169] S. Qin, Y. Song, M. E. Floto, and J. C. Grunlan, “Combined high stretchability and gas barrier in hydrogen-bonded multilayer nanobrick wall thin films,” *ACS Applied Materials & Interfaces*, vol. 9, no. 9, pp. 7903–7907, 2017.
- [170] H. Michaud, *Stretchable metallization technologies for skin-like transducers*. PhD thesis, 2017.

- [171] A. S. Gladman, E. A. Matsumoto, R. G. Nuzzo, L. Mahadevan, and J. A. Lewis, "Biomimetic 4d printing," *Nature materials*, vol. 15, no. 4, pp. 413–418, 2016.
- [172] W. Christiaens, E. Bosman, and J. Vanfleteren, "Utcp: A novel polyimide-based ultra-thin chip packaging technology," *IEEE transactions on components and packaging technologies*, vol. 33, no. 4, pp. 754–760, 2010.



Arthur Hirsch

Education

- 2013 - 2017 **PhD - EPFL**, *Laboratory for Soft Bioelectronic interfaces*, Lausanne.
Thesis title: *Electronic Dura Mater - Soft, multimodal neural interfaces*
- 2011 - 2012 **Master in Mechanical Engineering - EPFL**, *Double Degree cursus*, Lausanne.
Biomedical Technologies mansion
- 2008 - 2012 **Master in Aerospace Engineering - ISAE/Supaero**, Toulouse.
PEGASUS certificate
- June 2008 **Passed the competitive entrance exam to French Grandes Ecoles.**
237 over 3000 range
- 2006 - 2008 **Classes Préparatoires au Lycée Sainte-Geneviève (PC*)**, Versailles.
Undergraduate studies in national preparatory program for entrance into French state run graduate schools of engineering
- 2006 **Baccalauréat S**, *Suma cum laude*.
French equivalent of junior college diploma

Research and Work Experience

- Feb. 2013 **Master Thesis: R&D designer internship**, *Plugmed*, France.
to Aug. 2013 Development of an innovative skull implant
- Sep. 2013 **Neural bioMEMS development**, *EPFL*, Switzerland.
to Jan. 2013 Design optimization of soft gold neural electrodes on PDMS
- Feb. 2012 **"Lab-in-tube" 2012 project Winner**, *EPFL*, Switzerland.
to Aug. 2012 Micro sensor for blood flow using flexible electronics design leading - team project
- Sept. 2011 **Biomechanics development**, *EPFL*, Switzerland.
to Jan. 2012 3D model of the spinal subarachnoid space build up
- Feb. 2011 **Medical robotics development**, *CNRS*, France.
to Aug. 2011 Human Hand Dynamics model for a Linear Haptic Interface

Awards and Scholarship

- Sep. 2017 **Innogrant**, *EPFL*.
100'000 CHF entrepreneurial grant
- Mar. 2016 **MRS iMatSci Innovator Award**, *MRS 2016 Phoenix*.
Materials research society innovation award, 2nd prize

chemin du petit chateau, 1 – 1005 Lausanne – Switzerland

☎ +41 76 822 05 92 • ✉ arthur.edouard.hirsch@gmail.com
🌐 www.feeltronix.com • in [arthur-hirsch-a05ab411b/](https://www.linkedin.com/in/arthur-hirsch-a05ab411b/)

Technical Skills

Computer skills

C.A.D	Catia, Solid Works	Simulation	Comsol, Abacus, Fluent
Maths	Matlab, Simulink, Labview	Other	LaTeX, Illustrator, Photoshop
Coding	Arduino, Java, C++		

Cleanroom equipment and electrical characterization

Thin films	E-beam/Thermal Evaporation, Sputtering	Substrates	PDMS, Parylene C, Polyimide
Patterning	Dry/Wet Etching, Lift-off	Metrology	SEM, Porfilometer

Languages

French	Native	German	Basic
English	Professional working proficiency		

Leadership and Activities

- 2013 - 2014 President of EPFL Analog Photography Club
- 2011 "Lessons for children", singer songwriter and leader
Live tour 32 performance, studio album recording and release
- 2010 Supaero student welcome week association Vice President
- 2008 - 2010 Supaero gliding club Vice President
- Others Photography, film making, swimming

Publications

- [1] A. Hirsch and S. P. Lacour, "Gallium super-lyophilic silicone for smooth tailored liquid metal stretchable thin films," *submitted*, 2017.
- [2] A. Hirsch, H. O. Michaud, A. P. Gerratt, S. De Mulatier, and S. P. Lacour, "Intrinsically stretchable biphasic (solid-liquid) thin metal films," *Advanced Materials*, 2016.
- [3] I. R. Minev, P. Musienko, A. Hirsch, Q. Barraud, N. Wenger, E. M. Moraud, J. Gandar, M. Capogrosso, T. Milekovic, L. Asboth, *et al.*, "Electronic dura mater for long-term multimodal neural interfaces," *Science*, vol. 347, no. 6218, pp. 159–163, 2015.
- [4] A. Hirsch, I. Minev, N. Pavlova, L. Asboth, G. Courtine, and S. P. Lacour, "Pdms based μ -ecog," in *proceedings MEA Meeting 2014*, pp. 237–238, 2014.
- [5] I. Minev, A. Hirsch, P. Musienko, G. Courtine, and S. Lacour, "Peau synthétique pour enregistrer et moduler des activités physiologiques," July 14 2016. WO Patent App. PCT/EP2016/050,270.
- [6] A. Hirsch, H. Michaud, I. Minev, and S. Lacour, "Method for manufacturing electrical conductors, and electrical conductors manufactured according to same," May 4 2017. WO Patent App. PCT/EP2016/076,174.

chemin du petit chateau, 1 – 1005 Lausanne – Switzerland

☎ +41 76 822 05 92 • ✉ arthur.edouard.hirsch@gmail.com

🌐 www.feeltronix.com • in [arthur-hirsch-a05ab411b/](https://www.linkedin.com/in/arthur-hirsch-a05ab411b/)

